UNIVERSITY OF TURKU

Simulation of metal powder packing behaviour in laser-based powder bed fusion

Master of Science in Technology Thesis
Materials of Energy Technology
Material Engineering
Department of Mechanical and Materials Engineering

Author:
Erik Haapa

Supervisors:
Adjunct professor Heidi Piili D.Sc. (Tech.)
Development manager Juha Ottelin M.Sc. (Tech)

10.02.2023
Turku

The originality of this thesis has been checked in accordance with the University of Turku quality assurance system using the Turnitin Originality Check service.

Master's thesis

Subject: Material Engineering
Author: Erik Haapa
Title: Simulation of metal powder packing behaviour in laser-based powder bed fusion
Supervisor(s): Adjunct professor Heidi Piili, development manager Juha Ottelin
Number of pages: 132 pages
Date: 10.02.2023

Laser-based powder bed fusion (L-PBF) is a method of additive manufacturing, in which metal powder is fused into solid parts, layer by layer. L-PBF shows high promise for manufacture of functional Tungsten parts, but the development of Tungsten powder feedstock for L-PBF processing is demanding and expensive. Therefore, computer simulation is explored as a possible tool for Tungsten powder feedstock development at EOS Finland Oy, with whom this thesis was made.

The aim of this thesis was to develop a simulation model of the recoating process of an EOS M 290 L-PBF system, as well as a validation method for the simulation. The validated simulation model can be used to evaluate the applicability of the used simulation software (FLOW-3D DEM) in powder material development, and possibly use the model as a platform for future application with Tungsten powder. In order to reduce complexity and uncertainties, the irregular Tungsten powder is not yet simulated, and a well-known, spherical EOS IN718 powder feedstock was used instead.

The validation experiment is based on building a low, enclosed wall using the M 290 L-PBF system. Recoated powder is trapped inside as the enclosure is being built, making it possible to remove the sampled powder from a known volume. This enables measuring the powder packing density (*PD*) of the powder bed. The experiment was repeated five times and some sources of error were also quantified. Average PD was found to be 52 % with a standard deviation of 0.2 %.

The simulation was modelled after the IN718 powder and corresponding process used in the M 290 system. Material-related input values were found by dynamic image analysis, pycnometry, rheometry, and from literature. *PD* was measured with six different methods, and the method considered as most analogous to the practical validation experiment yielded a *PD* of 52 %. Various particle behavior phenomena were also observed and analyzed.

Many of the powder bed characterization methods found in literature were not applicable to L-PBF processing or were not representative of the simulated conditions. Many simulation studies were also found to use no validation, or used a validation method which is not based on the investigated phenomena. The validation model developed in this thesis accurately represents the simulated conditions and is found to produce reliable and repeatable results. The simulation model was parametrized with values acquired from practical experiments or literature and closely matched the validation experiment, and could therefore be considered a truthful representation of the powder recoating process of an EOS M 290. The model can be used as a platform for future development of Tungsten powder simulation.

Key words: additive manufacturing, laser-based powder bed fusion, metal, 3D-printing, simulation, validation, powder packing, DEM, IN718

Acknowledgements

This thesis opportunity was offered to me despite my lack of noteworthy previous experience in simulation, and I am thankful to those who took a chance with me and made it happen. Sincere thanks go to Tatu Syvänen, Juha Ottelin, Pilvi Ylander, Kevin Minet, and Olli Nyrhilä of EOS Finland for first of all entrusting this project to me, but also for their continued support, genuine interest, and guidance.

The single most influential person for this thesis, my supervisor Heidi Piili, deserves many thanks for providing her profound experience and cheerful guidance, as well as an honorable mention for her patience in repeating the same instructions to me meeting after meeting. This work would not have found its final form without her expertise and eagerness to help shape my thesis into the best it could be.

Working at EOS Finland, I cannot even begin to thank everyone who helped me at some point along the way, but I will try. There are still many who will unjustly not find their name here but know that I appreciate your help! Thanks to all the knowledgeable and helpful people of R&D and quality departments, for their support and their smart answers to my dumb questions; Ilkka, Shaafi, Mika, Visa, Katri, Jarno, and many others. Thank you also the operators, Aki, Kauko, and Niklas, for not only training me with the use of the machines but also all the other tools, instruments and processes that make up a large part of the actual work in AM… not to mention the times they saved my jobs or even did some of the prep work for me. Thanks to Saija, Janne and other folks at the laboratory for helping with finding all sorts of equipment and guiding in their use, as well as providing necessary lab results from previous experiments.

I'd like to thank Aditya and Saeid of the research group at UTU for their expertise, support, and advice! I must also acknowledge prof. Antti Salminen for his hard work in the background of everything, from first referring me to EOS Finland, to going through a lot of effort to enable a position for me to continue this work at UTU. Thank you!

Last but certainly not least I thank my family and friends for all the various support, fun company and great moments among the hurries and worries of thesis writing.

Table of contents

Nomenclature

Abbreviation	Explanation
AM	Additive manufacturing (colloquially “3D-printing”)
AOR	Angle of repose (of a powder pile)
CAD	Computer-aided design
CAM	Computer-aided manufacturing
CFD	Computed fluid dynamics
DRA	Dynamic repose angle (of a powder pile pushed by a recoater)
GA	Gas atomisation
DEM	Discrete element method
EIGA	Electrode inert gas atomisation
IN718	EOS NickelAlloy IN718 (a Nickel superalloy powder material)
IPA	Isopropyl alcohol
L-PBF	Laser-based powder bed fusion
LSD	Linear spring-dashpot (DEM contact model)
OL	Open cup, large (validation sample)
PA	Plasma atomisation
PBF	Powder bed fusion
PREP	Plasma rotating electrode process
PSD	Particle size distribution
SEM	Scanning electron microscope
VDW	Van Der Waals forces
W1	EOS Tungsten W1 (a pure Tungsten powder material)
WA	Water atomisation

Symbol	Unit	Explanation
AIF	°	Angle of internal friction
AWF	°	Angle of wall friction
BFE	mJ	Energy spent to spin a rheometer blade in powder sample
d10	µm	Top 10th percentile of particle sizes
d50	µm	Top 50th percentile of particle sizes (= median particle size)
d90	µm	Top 90th percentile of particle sizes
E	GPa	Young’s modulus
e	-	Coefficient of restitution
E_m	mJ/g	Specific energy spent to spin a rheometer blade in powder sample
h	mm	Average height of OL sample
h_1-h_4	mm	Height of OL sample (at corners 1-4)
h_l	µm	Height of recoated layer
h_{lt}	µm	True height of recoated layer

k	N/m	Spring constant
l	mm	Average inner length of OL sample
l_1-l_3	mm	Inner length of OL sample (at locations 1-3)
m_{full}	g	Mass of the OL sample, including platform and powder
$m_{emptied}$	g	Mass of the OL sample after removing sampled powder
$m_{cleaned.}$	g	Mass of the OL sample after removing sampled and residual powder
m_{powder_max}	g	Mass of powder removed from sample and cleaned from platform
$m_{powder\_measured}$	g	Mass of powder removed from sample; assumed true sampled mass
m_{powder_min}	g	Mass of powder recovered from sample, not including losses
PD	%	Powder packing density, volume of space taken by powder particles
$PDmax_{sim}$	%	Powder packing density measured from simulation with Method 3
$PDmeasured_{sim}$	%	Powder packing density measured from simulation with Method 4
$PDmin_{sim}$	%	Powder packing density measured from simulation with Method 2
r	mm	Fillet radius of OL sample corners
SE	mJ/m^2	Surface energy
SR	µm	Surface roughness (of the powder bed)
V_{powder}	cm^3	Volume occupied by powder particles (in a sampled volume)
V_{sample}	cm^3	Total sampled volume
$V_{sample\_measured}$	cm^3	Measured volume contained within inner extents of OL sample
$V_{nominal}$	cm^3	Nominal ideal volume of 3D-model of the OL sample
w	mm	Average inner width of OL sample
w_1-w_3	mm	Inner width of OL sample (at locations 1-3)

Greek letters	Unit	Explanation
μ	-	Coefficient of friction
μS	-	Coefficient of static friction
μSpp	-	Coefficient of static friction, particle-particle
μSpw	-	Coefficient of static friction, particle-wall
μD	-	Coefficient of dynamic friction
μDpp	-	Coefficient of dynamic friction, particle-particle
μDpw	-	Coefficient of dynamic friction, particle-wall
ρ_s	g/cm^3	Skeletal density; particle density accounting for internal pores

1 Introduction

This thesis work was done with EOS Finland Oy (Finland), a metal material and process development unit of EOS GmbH (Germany), which is a leading supplier of laser-based powder bed fusion (L-PBF) systems, materials, and processes for metals and polymers.

L-PBF as a manufacturing process falls under the umbrella of additive manufacturing, or AM. [1, 2] AM is further divided into seven different subcategories, of which only powder bed fusion (PBF) and more specifically L-PBF will be considered in this thesis. In L-PBF, a laser beam is used to melt and fuse thin layers of metal powder, layer on top of layer, into a solid part. The early generations of L-PBF systems were suitable mostly for prototyping purposes and niche manufacturing applications. In the 2020's, these days are long gone. Decades of development by equipment manufacturers and researchers have enabled L-PBF to reach the level of productivity, quality, and repeatability required of industrial serial manufacturing.

At EOS, this repeatability and quality of parts is maintained with a "quality triangle" system for quality assurance, where the quality and repeatability of the L-PBF built parts are ensured by quality control of three aspects of L-PBF manufacturing – the system, the process, and the material (i.e., powder) as is seen in Figure 1. [3] This thesis focuses on the "Material" -portion; the powder feedstock and more precisely its behaviour in the powder bed of the L-PBF system.

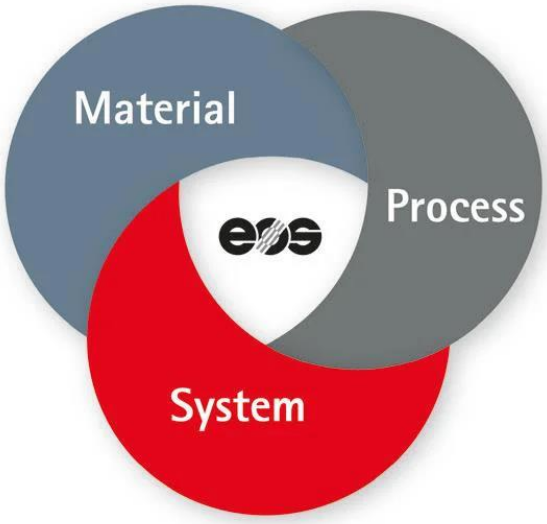

Figure 1 EOS quality triangle; quality assurance of the system, process parameters, and powder. [3]

In the quality triangle system, the powder feedstocks are given a technology readiness level to describe the amount of data available on the materials and their maturity for use in serial manufacturing. The powder materials featured in this thesis are the EOS NickelAlloy IN718 (IN718) which has a high technological readiness level, and EOS Tungsten W1 (W1) which has a lower technological readiness level for serial manufacturing. Both materials are representative of the expansion of L-PBF applications into serial production as well as enabling entirely new kinds of produced goods; IN718 is used for serial production of e.g., gas turbine components, which is a prime example of the viability of L-PBF in mass manufacturing. [4, 5] Tungsten on the other hand is not widely utilised despite its excellent properties in high-temperature environments and radiation attenuation, mainly because Tungsten is challenging to process using conventional manufacturing methods. There is therefore interest for manufacturing complex, functional Tungsten parts using L-PBF in energy-, medical-, and other industries. However, Tungsten is a challenging material in L-PBF as well; the rheological properties of the powder are not optimal and cracking during the L-PBF process is a persistent problem. [6] Plenty of research and development is therefore needed to bring W1 to the level of mass manufacturing seen with IN718.

To achieve this, all three aspects of the quality triangle seen in Figure 1 must be tailored into a single optimised set of parameters. Testing different combinations of material properties and process parameters for each L-PBF system means countless iterations of practical experimentation, which is costly. If some of these experiments could be replaced by simulations, it could mean significant savings in the cost of material research and development.

That is the motivation behind this thesis. The goal is to develop a validated simulation model of the behaviour of powder feedstock in the L-PBF system, answering these research questions:

- Can it be confirmed that the models produced with FLOW-3D DEM truthfully represent the behaviour of powder in the real process?
    - A powder bed characterisation method for validation must be developed if applicable methods do not exist.
- What data or methodology should be used to accurately define the input parameters?
- Is simulation a feasible tool for iterative L-PBF powder feedstock development?
    - Needs to be an improvement over current experimental methods in terms of required time, resources, and extractable information.

2 Powder properties

L-PBF uses metallic powder as feedstock for manufacturing parts. The properties of the powder feedstock mostly define the roughness, density, and uniformity of the powder bed, and have a large role in determining the porosity, mechanical properties, and dimensional accuracy of the finished part [7, 8]. Knowing the relevant powder material properties and how to characterise them is therefore essential for successfully applying the L-PBF process. The most important powder properties are the particle size distribution (PSD) and the particle morphology, which largely dictate the powder bulk behaviour. [9]

Much of the terminology and characterisation methods in L-PBF are borrowed or modified from the mature powder metallurgy industry. The international standard ISO/ASTM 52907:2019 [10] standardises feedstock-related terminology and characterisation methods for the AM industry.

2.1 Powder production

Powder is typically produced by a process called atomisation, where solid metal feedstock is melted and turned to fine droplets which quickly solidify into powder particles. Chemical reduction or milling are also used with certain materials. Powder properties such as morphology and the particle size distribution are mostly determined by the production method. Thus, powder feedstocks produced with different methods may have drastically different behaviour in L-PBF processing. For this reason, when comparing powder feedstocks it is important to know and understand how they are produced. [11] The common powder production methods are illustrated in Figure 2.

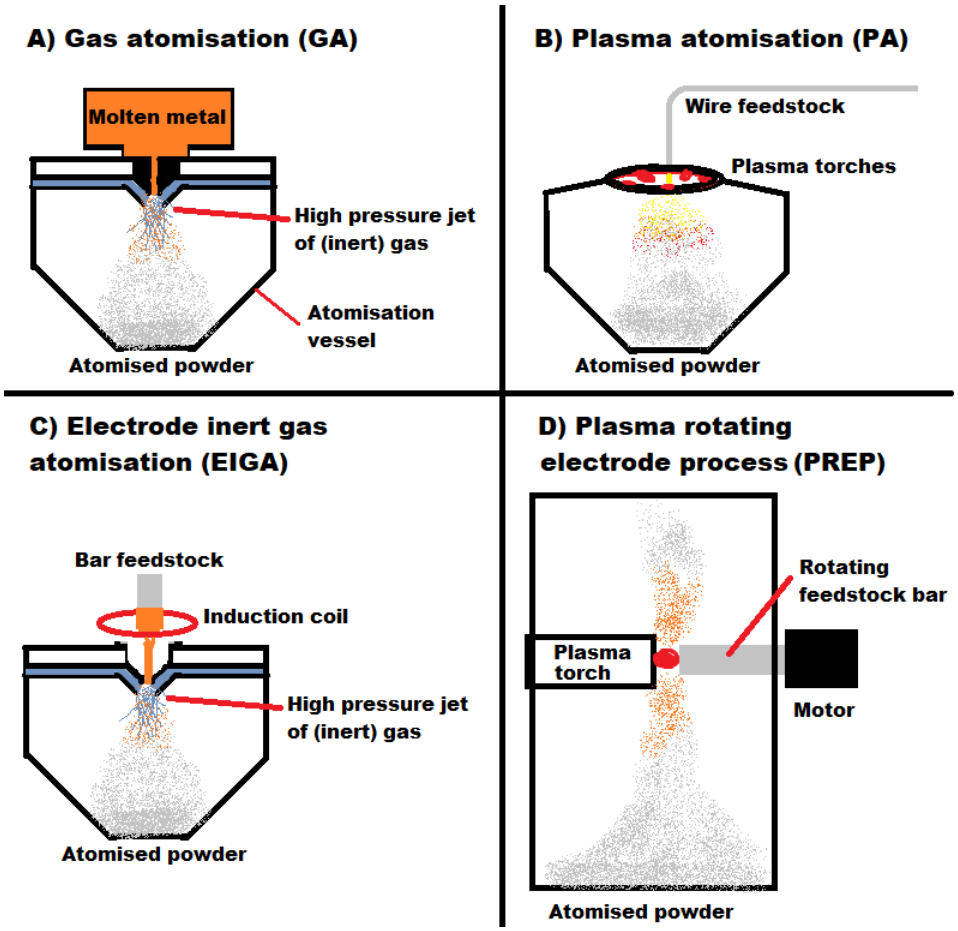

Figure 2 Illustrations of the common powder atomisation methods; gas atomisation, plasma atomisation, electrode inert gas atomisation and plasma rotating electrode process.

A typical production method for metal powder used in L-PBF is gas atomisation (shown in Figure 2 A), and less commonly water atomisation (GA and WA respectively). Molten metal is poured through a high-pressure jet of fluid (inert gas, air, or water), which breaks the metal into a fine spray that quickly solidifies into powder particles. For GA, particle shape is relatively spherical, throughput is high, but morphological defects are common and the PSD is wide. An example of the particles in GA powder is given in Figure 3 B. WA has comparable properties, though particle shape is irregular, and only non-reactive materials can be used. [7, 12, 13]

In plasma atomisation, a thick wire is slowly inserted into a plasma arc, where it is melted and atomised, as seen in Figure 2 B. The process produces spherical, high-purity powder, but is slow and expensive. A method called electrode inert gas atomisation (EIGA), as seen in Figure 2 C, uses a slowly rotating bar which is melted via induction and the dropping melt is atomised with a gas jet. The produced powder is spherical and high-purity, but the range of particle sizes is wide. [7, 13, 14] A process called plasma rotating electrode process or PREP is shown in

Figure 2 D. It utilises a quickly spinning metal bar which is melted by a plasma torch. PREP produces spherical high-purity powder, though with larger particle sizes. [7, 14]

Besides atomisation, it is possible to use mechanical milling or chemical processes to produce metal powder, which is uncommon for L-PBF feedstocks with the exception of Tungsten powder feedstocks. These methods usually produce irregular, polyhedral particles similar in shape to gravel. [15] An example of chemically reduced powder is shown in Figure 3 A.

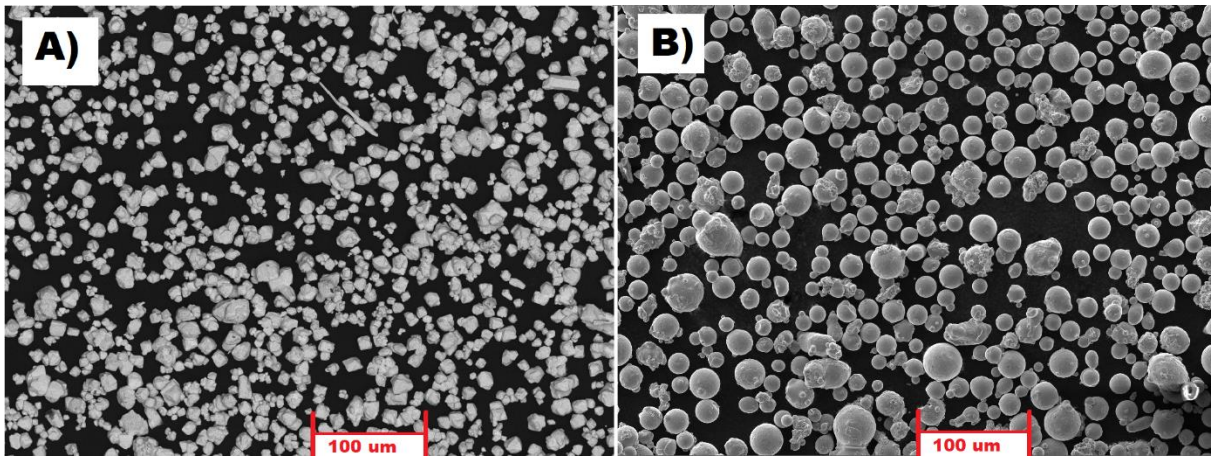

Figure 3 Micrographs of A) chemically reduced, irregular and B) gas atomised, spherical particles.

As seen in Figure 3, the production method has a significant impact on the particle shape. Chemically reduced powder (A) is irregular and polyhedral, in contrast to the GA powder (B) which is mostly spherical. The particles in image B feature defects typical to GA.

2.2 Bulk properties of powder

The bulk properties of powder define how the powder behaves during pouring and recoating. In L-PBF, bulk properties are described with the terms flowability, spreadability, and packing.

2.2.1 Flowability and spreadability

The terms flowability and spreadability are often used when describing powder behaviour. A rule-of-thumb explanation for these terms was given by Desai et al. (2019) [16], who summarised flowability as the ease of powder flow under the force of gravity, and spreadability as the ease of powder spreading under an external shear force in addition to gravity.

There are no units or strict definitions for either metric. They are qualitative compound properties formed by the PSD, morphology, friction, and adhesive forces of the powder

particles. [17, 14] Some attempts have been made to quantify these properties. For example, the standard ASTM B213-20 [18] defines a method of measuring powder flowability with the Hall flowmeter, which is a measure of how many seconds it takes for 50 g of powder to flow through a funnel. However, the Hall flowmeter was developed for the needs of traditional powder metallurgy, where the powder flow through a funnel into a mould was important. As discussed by Hryha & Riabov (2022) [14] this flowability metric can be considered insufficient when applied to L-PBF; the Hall flow measurement does not accurately predict powder behaviour under shear forces during recoating and is therefore not a direct measurement of powder spreadability, but at best a comparative metric of flowability. Other ad hoc methods, such as angle of repose, dynamic repose angle, and angle of avalanche measurements have been used to characterise the flowability and spreadability of L-PBF feedstocks [19, 20, 21, 22, 23].

Commercial flow- or spreadability test devices such as rheometers and shear force -based tests have also been developed. A rheometer such as the FT4 (Freeman technology, United Kingdom) works by spinning a "propeller blade" down into a container filled with powder and then pulling it back upwards, while measuring normal force and torque on the propeller shaft. This gives the basic flow energy *BFE* [mJ] and specific energy E_m [mJ/g], which provide information on powder flowability and cohesiveness under compression and in free flow respectively. A toothed shear blade and a flat plate can also be rotated on top of the powder bulk under various forces of compression to provide information on the internal friction and wall friction respectively. This kind of segmented flowability testing breaks the flow- and spreadability properties down into separate, quantitative parameters. [17, 20, 22, 23, 24, 25]

2.2.2 Packing behaviour

In L-PBF, powder feedstocks which easily settle into a tightly packed form are preferred, as densely packed powder absorbs more energy from the laser beam and produces denser parts. Powder packing density is difficult to measure during L-PBF processing and it can depend on many factors, but general packing behaviour can be expressed with apparent density and tap density. Apparent and tap density refer to the mass of bulk powder that is needed occupy a unit of volume [g/cm^3], or as a percentage of the total volume that is occupied by particles [%], which enables comparison of apparent/tap densities of different powder materials. These two values and their ratio give direct indication to the compressibility of the powder, i.e., how densely the powder material is packed under different circumstances. [26]

Apparent density is the packing density of powder that is allowed to settle under gravity. It can be considered the lowest limit for powder packing density during L-PBF processing, as no mechanical stimulation that might increase packing density are applied on the powder. [27, 28] Apparent density is typically measured according to standard ASTM B329-20 [28].

Tap density on the other hand is the density of bulk powder that has been agitated by tapping to the point of maximal packing. It can be considered the upper limit for powder packing density since the powder undergoes more intense compaction than can be expected during L-PBF. [27, 29] Tap density is typically measured according to standard ASTM B527-22 [29].

The ratio of apparent and tap density is called the Hausner ratio, which essentially describes the compressibility of the powder. If a powder does not change its volume after any time of tapping, i.e., it is incompressible, the Hausner ratio would be 1. A high Hausner ratio has previously been considered to indicate good flowability, but it has been found to agree poorly with other rheological measurement methods that are more representative of the L-PBF process conditions. Many authors have found it to be an unreliable metric for spreadability and flowability in L-PBF. [14, 20, 30]

2.3 Particle size

In practice, powder atomisation does not produce a certain size of powder particles, but a distribution of particle sizes. This distribution, called particle size distribution or PSD, is one the most important powder parameters in L-PBF. Typical characterisation methods include laser diffraction and dynamic image analysis. An overview of particle size characterisation techniques and their effects on the measured values of PSD is provided in Appendix 1. PSD is often idealised as a normal distribution where the median, mode and mean particle sizes are the same, as shown in Figure 4, though this is rarely the case in reality [12, 24].

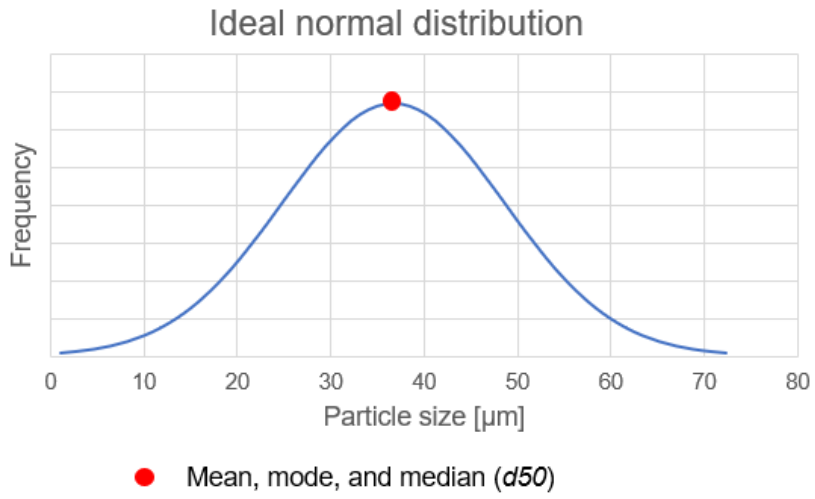

Figure 4 An example of an ideal normal distribution PSD with mean, mode and median marked.

As seen in Figure 4, an ideal normal distribution has a symmetrical bell curve, where the mean, mode, and median are identical. However, the PSD is rarely ideal, it is often more or less skewed or sometimes multimodal, as shown in Figure 5.

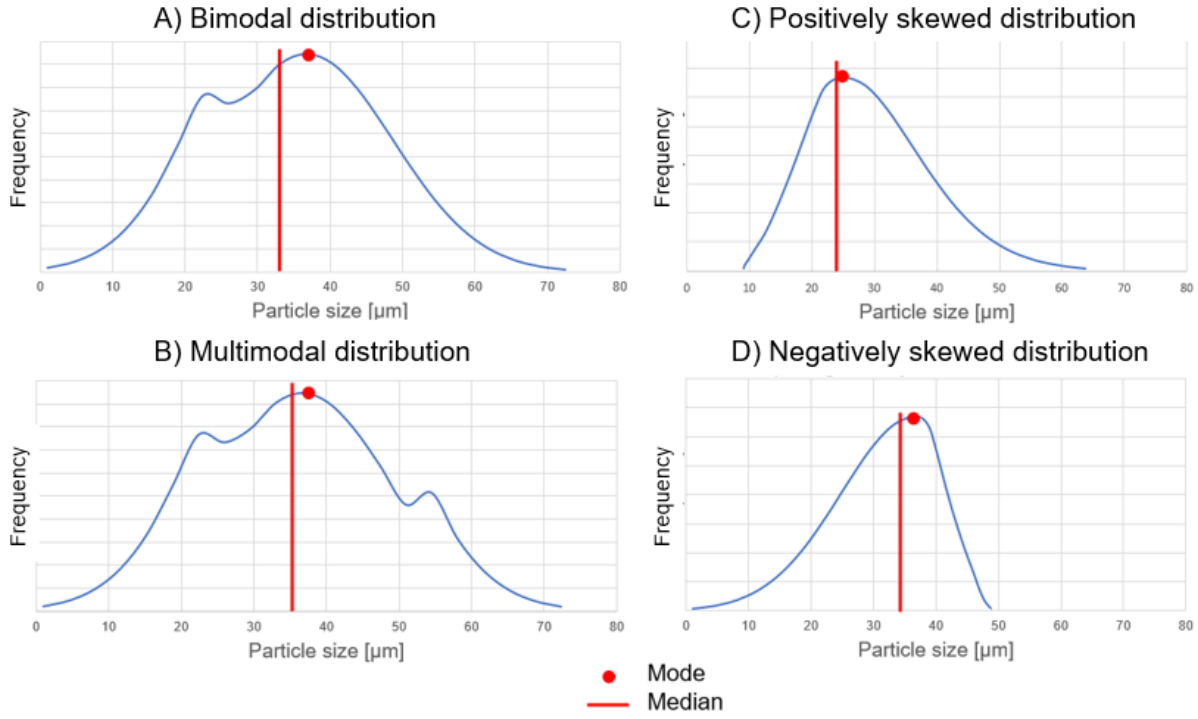

Figure 5 Example PSD with A) bimodal, B) multimodal, C) positively skewed, and D) negatively skewed distributions. Mode and median are marked with red.

As shown in Figure 5, the mode of a skewed distribution is larger or smaller than the median, called negatively skewed and positively skewed respectively. A multimodal distribution on the other hand has multiple modes. The most common multimodal distribution in L-PBF feedstocks is the bimodal distribution. [12, 24] As seen in Figure 5, the modality or skewedness of the PSD influences the median particle size, even if the PSD extents or mode do not change (e.g., between A-B). In addition to a bell curve, the PSD is often expressed on a cumulative curve, seen in Figure 6.

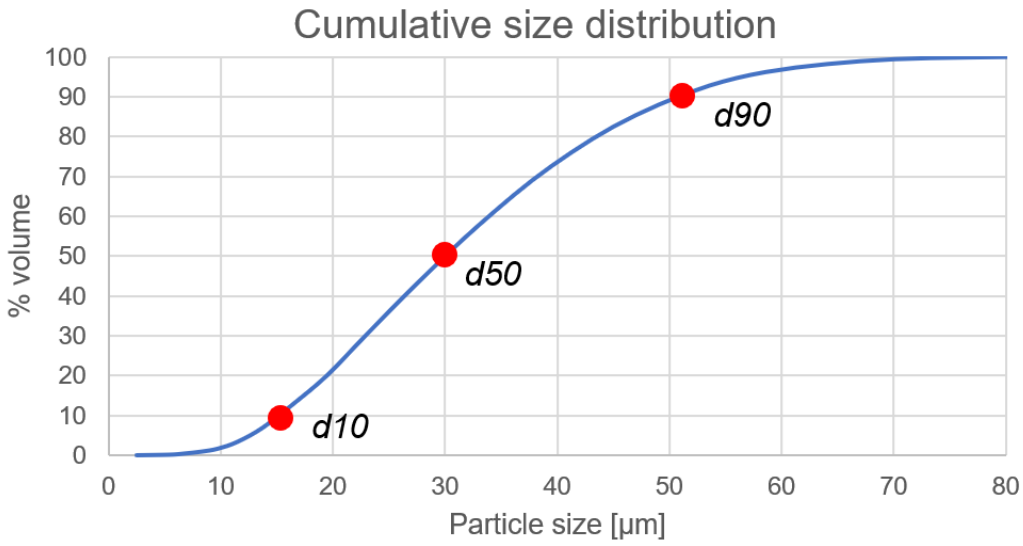

Figure 6 A cumulative distribution of an example PSD, demonstrating *d10, d50* and *d90.*

Cumulative curves can be used to read different percentiles of size classes as seen in Figure 6. The median, i.e., the top 50th percentile of particle sizes, is called the *d50*. *D50* is commonly used for describing overall powder coarseness. Other particle sizes that are commonly used to describe a powder feedstock are the top 90th and 10th percentiles *d90* and *d10*. *D90* is the size of a particle that is larger than 90% of all particles, and *d10* is the size larger than only 10% of particles. The size of *d10, d50, d90*, or any other particle percentile can be directly read from a cumulative curve. In this example, *d10* ~ 15 µm, *d50* ~ 30 µm, and *d90* ~ 51 µm.

The particle sizes in powder used in L-PBF are typically in the range of 10-70 µm. The size of largest particles are limited by the height of the powder layer as otherwise they would be scraped away by the recoater, and the size of smallest particles is limited by the increasing relative strength of interparticle attractive forces, an increasing risk of health issues for the L-PBF system operators, and the powder production processes themselves [11, 24, 31, 32].

Multiple studies have been carried out to optimise PSD, mainly for improving processing speed, density, surface roughness, or dimensional accuracy of finished parts [24, 33]. Powder with a wider PSD has been reported to provide a higher powder bed packing density compared to narrower PSD, since the small particles can fill the voids formed between larger particles. A wide PSD can therefore be expected to produce finished parts with less porosity. [9] However, the findings of Spierings et al. (2011) [34] suggest that the large particles of a wide PSD may not be needed at all, and it is only the small particles of the wide PSD that contribute to enhanced density and mechanical properties of finished parts. A PSD with mostly small particles may introduce problems though; smaller particles are more strongly affected by interparticle attractive forces, which can cause agglomeration and poor flow behaviour during recoating [33, 35]. Coarse and narrow PSDs on the other hand are found to improve flowability while packing density decreases. PSD optimisation can be considered a balancing act between good flowability and good packing density. [30]

Multimodal PSD has been investigated to improve packing density with a lower impact on flowability. A bimodal distribution has been found to provide higher powder bed density and produce up to 30% stronger parts due to reduced grain size, increased density, preferentially oriented precipitates, and weaker grain texture in comparison to monomodal PSD of similar width [8, 36]. However, Haferkamp et al. (2021) [32] found that a bimodal powder had no improvement in part density, but slightly worse flowability compared to monomodal powder.

PSD is not static throughout the lifespan of the powder. Reusing powder that has been already used in a L-PBF process before tends to skew the PSD towards larger particle sizes. This can happen due to particles larger than the layer height being swept away in recoating instead of being melted in the build process, leading to a higher concentration of large particles in the reused powder. The heat of the meltpool may also cause pre-sintering of nearby particles, or molten material may escape the meltpool and fuse to adjacent particles, forming large agglomerates. Sieving and mixing with virgin powder can alleviate the skewing of the PSD, and they are commonly done in commercial L-PBF manufacturing. [11, 12, 30, 33]

2.4 Particle morphology

Particle morphology in L-PBF refers to the sphericity of particles and the frequency, type, and severity of defects in the particles. Powder morphology can be determined visually with optical or scanning electron microscopy (SEM), or with dynamic image analysis. [37]

Most L-PBF powder feedstocks are predominantly spherical or near-spherical, but some water- and gas-atomised, milled, or reduced powder feedstocks may include irregular polyhedral shapes, blobs, and high aspect ratio particles or even rods. [37] Spherical particles may also feature defects which reduce their practical sphericity, as shown in Figure 7.

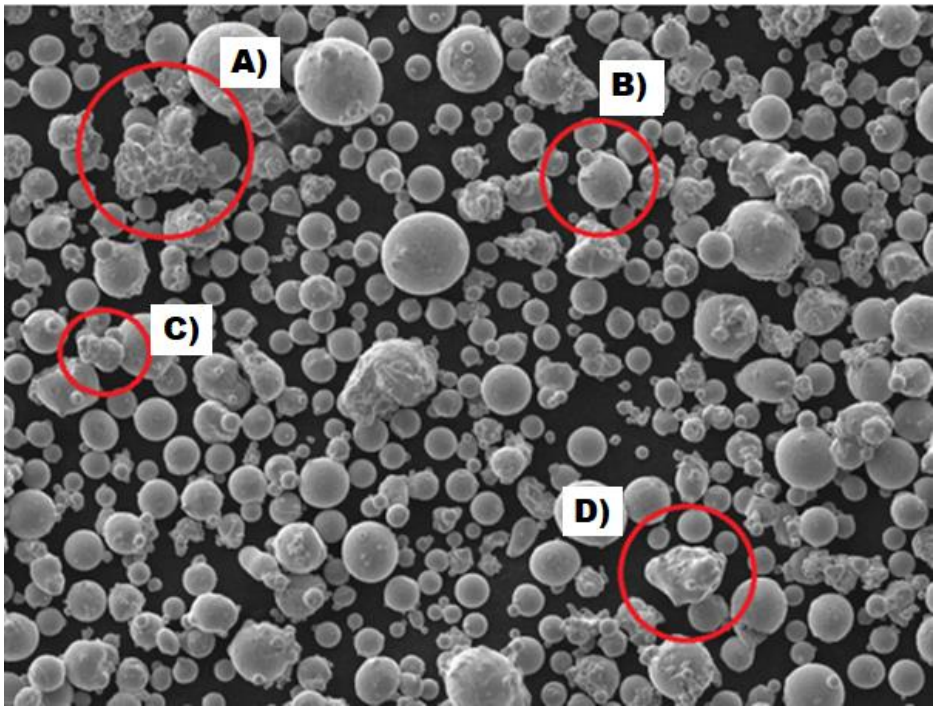

Figure 7 Examples of common defects in GA powder. A) agglomerate, B) satellites, C) conjoined particles, D) irregular particles

A common such defect is the satellite which can be seen in Figure 7 B. Satellites are small particles that become welded to a larger particle in the atomising process. Larger particles can also fuse to each other, creating large joint particles (Figure 7 C) and agglomerates (Figure 7 A) which degrade powder flowability and spreadability. Sometimes blob-like or otherwise irregular particles may form (Figure 7 D). [12] The surface roughness of the particle also may vary by production method [38].

High sphericity and smoothness of powder particles is generally considered ideal for L-PBF feedstocks. Flowability of coarse powder is improved as smoothness increases, but for fine powder there are some conflicting reports suggesting ellipticity and roughness may in fact improve flowability [30]. Smoother, spherical particles have been found to have a slight but undeniable advantage in terms of creating a smooth, dense powder bed. However, the significance of production method and shape of the particles becomes less pronounced

compared to other parameters, once the particles are predominantly spherical with only occasional defects. [38, 39]

Reusing powder in L-PBF can negatively affect its morphology, as the reused particles may feature bumps, tears, or notches. [33] Spherical particles may also become more elliptical [30].

2.4.1 Porosity

In addition to external defects, the particles may also have internal porosities that are not observable from micrographs. Porosity can be characterised by comparing the nominal material density of fully dense bulk material to the measured particle density, which is called skeletal density (ρ_s) [g/cm^3]. It is determined by pycnometry, which works by placing the powder sample into a vacuum, and flooding the sample with inert gas of known pressure and volume. Knowing the volume of gas spent on filling gaps between powder particles, the volume occupied by the particles themselves can be determined. This volume and the known mass of the particles are used to calculate ρ_s. The major difference compared to the nominal material density is that ρ_s accounts for internal porosities resulting from e.g. the atomisation process. Particle porosity can therefore be estimated from the difference between nominal material density and ρ_s. High porosity in particles is unwanted, as it may translate to increased porosity in the finished parts. [7, 27, 40]

3 Powder bed properties in L-PBF

A powder bed is created by recoating powder onto the building platform. It is then exposed to the laser beam for creating a melt track and fusing powder into a finished part. This means that the powder bed connects the finished part to the powder material and the process parameters. Therefore, to use a simulation model for predicting the effect of powder properties on the finished parts, it is necessary to somehow characterise and evaluate the powder bed. Understanding the recoating event and the effects of processing parameters, such as recoating speed and layer height, is also useful. An overview of the L-PBF process and powder bed recoating is provided in Appendix 2.

However, there are no standardised parameters for characterising L-PBF powder beds. For this reason, review papers on powder bed parameters were studied to find previously defined parameters that can be used to characterise powder beds. The effects of these parameters on finished parts were also looked at, to find which parameters are more relevant for describing the ability of a powder bed to produce mechanically strong parts. Then, review papers and research articles were reviewed to learn how powder bed parameters are affected by external factors that are irrelevant for the purposes of this thesis, and whether the powder bed parameters affect each other. Based on the results of this review, two parameters were chosen for a more in-depth literature review to find methods for measuring them.

3.1 Powder bed parameters in literature

Multiple powder bed parameters were found in literature, of which two were especially common and seemingly practical: powder packing density and surface roughness.

- Powder packing density *PD*: Density of powder in the powder bed. Measured as density [g/cm^3] or the volume percentage of space occupied by particles [%]. [20, 22, 33, 41]

- Surface roughness *SR*: the variability of the powder bed surface. Measured by e.g., average roughness or height difference of lowest and highest points. [20, 22, 33, 41, 42]

Other found parameters included the frequency of defects and layer height accuracy. However, these are heavily influenced by process parameters which makes characterising them less interesting from the powder development point of view. [22, 30, 33] However this could mean that they are useful for characterising powder beds in the context of process parameter development, though that is not within the scope of the thesis.

As illustrated in Figure 8, powder properties at particle level control its bulk behaviour, i.e., the flowability and spreadability. Some process parameters such as layer height and recoater material are also dictated by the particle properties. Together, the bulk powder properties and process parameters control the properties of the powder bed; roughness, density, frequency of defect, and the accuracy of the layer height. These powder bed properties (and the material properties of the used alloy) influence the absorptivity and conductivity of thermal energy from the laser beam, as well as the porosity, dimensional accuracy, and microstructure of the finished part. [33, 43] This chain from the particle properties to the mechanical properties of the finished part is shown in Figure 8 as parameter dependencies, i.e., top parameters are most fundamental, and parameters below them are derived from them as demonstrated with arrows. Figure 8 was collated and adapted from [20, 30, 33, 38, 41, 44, 45, 46, 47, 48, 49, 50].

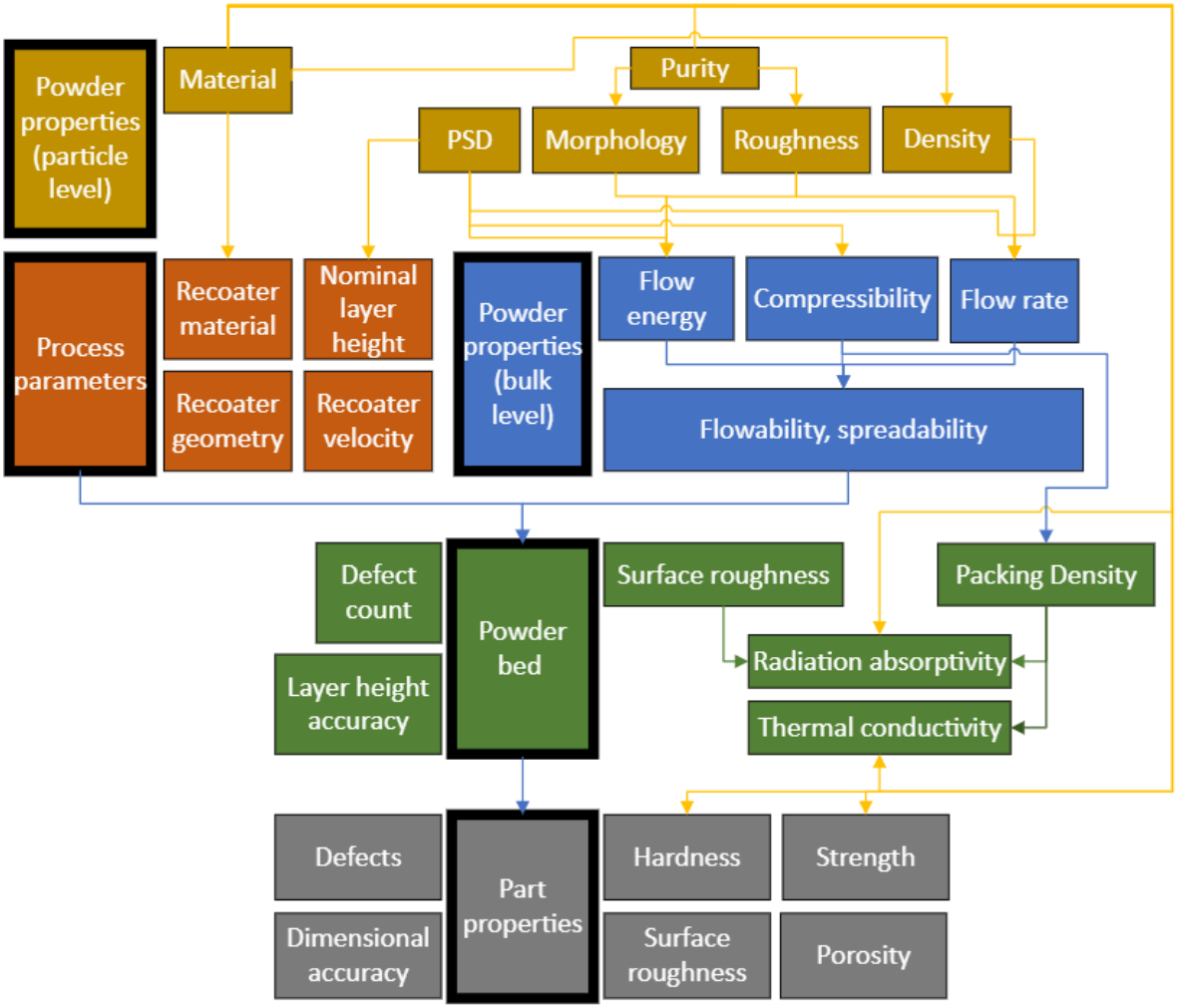

Figure 8 Visualisation of main parameters of powder, process, powder bed and finished parts.

3.1.1 Factors affecting powder bed parameters

As is seen in Figure 8, the powder bed parameters are most significantly affected by the powder properties and process parameters. A literature review was conducted to find all relevant factors affecting the powder bed parameters and their possible interdependencies, i.e., how and if the values of *SR* and *PD* depend on each other.

Powder properties

The properties of the powder feedstock have arguably the most influence on *SR* and *PD*. The most important powder properties and their relationship with these powder bed parameters are given in Table 1 [9, 30, 33, 34, 35, 38, 39, 50].

Table 1 Relationship of powder properties and powder bed parameters.
"Relation" means that increasing the parameter of the row increases the parameter in the column. "?" indicates that some conflicting information the relationship was found.

Powder property		*SR*	*PD*
PSD	Wide	Relation?	Relation
	Narrow	Relation?	Inverse relation
Sphericity		Inverse relation	Relation
Particle surface roughness		N/A	Inverse relation

As seen in Table 1, the PSD of the used powder has a complicated relationship with *SR* and *PD*. Wide PSD decreases the flowability of the powder, which can increase *SR* [30, 33, 35] but also increase *PD* as small particles fill gaps between larger ones [9, 33, 34]. However, this relationship is not entirely certain, as a narrow PSD was also found to lower *SR* in a study by Yim et al. (2022) [38]. Also, increasing the share of larger particles on its own may increase *SR* as surface height differences increase, but then again, a negatively skewed PSD may also increase flowability which may reduce *SR* [33]. Even though a PSD with more small particles has been found to increase *PD*, small particles may cause agglomeration and reduced spreadability, which may then also start to decrease *PD*. Findings of Chen et al. (2019) indicate that there may be a "Goldilocks zone" for PSD in terms of maximising *PD* [50]. All in all, PSD is a highly complex parameter and its relationship with the powder bed is worth a focused study on its own.

It is commonly thought that sphericity of particles is ideal for both *PD* and *SR* [33]. This has been confirmed in practical experiments as well, though the impact of sphericity was found to be overshadowed by the impact of changes in PSD [38]. Sphericity is therefore a well understood factor, but its significance for *PD* and *SR* is slight.

High surface roughness of the particles themselves also has been found to reduce *PD*, but again the significance is low compared to that of PSD [38, 39].

External factors, process parameters

Besides the powder properties, there are other factors which may change with the L-PBF system, process, location, or powder handling procedure. The ones commonly recognised in literature are humidity, recoating velocity, and layer height. Their relationships with the powder bed parameters are presented in Table 2, compiled from [33, 41, 46, 47, 51, 52, 53]

Table 2 Relationship of external factors, process parameters and powder bed parameters

Powder property	*SR*	*PD*
Humidity	Relation	Inverse relation?
Recoating velocity	Relation?	Inverse relation?
Layer height h_l	Inverse relation	Relation?

As seen in Table 2, humidity has an overall negative effect on both powder bed parameters. Exposure to humid air increases surface energy between the particles, causing agglomeration and poor flow and spreadability which leads to higher *SR,* and logically lower *PD* too, though this review did not find conclusive experimental data on the effect of humidity on *PD*. [33, 51]

Recoating velocity has been commonly thought to increase *SR* and lower *PD* [33], but in a study by Chen et al. (2022), the negative effect of higher recoating speeds is very limited in the large scale, and the initially low true layer height h_{lt} and *PD* normalise within the first 10 layers [41].

Increasing layer height h_l has been found in multiple studies to increase *PD* [47, 52, 53]. However, Choi et al. (2017) [46] found no increase in *PD* when h_l was doubled or tripled, which may indicate the relationship is more complicated than assumed. No clear evidence was found of h_l having a major effect on *SR*, though it should be noted that h_l probably should not be smaller than the largest particles in the powder, as this may cause drag marks or other defects during recoating, which will increase *SR*. Wu et al. (2022) [52] also found higher h_l to reduce

compressive forces acting on particles during recoating, which may reduce the likelihood of defects on the powder bed surface.

Interrelations

A more complicated relationship affecting these two powder bed parameters was discovered during the review; low *SR* and high *PD* correlate with each other, but the mechanics of the relationship are uncertain. This phenomenon has been successfully used to characterise *PD* by non-invasive *SR* measurement alone [48]. However, there was no definitive answer to which causes which, or are both result of some powder property or process parameter.

3.1.2 Effect of powder bed parameters on finished parts

As it can be seen in Figure 8, the powder bed plays a major role in determining the mechanical properties of the finished part, in addition to the material properties of the particles. The influence of material properties to finished parts is outside the scope of this thesis, as it will be considered case-by-case when the simulation is applied to new powder materials.

The relationships of powder bed parameters and the mechanical properties of finished parts are of interest in this thesis, as the chosen powder bed parameter should ideally be relevant for evaluating the quality of the powder bed for producing functional parts with strict requirements for mechanical properties. The results of this review [33, 44, 45] are shown in Table 3.

Table 3 Relationships of mechanical properties and powder bed parameters.

Powder bed parameter	Porosity	Tensile strength	Hardness	Part surface roughness	Dimensional accuracy	Defects
SR	Relation	Inverse relation	N/A	Relation	Inverse relation	Relation
PD	Inverse relation	Relation	Relation	Inverse relation	Relation	Inverse relation

As seen in Table 3, both parameters affect different aspects of the laser-material interaction as well as the mechanical properties of the resulting part. Increasing *SR* is shown to have a direct negative impact on almost all listed mechanical properties, except for hardness, for which no connection has been found in the articles reviewed by Avrampos & Vasniakos (2022), Sanchez et al. (2021), and Gor et al. (2021). Variations in powder bed surface can directly transfer to variations in the surface of each fused layer, which interferes with the deposition of the next powder layer and contributes to dimensional inaccuracy. Variations in surface height can also

momentarily change the focus of the laser beam, creating a discontinuity in laser energy density. Therefore, *SR* should always be as low as possible. [33]

PD seems to affect most aspects of the finished part. One major reason is that since low *PD* means there are more voids in the powder bed, it is linked to increased porosity in the finished part. High porosity is a critical weakness that will also degrade other mechanical properties. Increasing the *PD* is also found to improve absorption of energy from the laser beam [54]. *PD* should therefore be maximised when possible. [33, 45, 55]

3.1.3 Conclusions

Based on this review, *PD* and *SR* are relevant parameters for characterising powder beds in the context of powder development, as these parameters are mostly influenced by the powder properties, though the possible effect of process parameters and humidity should also be acknowledged. *PD* and *SR* also control many critical mechanical properties of the finished part, which increases their usefulness as descriptors of the quality of a powder bed for successful L-PBF processing. [22, 33, 30]

PD and *SR* were therefore chosen as the focus of further literature review aimed at finding practical powder bed characterisation methods used in previous works. However, it was ultimately decided that *SR* would not be characterised in the experimental portion of this thesis. Findings for *PD* are presented below, and the results regarding *SR* are included in Appendix 3: Surface roughness as a powder bed parameter for potential future application.

3.2 Characterisation of powder packing density

Powder packing density *PD*, also called packing fraction, can be calculated as Equation 1 shows. Here, V_{powder} is the volume occupied by powder particles in V_{sample} which is the sampled volume of the powder bed [55].

$$PD = \frac{V_{powder}}{V_{sample}} \quad (1)$$

There are no standardised methods of measuring powder bed packing density in L-PBF, despite its significance in most aspects of the L-PBF process. Therefore, many authors have developed their own methods of characterising *PD*, which are presented in Table 4. All powder bed AM technologies were included in this review, as well as generic ad-hoc test rigs, marked with a dash (-). It should be noted that methods developed for polymer powder bed fusion and binder

jet AM may not be applicable for metal materials and L-PBF, though these studies still give valuable insights into the extraction of powder samples and the possible sources of error.

Table 4 Powder bed characterisation methods; results of literature review.
PD = packing density, *SR* = surface roughness, h_{lt} = true layer height

Author, year	Property	Method	AM	Remarks	Ref.
Lampitella et al. 2021	*PD*	Sample picker	L-PBF	Not thoroughly documented.	[56]
Jacob et al. 2016	*PD*	Closed container	L-PBF	Well documented, analysed.	[53]
Chen et al. 2019	*PD*	Open cups	L-PBF	Small cups to track variance of packing along recoater travel.	[50]
Elliott et al. 2016	*PD*	Open cups	Binder jet	Not suitable for L-PBF.	[57]
Oh et al. 2019	*PD*	Open cups	Binder jet	Studied effect of cup size on *PD*; tiny negative correlation.	[58]
Bochuan et al. 2011	*PD*	Open cups	L-PBF	Description of experiment lacking in documentation.	[59]
Rogalsky et al. 2018	*PD*	Open cups	L-PBF	Built on bolts for removal. CT scanned. Well documented.	[39]
Choi et al. 2017	*PD*	Open cups	L-PBF	Small cube cups, studied relation of layer height/*PD*, powder materials.	[46]
Haferkamp et al. 2021	*PD*	Pre-made open cup	-	Question if representative of L-PBF process. Single layer.	[32]
Ali et al. 2018	*PD*	UV-cured polymer	L-PBF	Extracted solid samples of bed in UV-cured polymer. Intrusive.	[60]
Li et al. 2019	*PD*	Impact penetrator	-	Steel ball dropped on bed. Needs calibration. Intrusive.	[61]
Chen et al. 2022	*PD*, h_{lt}	Staircase	L-PBF	Effect of recoating velocity on *PD, h,* mechanical properties. *PD* measured by weighing deposited layers.	[41]
Wu et al. 2022	*PD*	Staircase	L-PBF	Dynamics of particle-blade interaction with varying layer height. Thorough documentation, analysis	[52]
Wischeropp et al. 2019	*PD*, h_{lt}	Staircase	L-PBF	Study on finding true layer height and PD within single layers	[62]
Sillani et al. 2021	*SR, PD*	Profilometer	Polymer L-PBF	Pre-made cup, study on relation of *PD* and *SR*.	[48]

As seen in Table 4, the most popular *PD* characterisation method used in literature so far is the "open cup" method. In this case "open cup" refers to a method where the L-PBF process is used to build a small open-top container, which traps a sample of powder inside it as it is built. This is shown in Figure 9.

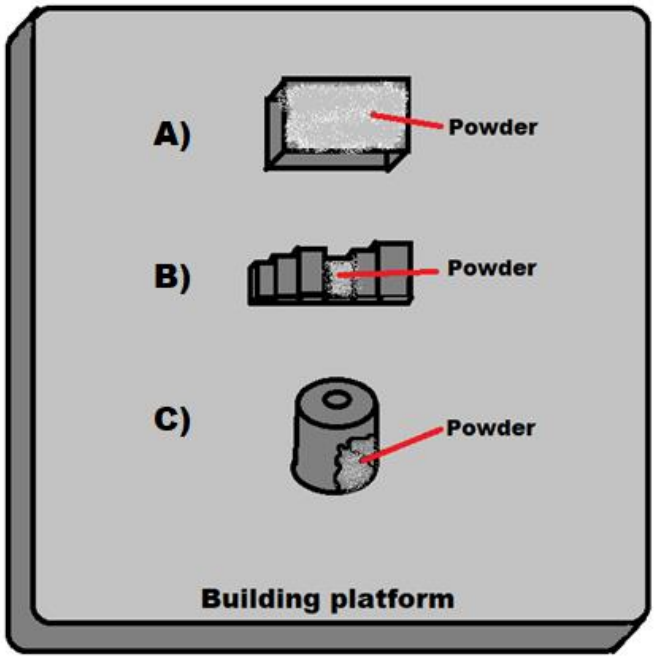

Figure 9 Examples of typical A) open cup, B) staircase, and C) closed container *PD* samples.

The open cup style of sample seen in Figure 9 A was by far the most common. However, Chen et al. (2022) showed that the staircase samples as seen in Figure 9 B, typically used for measuring h_{lt}, can be used for *PD* measurements as well. Haferkamp et al. (2021) used a pre-made, one-layer deep cup, in which case powder is simply recoated over the pre-made cup to determine the *PD* of a single layer. However, this method is inflexible and may not represent true L-PBF process conditions. In the case of L-PBF -built open cup and staircase samples, measuring the powder sample mass for determining *PD* often means weighing the entire building platform, as the cup samples cannot be detached without disturbing the contained powder. This process can be impractical and prone to error.

Jacob et al. (2016) presented a refined version of the open cup method which enables detaching the samples without disturbing the sampled powder. Their sample was a cylindrical, sealed container, as seen in Figure 9 C. The closed container was opened by punching open a thin lid at the top. Powder is poured out and the container filled with water to determine its volume. Intuitively, the method has a concern of powder getting stuck inside and water not filling the entire volume due to surface tension, however the authors present a thorough uncertainty study to increase confidence in the method. Lampitella et al. (2021) presented a custom-made sample picker device which allows the direct extraction of a powder sample from the bed. The method is quick and simple but may have increased uncertainty due to the manual operation of the hand-

held device. Li et al. (2019) used a specialised test rig which drops a steel ball onto the powder bed. The resistance of the powder can then be used to determine *PD*, provided that the rig is calibrated. Intuitively the system seems relatively sensitive to changes in powder bed depth but is otherwise likely robust to user error. Ali et al. (2018) developed a method of spraying UV-curable polymer onto the powder bed and studying the solidified powder bed samples with e.g., computed tomography scanning. The method provides versatile insights into the powder bed and should not allow for major human error but is complicated and expensive. There is also a question of repeatability and representativeness of true *PD*, considering the changes in volume and mass of the powder sample from the addition of a liquid and its solidification. Sillani et al. (2021) combined the *PD* and *SR* measurements by defining *PD* as a function of *SR*, though the exact mechanics of this relationship are uncertain.

4 Discrete element method simulation of the powder bed

The discrete element method (DEM), its first computer program application called “BALL”, and validation of the program were introduced in the works of Cundall and Strack in the 1970’s [63]. Since then, the method has seen widespread adoption and development in many fields such as geology, agriculture, and a variety of other industrial processes featuring discontinuous systems (i.e., individual, indivisible pieces and particles instead of mutable objects or fluids). [64, 65, 66] The core idea of DEM modelling is almost simple enough to work with hand calculations, but in practice real DEM models utilise complex contact models to simulate up to millions of particles interacting with each other and solid geometry over microsecond-scale intervals [21, 67, 68, 69]. The particles may be of any shape, but idealised spheres are commonly preferred as they are computationally easier. The initial location, size, shape, and material properties of each particle are known. Then, with Newtonian laws and kinematic equations, the particle trajectories can be determined based on the forces acting on them at each time step (gravity, collisions, inter-particle attractive forces). [68, 69]

DEM is a popular method for creating the powder bed in L-PBF simulations, thanks to its unrivalled realism. Dynamic modelling of particles settling into a powder bed is computationally demanding, but it is the only option to reach realistic particle packing. Using a predetermined (e.g., body- or face-centered) packing structure will result in an unrealistically high powder packing density, up to 30 percentage points higher than in reality. [70]

4.1 Contact modelling

Particles in DEM models are in near constant contact with each other, imparting kinetic energy on each other and dissipating it until the system comes to rest. The contact force model considered in this thesis is a linear spring-dashpot (LSD) Voigt model, which considers contact force as a combination of stored elastic force and viscous dissipation. Elastic force is modelled as a “spring” which stores and releases kinetic energy during contact and determines how much overlap between contacting particles is allowed. The “dashpot”, or damper, models viscous damping, which determines how much energy is dissipated during contact. These components are connected in parallel for both normal and tangential directions. The Voigt LSD model is illustrated in Figure 10. [71]

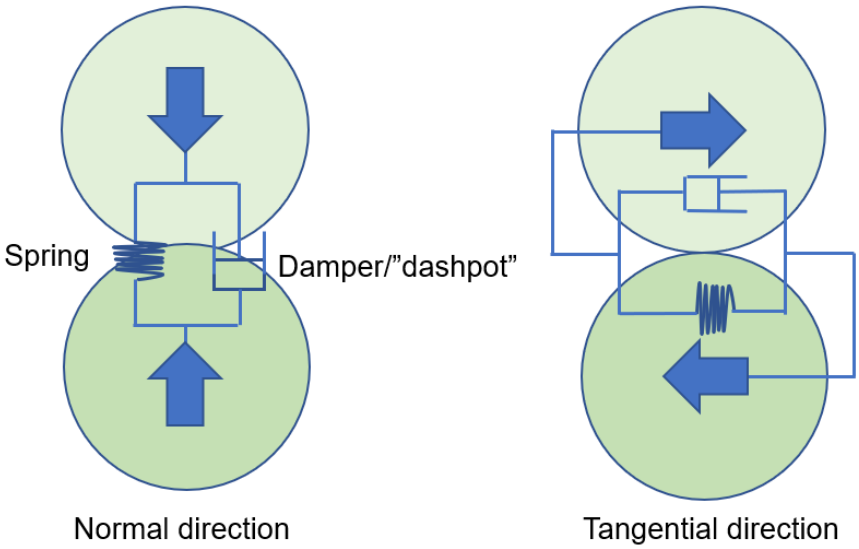

Figure 10 Illustration of the spring-dashpot contact model used in FLOW-3D [71].

4.1.1 Mesh and contact detection

The simulated volume is divided into cells which must be larger than the largest particle diameter. This process is referred to as meshing. The mesh can be composed of cells of different shapes and sizes, but they must form an uninterrupted mesh with no gaps or holes. The mesh determines the resolution of modelled geometry, as demonstrated in Figure 11 [72].

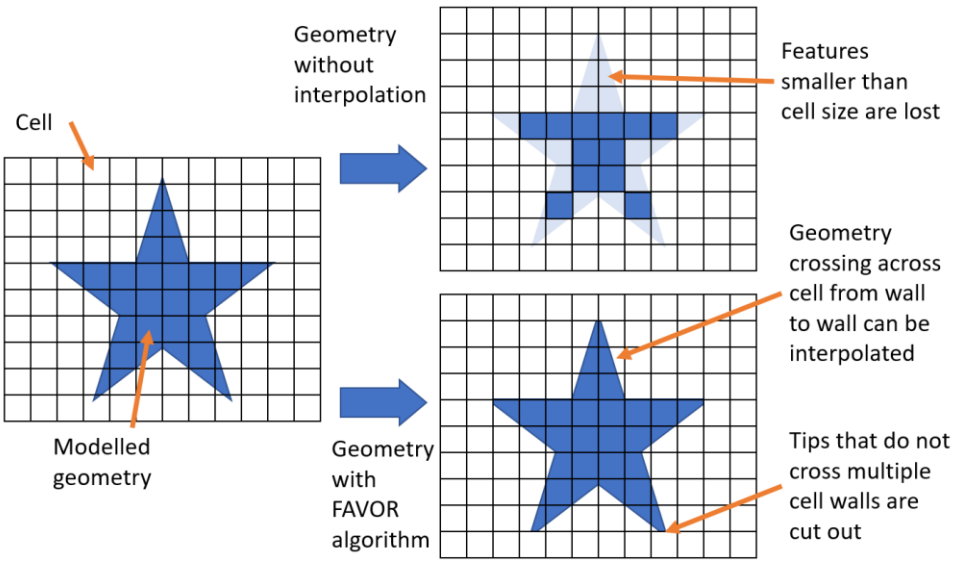

Figure 11 Effect of small cell size on geometry, with and without interpolating algorithms [72].

As seen in Figure 11, the cell size should be smaller than the geometry features, or otherwise the features may be lost. Some programs mitigate this problem with a process (such as FLOW-3D with its FAVOR-algorithm), which interpolates geometry in the middle of mesh cells.

The mesh is usually defined as a block, cylinder, or other simple shape. Multiple mesh blocks may also be connected to each other. The mesh surfaces are called boundaries and they must be given a boundary condition, which defines how particles are treated when they reach the mesh boundary. [72] Typical boundary conditions in L-PBF DEM models are the wall boundary condition and the outflow boundary condition. Wall boundaries are rigid boundaries which allow nothing through them. [71] Wall boundaries may be an appropriate choice for the side boundaries (xz-planes if the recoater moves along the x-axis) of a powder recoating simulation for example. Outflow boundaries on the other hand allow particles to pass through freely and leave the simulated domain permanently, which can be used to represent the end of the powder bed where powder in the real L-PBF system would be swept away into the collector bin. [71, 73]

At each time step, the DEM solver searches the mesh cells surrounding each particle. The search is only performed for those particles in cells immediately next to the searched particle (i.e., a nearest neighbour search), as shown in Figure 12. After finding a nearest neighbour particle (or solid object geometry), collision detection is conducted by comparing the added radii of the particles to the distance between the particle centres (or the radius of the searched particle and the distance to a solid object). [74]

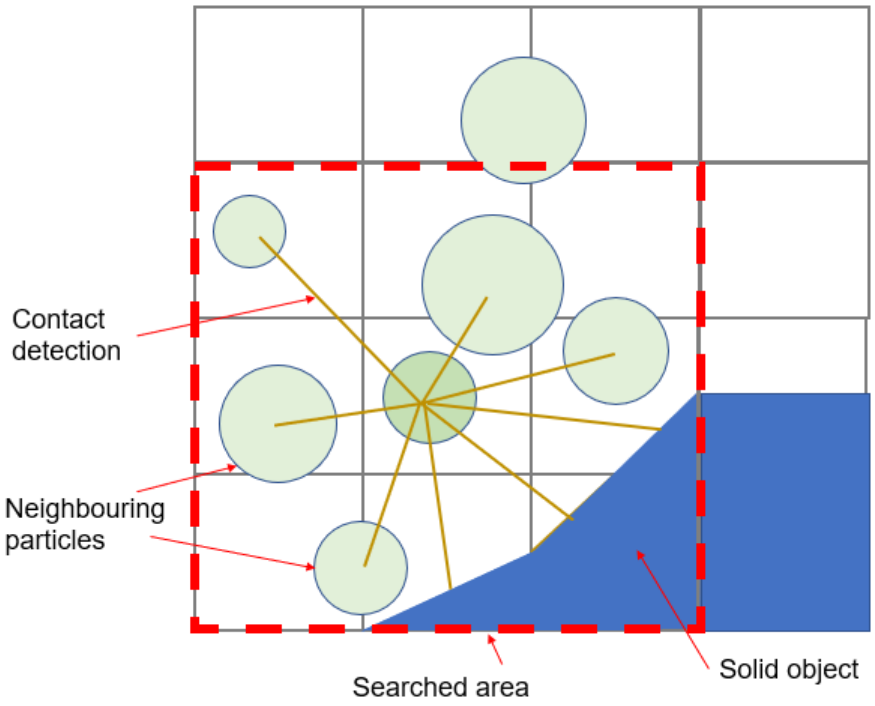

Figure 12 DEM contact detection in FLOW-3D [71].

4.1.2 Contact force modelling

If particle contact is detected, the rebound velocity and direction can be calculated based on the amount and direction of overlap between contacting particles (or particles and walls), the stored elastic force, and the amount of energy lost in viscous dissipation. [74] The overlapping emulates the deformation of particles, and therefore is dictated by the spring constant or other parameter describing particle stiffness (e.g., Young's modulus E) depending on the contact model used. These overlaps happen on the nanometre-scale, which means that extremely short time-steps must be used to "catch" each overlapping particle. [75] Therefore time-step length is determined by the overlap size. It is common to decrease the stiffness of particles and allow for larger overlaps than in reality to reduce runtimes. However, a maximum overlap in the range of 0.1-0.5% of the largest particle radius is recommended by Cleary (2010) [65] to prevent the low material stiffness from influencing bulk flow behaviour. This may seem like a uselessly small range, but for example in the case of Geer et al. (2018) [21] it translated to a usable range of E = 33-828 MPa for stainless steel particles; a significant reduction compared to the nominal value of E = 200 GPa.

The LSD Voigt contact model also accounts for energy dissipated due to friction. Friction is modelled in static and dynamic components. Static friction (μS) is the frictional force between

two bodies which are not moving in relation to each other. Dynamic friction (*μD)* is a force between two bodies with a velocity difference. Static friction affects objects with no velocity difference, while dynamic affects objects sliding against another surface. In this model, friction dissipates kinetic energy proportionally to the normal force pushing the objects against each other (in contrast to the tangential damping, i.e., viscous dissipation, which dissipates energy proportionally to the velocity difference of the objects rubbing against each other). [72]

Another force to consider when simulating μm-scale particles is attractive force. Since powder used in L-PBF is very dry, adhesion due to surface tension can often be neglected, leaving Van Der Waals forces (VDW) as the relevant attractive force [76]. Some authors such as Lee et al. (2018) [70] consider the use of VDW forces unnecessary with metallic particles well over ~1 μm in size, but some consider VDW a relevant cohesive force in particles up to 100 μm in size [23, 50]. Meier et al. (2019) [77] found that attractive forces are usually lower in reality than in theoretical models, due to surface irregularities and oxidation, which the DEM model would not account for.

4.2 Parametrisation

Necessary input parameters of DEM simulations depend on the type of used contact model and the level of detail in contact modelling. In the Voigt linear spring-dashpot model, viscous damping in normal and tangential directions is parametrised as the coefficient of restitution (*e,* [-]), and the elastic force as a spring constant (*k,* [N/m]). Friction is modelled as a dynamic and static friction between particles (*μDpp, μSpp* [-]) and walls (*μDpw, μSpw* [-]). Adhesive forces between particles are modelled as the surface energy (*SE)* [J/m^2]. The particle sizes and density are defined by the user.

Due to the difficulty and uncertainty of measuring most DEM input parameter values, a literature review was conducted to find DEM parameters used in previous works, as well as studies where DEM-applicable parameters such as *e* were characterised from metallic particles in the 10-100 μm scale, which corresponds to the particles found in typical AM powder feedstocks. The most relevant findings are presented in Table 5, and complete results can be found in Appendix 4.

Table 5 DEM input parameters from literature.

Table lists inputs used/calibrated in previous DEM simulation works as well as measured values (indicated with **). A single * indicates a rolling/sliding friction model as opposed to static/dynamic.

Author, year, material	ρ_s [g/cm^3]	*μSpp* [-]	*μDpp* [-]	*μSpw* [-]	*μDpw* [-]	*e* [-]	*SE* [mJ/m^2]	Ref.
Ganesan et al. 2022, IN718	8.2	0.005*	0.3*	0.005*	0.9*	0.35		[78]
Shaheen et al. 2021, IN718							0-0.4	[79]
Marchais et al. 2021, IN718	8.0					0.1	0-1	[76]
Lampitella et al. 2021, IN718	9.2	0.15*				0.7		[56]
Dai et al. 2021, IN718	8.2	0.51*	0.39*	0.05*	0.05*	0.3	0.1-0.5	[80]
Dai et al. 2019, IN718	8.2					0.3		[81]
Lee et al. 2018, IN718	8.1	0.2*	0.58*	0.2*	0.18*	0.75		[70]
Lee et al. 2018, 316L	7.9	0.2*	0.58*	0.2*	0.18*	0.75		[70]
Nguyen et al. 2017, IN718		0.4**	0.3**					[25]
Lee & Zhang 2016, IN718		0.3						[82]
Wang et al. 2020, HX	8.2	0.005*	0.3*			0.35		[83]
Han et al. 2019, HX	8.2	0.005*	0.4*			0.4	1.6	[84]
Yao et al. 2021, 316L	7.8	0.09*	0.6*			0.6	1	[85]
Xiang et al. 2021, 316L	7.8	0.1*	0.62*			0.9	0.1	[86]
Tian et al. 2020, 316L	7.9	0.62*				0.9	0.1	[87]
Chen et al. 2019, 316L	7.8		0.62*			0.9	0.1	[50]
Steuben et al. 2016, 316L	8.0	0.3						[88]
Li et al. 1999, 316L						0.6-0.8**		[89]
Yim et al. 2022, GA Ti48Al		0.2*	0.5*	0.6*		0.3		[38]
Yim et al. 2022, PREP Ti48Al		0.12*	0.31*	0.3*		0.2		[38]
Wu et al. 2022, Al		0.01*				0.7**	0.2	[52]
Phua et al. 2021, Ti6Al4V			0.12*		0.05*		0.5	[90]
Fouda & Bayly 2020 Ti6Al4V	4.3	0.01*	0.5*	0.1*	0.5*	0.5		[91]
He et al. 2020, Ti6Al4V	4.4	0.01*	0.3*			0.4		[92]
Meier et al. 2019, Ti6Al4V	4.4	0.4*				0.4	0.1	[93]
Desai et al. 2019, Ti6Al4V			0.19*		0.12**			[16]
Marinack et al. 2013, steels						~0.7**		[94]
Marinack et al. 2013, WC	15					0.55**		[94]
Tolias et al. 2017, W						0.45-0.8**		[95]
Ratynskaia et al. 2015, W						0.3**		[96]
Wagner 1983, W					~0.2**			[97]

As shown in Table 5, the most commonly used or characterised material properties are ρ_s, μS_{pp}, μD_{pp} and e. In all reviewed papers, friction was represented as a split into rolling and sliding friction, i.e., into a resistive torque and a resistive linear force respectively. These figures are marked with an asterisk (*), as they are not necessarily drop-in replacements (depending on the exact contact model used in each study) for the static and dynamic friction model which is used in this thesis. Some authors also used a single friction coefficient to dissipate energy in all particle-particle shearing contact [50, 76]. Interestingly, in studies where the rolling/sliding friction model was used, friction tends to play a larger part compared to those using a generic single friction coefficient, see for example Dai et al. (2019) [81] vs Marchais et al. (2021) [76].

Values for e were often approximated between 0.2-0.5, however in experiments of Li et al. (1999) [89] and Tolias et al. (2017) [95], values of e for particles of various alloys were found to be in the range of 0.45-0.8. A related value that is not featured in this table is the spring constant k. This is because k is typically kept as small as possible to reduce computation times without much regard for material properties. Values for μ or e characterised with practical experiments are marked with a double asterisk (**), as opposed to estimates or calibration.

Adhesive forces between particles can be modelled in various ways, for example as a force proportional to deformation in contact, or as a force based on surface energy, or as a force that is in effect over a certain particle-particle distance [98]. Characterising adhesive forces is difficult, and they are often excluded entirely from DEM models as seen in Table 5.

Parameters that are easily measured were excluded from the literature review. These include particle density and PSD. [71] Skeletal density ρ_s should be used as the particle density, to account for possible porosity within the particles. The sizes of particles can be modelled as set of size classes. For example, the measured real PSD can be divided into 10 particle size classes, which are given a concentration corresponding to the share of each particle size class of the total particle count. [71]

4.2.1 Environment modelling

Due to the high computational demand of modelling many millions of particles present in even small powder samples, DEM models are often miniatures or small samples of the real system. Significantly miniaturised L-PBF simulations have been found to generally agree well with reality, but the possible effects of miniaturisation should still be evaluated before making this assumption. [84]

L-PBF and other industrial applications of DEM simulation often feature containers and other objects that interact with the simulated powder. Atmospheric conditions and possible fluid flows may also be relevant for particle behaviour. For this reason, DEM programs used in industrial applications often feature tools for creating and importing complex moving or stationary geometries, and some programs couple the DEM model with a CFD (computed fluid dynamics) model to simulate the effect of fluid flows and atmosphere on the particles. [72]

4.3 Calibration

Parametrising DEM simulations requires a wide range of material properties, which can be very difficult to characterise. A commonly used approach in L-PBF simulations is to find some particle parameters through calibration by bulk behaviour, such as free flow or piling of powder. [21, 64] In calibration by bulk behaviour, one or multiple practical rheological experiments are repeated in the DEM simulation and particle parameters are adjusted until the bulk behaviour of the simulated powder matches that of the practical experiment. [64, 66]. Commonly calibrated parameters include rolling resistances [77, 84, 99, 100], surface energy/interparticle attractive forces [84, 77], and particle-level friction coefficients [80, 100, 101]. For simulations featuring non-spherical particles, the particle shape itself may be a calibrated parameter [64].

Of course, there is no certainty that the values of material properties found by calibration are actually true; only that their particular combination yields a simulation result that is close to reality in the particular calibration experiment [21, 64, 102]. Therefore, all calibration experiments should feature similar forces and mechanics to the simulated main process. For example, highly dynamic flow-based calibration experiments will not yield representative parametrisation for a simulation investigating static compression. It is also advisable to perform multiple different calibration experiments in order to choose robust parameter values, instead of parameter values that match reality only in that specific experiment. [102]

A literature review was conducted on DEM simulations of powder packing in L-PBF to find viable calibration methods, often calibrated parameters and their values, and the relevance of calibration to the end result. The results of this review are presented in Table 6.

Table 6 Calibration methods and parameters in literature.

μ = friction, h_{lt} = true layer height, *AOR* = angle of repose, *DRA* = dynamic repose angle.

Author, year	Subject	Calibrated parameters	Method	Remarks	Ref.
Tian et al. 2020	Fusing	-	-	Powder bed recoating simulated but not focus of study – not validated/calibrated	[87]
Han et al. 2019	Spread	*SE*	*AOR*	Optimisation of recoated layer height	[84]
Meier et al. 2019	Flow	*SE*	*AOR*	Characterised adhesive forces via *AOR* simulations	[77]
Desai et al. 2019	Flow	μ	*AOR*	Simulation for developing virtual copy of rheometer, validated with real device	[16]
Dai et al. 2019	Flow	-	-	Effect of *SE* and μ on *AOR*, no comparison to practical experiment.	[81]
Phua et al. 2021	Spread	μ, *SE*	AOR, Hall flow	Study on particle behaviour with different recoater geometries.	[90]
Dai et al. 2021	Flow	μ, *SE*	AOR, Hall flow	Characterised powder properties.	[80]
Yim et al. 2022	Spread	μ, *SE*	*AOR, DRA*, Hall flow	Studied inter-particle forces in recoating. Also PREP/GA effect on *PD*, roughness.	[38]
Yao et al. 2021	Spread	-	-	Effect of layer height, recoater velocity on *PD*, uniformity of bed.	[85]
Wu et al. 2022	Spread	h_l	h_{lt} (staircase)	Calibrated by layer height with a built staircase. Study of various recoating parameters effects on interparticle forces.	[52]
Xiang et al. 2021	Spread	-	-	Effect of platform surface roughness on powder bed.	[86]
Shaheen et al. 2021	Spread	μ, *SE*	*AOR*	Recoater effect on bed. Validated with visual comparison of hand-recoated bed	[79]
Lampitella et al. 2021	Spread	μ, *SE*	*AOR,* slip	Effect of recoating speeds on *DRA, PD*	[56]
Marchais et al. 2021	Spread	-	-	Effect of recoating parameters on recoating and powder bed	[76]
Zhang et al. 2020	Spread	*SE*	*AOR*, Avalanche	Effect of roller parameters on packing density	[103]
Chen et al. 2017	Spread	μ, *SE*	*DRA*	Study on powder flow behaviour during recoating	[23]
Chen et al. 2019	Spread	-	-	Study on powder packing, flow during recoating.	[50]
Si et al. 2021	Spread	μ, *SE*	*AOR*	Effect of recoating parameters on powder bed quality	[104]
Lee et al. 2018	Spread	-	-	Study on packing behaviour in settling and recoating	[70]
Wang et al. 2020	Spread	μ, *SE*	*AOR, PD*	Effect of adhesion, PSD on particle behaviour in recoating	[83]

As can be seen from Table 6, the most common calibration methods are the angle of repose (*AOR*) and dynamic repose angle (*DRA*), both of which have been used to calibrate surface energy and particle-particle friction coefficients. Both methods are illustrated in Figure 13.

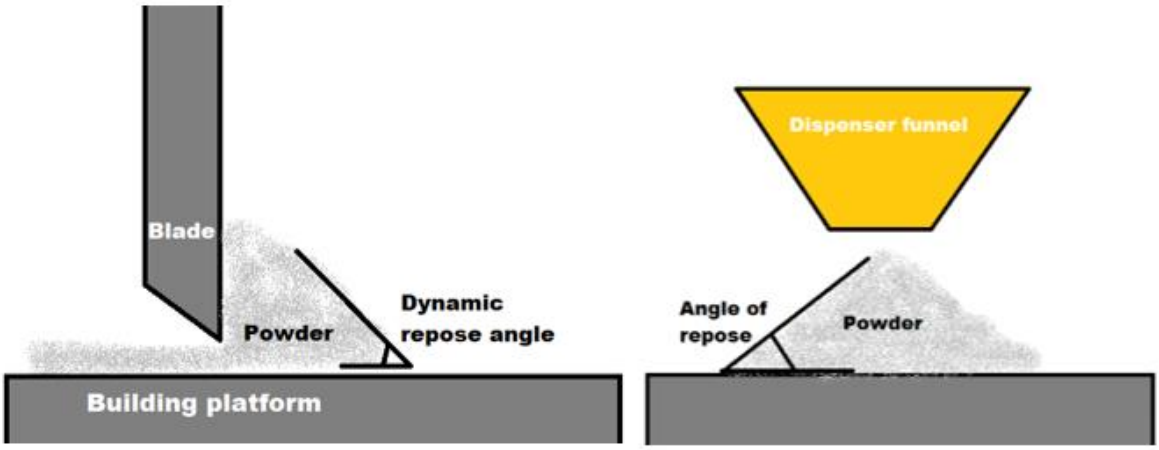

Figure 13 Sketch of *DRA* and *AOR* measurement [77, 84, 93].

As show in Figure 13, *AOR* is the angle of a pile of powder that has been freely poured onto a surface, while *DRA* is the angle of a pile of powder being pushed by the recoater. Multiple studies have found *AOR* to be sensitive to changes in both *SE* and interparticle friction coefficients, which makes it a useful calibration method [77, 84, 93]. *AOR* is also very easy to measure and is computationally less demanding. *DRA* and Hall flow experiments are more computationally demanding, but provide information on e.g., particle-wall friction which *AOR* does not. *DRA* can be a convenient calibration method if powder flow behaviour during recoating is modelled for the main simulation anyway, so the same simulation model can be repurposed or modified for calibration as well. It also features external shear forces from the recoater in addition to gravity, making it more representative of the dynamics of L-PBF processing compared to *AOR* or Hall flow. Other occasionally used methods were avalanche angle and slip angle testing, illustrated in Figure 14.

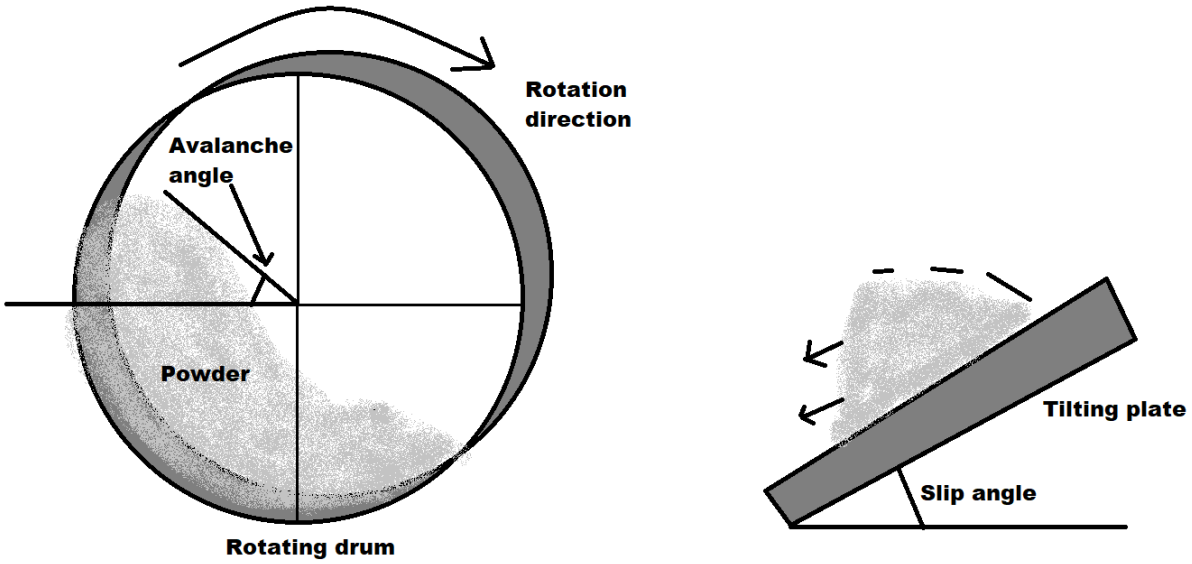

Figure 14 Measurement of avalanche angle and slip angle [56, 103]

As can be seen from Figure 14, avalanche and slip angle are executed in a controlled environment; avalanche angle is measured from powder bulk being spun inside a cylinder (similarly to a laundry machine) [103]. Slip angle is measured by pouring a pile of powder on a surface, and measuring the needed tilt angle for the pile to slide off [56]. The main distinction is that the powder is in constant movement in avalanche angle, while slip angle characterises friction from a static position.

A method used by Wu et al. (2022) [52] is the staircase calibration/validation tool. The staircase is built so that each recoated layer is fused into a "step" in the staircase, enabling the measurement of true layer height. Wu et al. (2022) utilised this to calibrate their DEM model based on layer height. This method is basically calibrating the experiment itself, rather than aiming to calibrate individual material properties.

It can be argued that calibrating the experiment itself until a good agreement between simulation and reality is found is no longer a method of parameter calibration, since it has been found that multiple parameter sets can result in similar powder behaviour, and there is no confidence that the used parameters represent the real material [80]. However, if ultimate truthfulness of a simulation model is deemed more important than the truthfulness of individual parameters, calibrating the entire simulation model instead of individual parameters can be considered a valid approach. This method requires a comprehensive and robust validation experiment as a benchmark that the simulation can be compared to.

4.4 Validation

In most cases, a simulation model is not useful if there is no way to know whether its results match with reality. The act of proving the realism of a simulation is called validation. To validate a simulation model, the model (or core components of it) is replicated in a practical experiment and the result of both the experiment and simulation model are measured and compared to each other. If the results match within a defined margin of error, the simulation model is deemed validated and can be trusted and applied to practical problems. Though in many cases a qualitative validation is accepted to reduce computation time and simplify the practical experiment, one or more quantitative validation experiments should ideally be done to have reasonable confidence in the model. Validation sounds similar to calibration, but one relevant difference is that in DEM, calibration experiments can only be used to define individual parameters, and calibration of individual parameters cannot confirm the truthfulness of the entire simulated model. [64]

A literature review was conducted on DEM simulations of powder packing in L-PBF to find viable validation methods, often validated parameters and their values, and the relevance of validation to the end result. The results of this review are presented in Table 7.

Table 7 Validation methods in literature.
PD = packing density, *DRA* = dynamic repose angle, *AOR* = angle of repose.

Author, year	Subject	Validated	Validation method	Remarks	Ref.
Tian et al. 2020	Fusing	Yes	Visual comparison of melt track	Powder bed recoating simulated but not focus – not validated	[87]
Han et al. 2019	Spread	Partly	Visual comparison of powder beds	Optimisation of recoated layer height	[84]
Meier et al. 2019	Flow	Yes	*AOR*	Characterised adhesive forces via *AOR* simulations	[77]
Desai et al. 2019	Flow	Yes	Rheometer	Developing a virtual rheometer, validated with real device	[16]
Dai et al. 2019	Flow	No	-	Effect of *SE* and μ on *AOR*, no comparison to practical experiment.	[81]
Phua et al. 2021	Spread	No	-	Study on particle behaviour with different recoater geometries.	[90]
Dai et al. 2021	Flow	No	-	Characterised powder properties.	[80]
Yim et al. 2022	Spread	Yes	Surface roughness	Studied stress conditions, inter-particle forces in recoating. Also PREP/GA effect on *PD*, roughness.	[38]

(Continued) Table 7 Validation methods in literature.

Yao et al. 2021	Spread	No	-	Effect of layer height, recoater velocity on *PD*, uniformity of bed.	[85]
Wu et al. 2022	Spread	Yes	*PD* + *DRA*	Study of various recoating parameters effects on interparticle forces. Staircase validation.	[52]
Xiang et al. 2021	Spread	Partly	*DRA*	Study on effect of platform surface roughness on recoating	[86]
Shaheen et al. 2021	Spread	Partly	Visual comparison of powder beds	Effect of recoaters on *PD* and uniformity. Validated with visual comparison to hand-recoated bed.	[79]
Lampitella et al. 2021	Spread	No	-	Effect of recoating speed on *DRA, PD*	[56]
Marchais et al. 2021	Spread	No	-	Effect of recoating parameters on recoating and powder bed	[76]
Zhang et al. 2020	Spread	No	-	Effect of roller parameters on packing density	[103]
Chen et al. 2017	Spread	Yes	*DRA*	Study on powder flow behaviour during recoating	[23]
Chen et al. 2019	Spread	Yes	*PD*	Study on powder packing, flow during recoating.	[50]
Si et al. 2021	Spread	Partly	*DRA*	Effect of recoating parameters on powder bed quality	[104]
Cao 2019	Spread	Partly	*AOR*	Study on packing behaviour in settling and recoating	[105]
Zhao et al. 2016	Spread	No	-	Effect of recoating speeds on *DRA, PD*	[106]
Liu et al. 2020	Spread	No	-	Effect of recoating parameters on recoating and powder bed	[107]
Gao et al. 2020	Spread	Partly	Visual comparison of melt track	Effect of roller parameters on packing density	[108]
Lee et al. 2018	Spread	Yes	*PD*	Powder flow in recoating. Validated with results of 3rd party study.	[70]

As can be seen in Table 7, the most common validation methods are visual comparisons between practical experiments and simulated models, tied with the *DRA.* Visual comparisons of powder beds are highly qualitative and even subjective, while a much higher accuracy between comparisons can be achieved by comparing the size and shape of melt track cross sections. However, the problem with validation by melt track is that it does not necessarily validate the powder bed simulation. Of course, the laser-material interaction could well be considered validated, but if the aim is to investigate the effect of changes in powder bed

parameters on the laser-material interaction, there is a question of whether only validating the melt track is sufficient.

As with calibration, *DRA* is a popular validation method. It is significantly more relevant to L-PBF simulations than *AOR*, but not necessarily sufficient to validate simulations focused on packing behaviour. However, some L-PBF simulation models do not investigate packing or any phenomenon dependant on it (such as laser beam absorptivity) as is the case with Chen et al. (2017) who studied the behaviour of powder bulk during recoating and the forces affecting individual particles, and for them *DRA* may be a reasonable choice.

AOR, used by two authors in this review, may not always be reliable for validating a spreading-related model, since the *AOR* experiment features no external forces besides gravity. However in a purely flow-based model which only features gravity and particle-particle interaction, it may well be a credible validation method, as is the case with Meier et al. (2019) [77].

A relatively popular validation method is the powder packing density. In some cases, *PD* was determined in conjunction with the staircase layer height calibration experiment. *PD* is relatively easy to measure from a simulation, though attention should be paid to how the sampling volume is defined (i.e. is the sampling volume embedded in the powder bed or following the extents of particles), as it will affect the resulting *PD* value and different methods are not comparable to each other [21]. *PD* can be measured directly from the powder bed and is mostly only dependent on powder properties and recoating process parameters, making it a credible parameter for validation of a known recoating process with a known powder feedstock.

A unique and interesting entry in this table is the rheometer-based validation experiment, which was done by Desai et al. (2019) [16]. In this experiment, the rheometer itself was replicated in DEM and its outputs (torque and normal force on the tool shaft) during rheometer test programs were compared to those of the actual device, in order to validate the simulated powder material.

A surprisingly rare validation approach is surface roughness, which was only utilised by Yim et al. (2022) [38]. One reason for the rarity might be the relative complexity of characterising topography of the simulated powder bed so that it can be directly compared to real beds.

Another result of this literature review is what is missing in Table 7; nine out of the 23 papers reviewed used no validation at all, and of those that did, six used a validation method that does not match the conditions and mechanics of the validated experiment.

5 Aim and purpose of experiments

The goal of the experimental part is to create a simulation which EOS Finland can use to study the behaviour of powder particles in powder beds and the effect of changing material properties on the L-PBF process. The scope of the experimental work of this thesis was limited to powder bed forming and recoating, as the introduction of laser-material interaction will significantly increase the complexity of the model and the amount of needed background information and experimentation.

As visualised in column A of Figure 15, EOS Finland is developing Tungsten powder materials. Tungsten is a challenging material for all aspects of L-PBF processing, and thus requires disproportionate amounts of experimentation to develop as an L-PBF feedstock. For this reason, EOS Finland is looking into simulation as a solution to reduce the amount of iterative experimentation, which is the motivator of this thesis.

Column B of Figure 15 shows the scope of this thesis. As can be seen, the main research goal is to develop a realistic simulation model of powder behaviour in a powder bed. Realistic modelling is required in order to replace practical experimentation with simulated experiments, which is why the simulation model must be accompanied by a validation method. Established validation processes or standards for L-PBF simulations were not found, so developing and executing a practical, accurate validation method is an important subgoal, arguably as important as the simulation model itself. The validation experiment is repeated multiple times and sources of uncertainty are recognised and quantified to provide a solid base for development in the future.

The initial simulation and validation method will be developed using a mature, well-known L-PBF powder material EOS NickelAlloy IN718 in order to reduce uncertainties unrelated to the simulation model. If the model is successfully validated, the particles will be re-parametrised to represent Tungsten. The Tungsten simulation will not be included in this thesis but created for EOS Finland as a jumping off point for future Tungsten simulation development, as shown in column C of Figure 15.

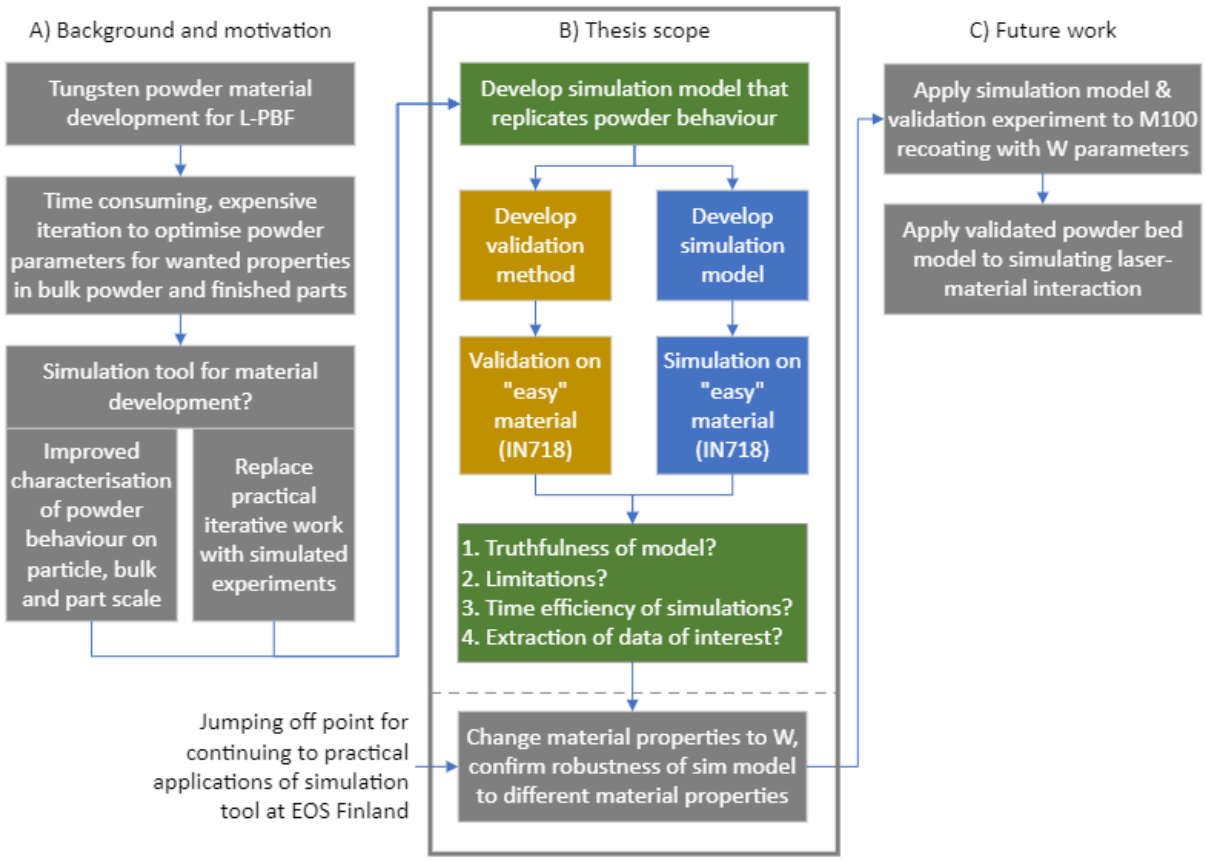

Figure 15 Visualisation of thesis background, scope, and future application of thesis results.

Since the simulation and validation process will be expanded to laser-material interaction and challenging Tungsten powder, both experiments must be designed with customisability in mind. The simulation model should be reproducible, reliable, and robust to changes in environment, process parameters, and material properties. It should also support the introduction of other physics models such as the laser heat source, material phase change, and different thermodynamic fluid flow mechanics. Similarly, the validation experiment must be reliable, adaptable, and reproducible.

The simulation model would be developed using software and computers provided by University of Turku, while design and execution of validation experiments would be done at EOS Finland using their software, computers, L-PBF systems, tools, and powder materials.

The thesis features two similar experiments which take place in different domains, physical (validation) and virtual (simulation). To avoid confusion between domains, the experimental portion of the thesis is presented with a division into Part A: Validation and part B: Simulation.

6 Experimental set-up

6.1 Powder material

6.1.1 EOS NickelAlloy IN718

The powder material used in validation experiments as well as a basis for the simulated particles is the gas-atomised EOS NickelAlloy IN718 powder. IN718 was chosen for multiple reasons. Its behaviour in L-PBF processing is well understood, which reduces the need for iteration and experimentation when designing validation samples, i.e., validation samples can be expected to build successfully and consistently without further parameter optimisation. Gas-atomised IN718 powder particles are also mostly spherical in shape, which is significantly easier to model in DEM. Finally, IN718 is a highly interesting and commonly used AM material especially in the energy industry [4, 5] which makes IN718 a relevant research subject for advancing the development of materials for energy technology.

IN718 is a nickel-based superalloy, which has high strength and resistance to creep and corrosion even in high-temperature environments. It features predictable grain structure and chemistry, is weldable and heat treatable, and importantly is well suited to L-PBF processing. These factors have lead to its wide use in various combustion environments, such as rocket engines, turbines, incinerators, and exhaust components, but also in cryogenic applications – all of which have many use cases for complex high value parts produced by L-PBF. [4, 5]

Parts produced with EOS NickelAlloy IN718 can be expected to have an ultimate tensile strength of 1020 MPa, yield strength of 710 MPa, and 29% elongation at break. Chemical composition of the powder material is listed in Table 8 below. [109]

Table 8 Chemical composition of EOS NickelAlloy IN718.

Element	Fe	Ni	Cr	Nb	Mo	Ti	Al
Min wt%	Balance	50	17	4.75	2.8	0.65	0.2
Max wt%		55	21	5.5	3.3	1.15	0.8

Element	Co	Cu	Si	Mn	Ta	C	S	P	B	Pb	Se	Bi
Min wt%	-	-	-	-	-	-	-	-	-	-	-	-
Max wt%	1	0.3	0.35	0.35	0.05	0.08	0.015	0.015	0.006	0.0005	0.002	0.00003

As seen in Table 8, IN718 is a Nickel-Chromium-Iron alloy, with other constituents being Niobium, Molybdenum, Titanium and Aluminium, all of which have both minimum and maximum contents. 12 other minor constituents or impurities are also specified a maximum content.

The powder lot used for experiments in this thesis had been previously characterised by the EOS Finland laboratory. The relevant characterisation results and methods are presented in Table 9. The powder was not in virgin condition as used in experiments, but once used before in a separate build job and sieved with a 63 µm aperture sieve to separate melted and re-solidified particles, large particles, and agglomerates. Theoretically, after reuse and sieving, the PSD can be expected to change and the particles may become less spherical. However, based on findings by Rock et al. (2021), Cordova et al. (2019) and Hann (2016) the changes in PSD, chemical composition, and morphology of IN718 powder can be expected to be negligible after only one reuse [110, 111, 112]. Therefore, in this thesis the powder properties are assumed to remain unchanged from the virgin state, in which the powder was characterised.

Table 9 IN718 powder properties.

Property		Value	Characterisation method
Skeletal density	[g/cm^3]	8.2	ASTM B923-22 [40] Pycnometry
d10 | d50 | d90	[µm]	16 | 31 | 48	ISO 13322-2 [113] Dynamic image analysis
Sphericity, mean	[-]	89.3%	ISO 13322-2 [113] Dynamic image analysis
Apparent density	[g/cm^3] | [%]	3.85 | 46	ASTM B417 [114] Hall funnel & cup
Internal friction angle	[°]	24.6	ASTM D7891 [115] FT4 Rheometer
Wall friction angle	[°]	17.8	ASTM D7891 [115] FT4 Rheometer
Flow function	[-]	10.9	FT4 Rheometer
Basic flow energy	[mJ]	686.6	FT4 Rheometer
Specific energy	[mJ/g]	2.9	FT4 Rheometer

As seen in Table 9, EOS IN718 is a typical gas atomised, predominantly spherical powder, with a d10-d90 width of 16-48 µm and d50 of 31 µm. The flow function as defined by Jenike (1964) [116] is 10.9. With the Jenike method, >10 is considered as free-flowing powder. Additionally, friction angles are relatively low, indicating low frictional forces between particles, though elevated specific flow energy indicates some particle-particle interlocking during flow which can be expected from gas-atomised powder. As seen in Figure 16, the PSD is positively skewed.

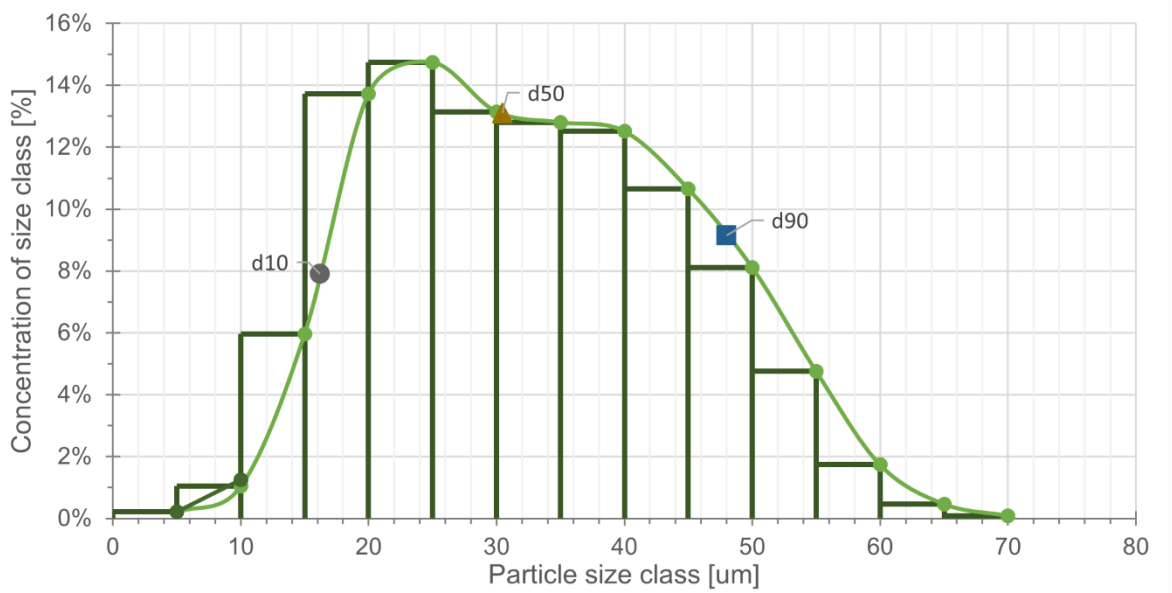

Figure 16 Distribution of IN718 size classes. A histogram and interpolated curve with d10, d50, d90.

Figure 16 shows the PSD as a size class histogram. Each column represents a measured particle class. The width of the column on the x-axis indicates range of particle sizes in the size class, while the height of the column on the y-axis indicates the portion of each size class in the entire powder sample. A curve is interpolated between the endpoints of each size class. D*10, d50,* and *d90* are marked on the curve.

As shown in Table 9, apparent density is 46%, which is relatively typical of AM powder feedstocks. A skeletal density of 8.2 g/cm^3 indicates little to no internal porosity, as it matches a measured solid density for IN718 alloy [117]. Sphericity of 89.3% indicates mostly spherical particles with some defects, which can be seen in SEM micrographs shown in Figure 17.

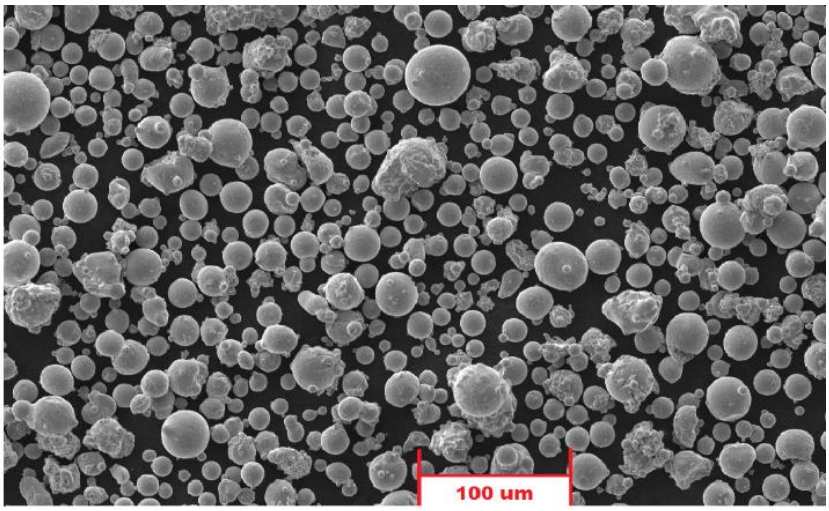

Figure 17 An SEM micrograph of the used IN718 powder. 500X magnification.

Figure 17 shows the morphology of IN718. Typical of GA powder, it is mostly spherical with occasional irregular or conjoined particles, satellites, and agglomerates. The large agglomerates are expected to have been removed in sieving before the powder was used in L-PBF.

6.2 Simulation software

FLOW-3D by Flow Science Inc. (United States of America) is a CFD software platform specialising in solving free-surface models. It can be augmented with modules aimed directly to certain industries, such as additive manufacturing, casting, and civil engineering. The base software alone can be used to simulate a variety of multiphysics fluid flows, but the modules provide specialised physics models necessary for the applications of each industry. [118]

The simulations for this thesis were made using the base FLOW-3D software and the DEM-module, which is a part of the AM package. The DEM module gives the particle physics a viscoelastic (modelled as a Voigt linear spring-dashpot model) collision mechanic, which enables realistic Newtonian interparticle behaviour. The DEM module also gives the user options for defining dynamic and static friction coefficients and adhesive forces. The particle properties are defined within the DEM module as shown in Figure 18.

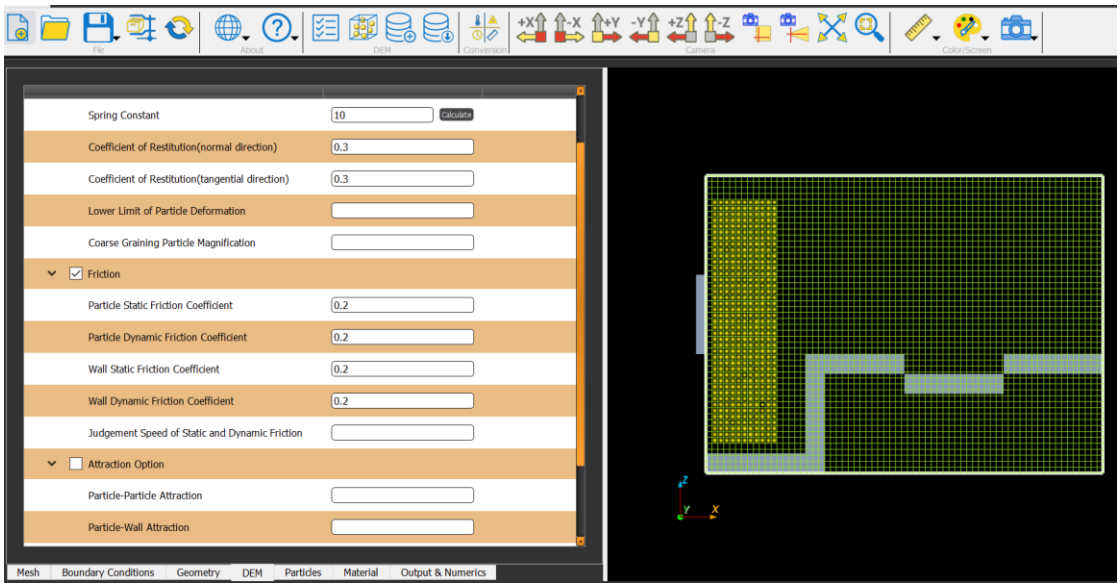

Figure 18 DEM module user interface with a simplistic example simulation.

As seen in Figure 18, the main function of the DEM module is to input particle properties to specify the linear spring-dashpot contact physics model for the particles, but most modelling functions are also available. The DEM module leaves out most multiphysics options and other functions that are irrelevant for a particle-based simulation model. The simulated environment can be modelled in the DEM module or in the base software, shown in Figure 19.

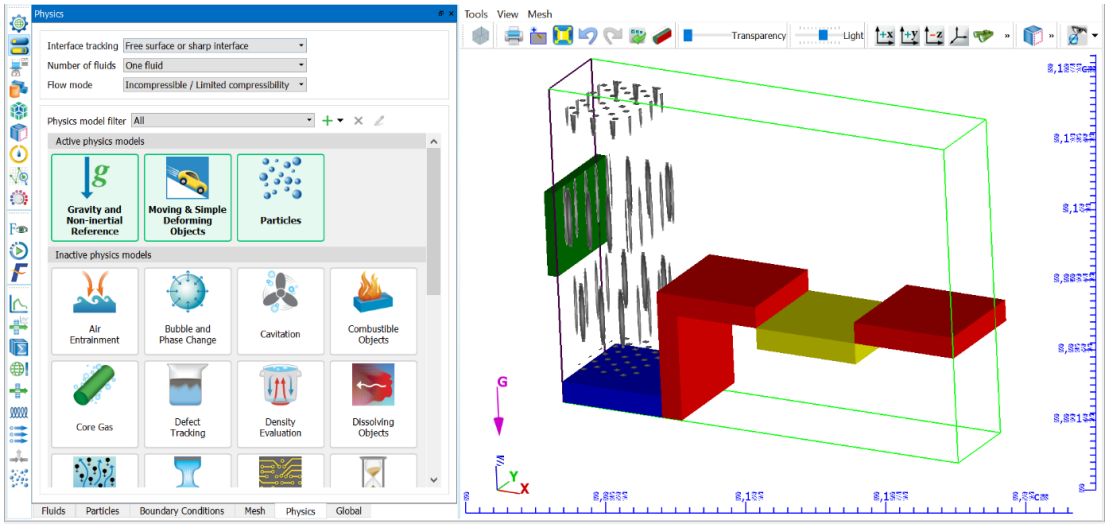

Figure 19 Base FLOW-3D software user interface with a simplistic example simulation.

As seen in Figure 19, the base FLOW-3D software provides a wide selection of physics models and analysis tools that can be incorporated into a simulation. The physics selection widget is opened in the image, with physics chosen for gravity, moving objects, and discrete particles.

On the right-hand side is a simplistic example of a powder bed -forming simulation, with a powder dispenser (blue), blade (green) and building platform (yellow).

6.3 Design and manufacturing software

6.3.1 SolidWorks 2017

SolidWorks by Dassault Systémes S.A. (France) is a parametric, feature-based 3D CAD (computer-aided design) program, used worldwide by many industries for various design and engineering applications. [119] The 2017 version of SolidWorks was used in the experimental portion of this thesis for modelling samples and finding their nominal dimensions and volumes.

6.3.2 EOSPRINT 2

EOSPRINT by EOS GmbH (Germany) is a CAM (computer-aided manufacturing) software for converting 3D models into numerical control instructions encompassing all the necessary information such as laser scanning paths, laser power, platform movement etc. for EOS L-PBF systems. [120] EOSPRINT 2 was used in the experimental portion of this thesis for build job preparation such as part positioning, and generating the necessary CAM data and transferring it to the used EOS L-PBF system. A screen capture of the build job preparation process for the open cup sample as used in the validation experiments can be seen in Figure 20.

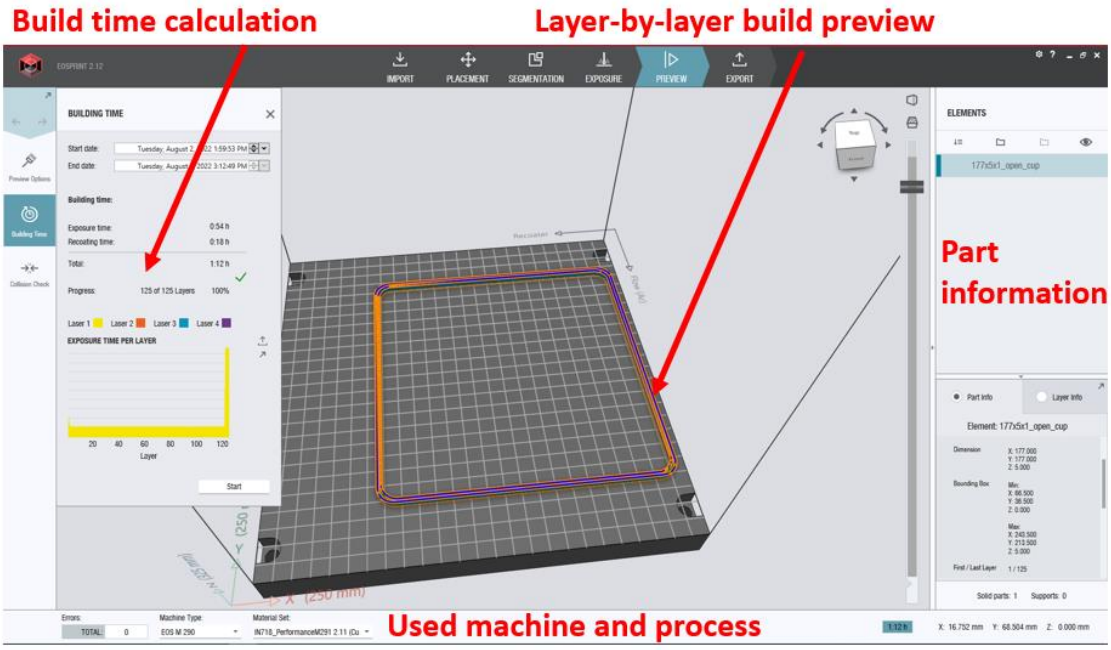

Figure 20 User interface of EOSPRINT 2. The part is in build preview mode, showing the contours, infill, and boundaries in colour-coded view one slice at a time.

Shown in Figure 20 is the preview-tab of EOSPRINT2, where the user can view the process one layer at a time. Individual scan vectors are shown and colour-coded depending on their type. The building time calculation can also be seen in the top left-hand corner.

6.4 Hardware

6.4.1 L-PBF system

The L-PBF system used in this thesis is the M 290 by EOS GmbH (Germany). It is a medium sized system launched in 2014, featuring a 250 x 250 x 325 mm building volume and one or two 400 or 1000 W Ytterbium fibre lasers, with further options for different optics and a selection of various hard and soft recoater blades. [121] An M 290 configured with one 400 W laser and a steel blade was used for building the validation experiment samples in this thesis.

The M 290 has a three-lifter, single direction recoater configuration, with a building platform lifter in the centre, a collector lifter on the left (as viewed from the chamber window) and a powder dispenser lifter on the right. Powder is dispensed by lifting it incrementally in inverse relation to the movement of the building platform, and swept from the dispenser, over the building platform, and into the collector by a recoater blade, as shown in Figure 59. The building platform then lowers out of the way so the recoater can move back to its original position behind the dispenser. Inert gas flow is perpendicular to the recoater movement, towards the chamber window, as shown in Figure 21.

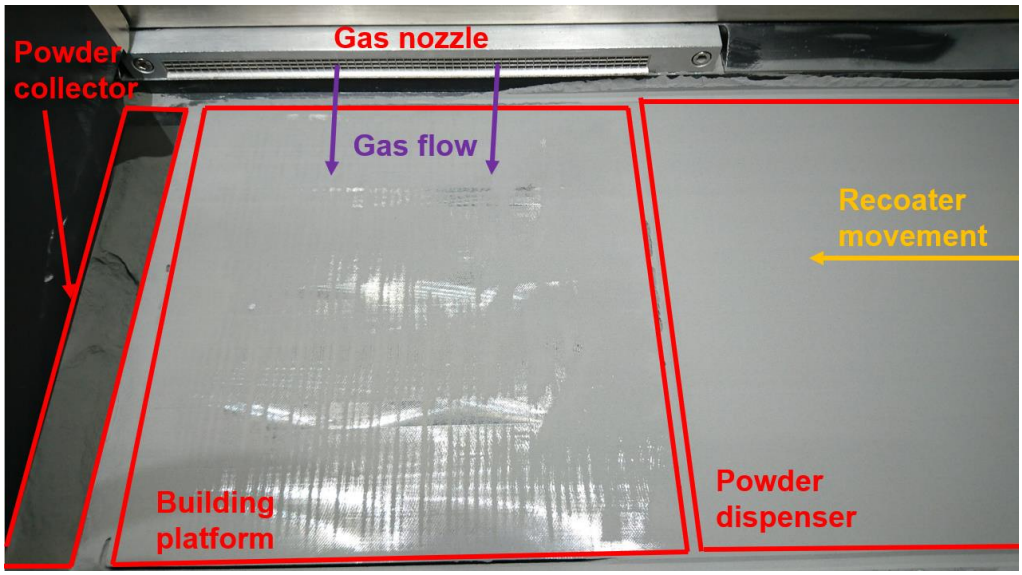

Figure 21 Picture of the M 290 process chamber, taken from the chamber door.

6.4.2 Measuring instruments

Calliper

Mitutoyo 500-173-30 Absolute Digimatic (Japan) seen in Figure 22 is a large digital precision calliper with a thumbwheel and electrostatic capacitance-based sensing. Measuring range is 300 mm and step size 0.01 mm.

Figure 22 Mitutoyo digital calliper as used in experiments.

The small inside jaws as indicated in Figure 22 were used for measuring the length and width of the validation samples.

Depth gage

Mitutoyo ID-C112X/1012X Absolute Digimatic (Japan) shown in Figure 23 is a digital precision depth gage with electrostatic capacitance-based sensing. Measuring range is 12.7 mm and step size 0.001 mm.

Figure 23 Mitutoyo digital depth gage as used in experiments.

As indicated in

Figure 23, a flat-bottom stand was used for measuring the wall height of the validation samples.

Scale

Mettler Toledo ICS425 (Switzerland) seen in Figure 24 is a general industrial scale. Measuring range is 5 – 35100 g and step size 0.1 g.

Figure 24 Mettler Toledo scale as used in experiments.

The scale was used for weighing validation samples in the condition shown in Figure 24.

Rheometer

The Freeman Technology FT4 rheometer (United Kingdom) seen in Figure 25 is a powder characterisation device capable of measuring a range of bulk powder properties with different measurement vessels and attachments. The device works by spinning a blade or other tool inside or on top of a powder sample. In this thesis, it was used to measure the basic flowability energy, specific flow energy, internal friction angle, and wall friction angles of IN718 powder as well as two benchmark powder feedstocks (spherical and non-spherical). Attachments used were the 23.5mm blade, compression head, shear head, and wall friction head.

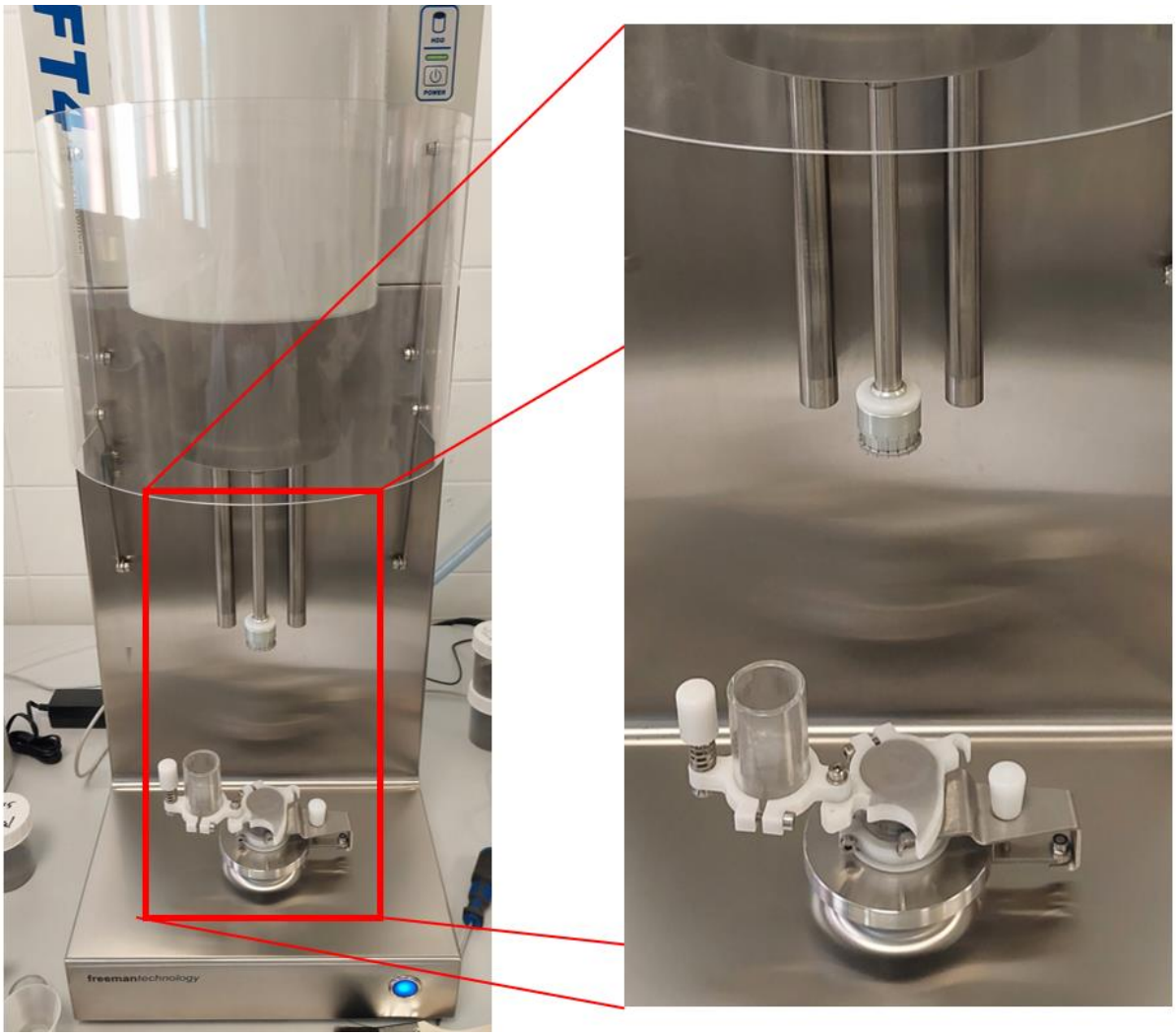

Figure 25 FT4 rheometer with shear head attachment and readied powder sample.

7 Experimental procedure (part A: Validation)

7.1 Validation samples

The simulation should be validated with a quantitative experiment that replicates the simulation model. Ideally, multiple different parameters would be used in order to have higher confidence in the validation, but in this thesis only one parameter would be used for validating the simulation due to time constraints and simplicity for possible future commercial use. As seen in Table 7, using only one parameter for validation of powder bed simulations is common.

A set of requirements were defined before researching validation approaches. For instance, the validation experiment should match the simulated environment as closely as possible. The simulation is restricted to <10 recoated layers and a small sampling due to the significant computation time of simulating larger numbers of particles. Therefore, the validation experiment should also sample a very shallow powder bed at the edge of the building platform. However, the sampled area in the validation experiment should be relatively large to reduce the impact of possible human error or other inherent process variability, increasing the robustness and repeatability of the experiment.

7.1.1 Validated parameter and validation sample

The literature reviews on powder bed parameters, their characterisation, and validation methods of powder bed simulations were conducted to find parameters and methods for validation. The most interesting parameter for validation was powder packing density.

However, most *PD*-based validation methods or other methods for characterising *PD* found in the review were not applicable for large sample sizes, could not be applied to commercial L-PBF systems, or were not suitable for sampling shallow powder beds, all of which are requirements for the validation method. A common approach in literature was to build a container of some sort with the L-PBF process and measure the mass and volume of the powder trapped inside the built container. Specifically, the closed container method used by Jacob et al. (2016) [53] and Farzadfar et al. (2020) [8], as well as the open cup methods used by multiple authors showed the most promise in terms of feasibility and ability to conform to validation requirements.

The open cup method for determining PD as the validated powder bed parameter was ultimately chosen, though multiple test runs for closed container samples were also done – the iterative

design and testing process for all samples is described in detail in Appendix 5. The final open cup sample design shown in Figure 26 was found by first identifying limiting factors and possible sources of error, and then narrowing down the possible shapes, sizes, and platform locations of the sample.

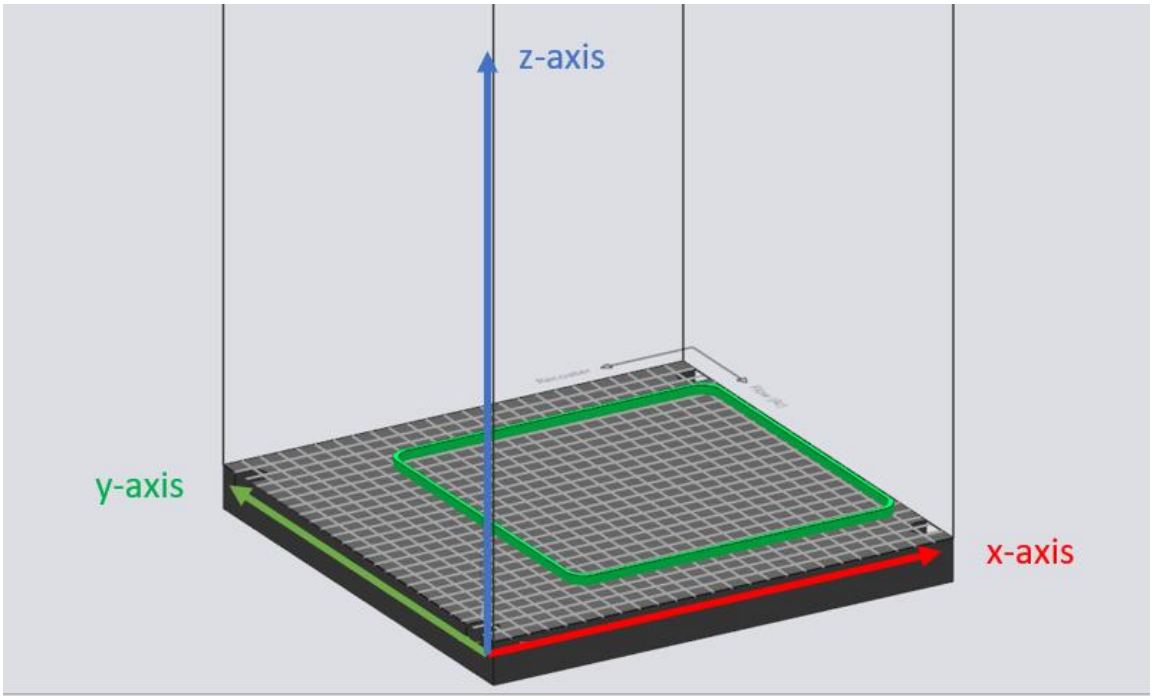

Figure 26 3D model of the final open cup sample design; Built part in green, and the building platform in black with a grid surface. Y-x-z -axes are marked with green, red, and blue.

Figure 26 shows a 3D model of the as-built sample, the built part in green and the building platform in grey. It is essentially a continuous wall which traps a shallow powder bed sample inside. Powder is not displayed in the 3D model.

Minimising and quantifying sources of error was prioritised when the sample and experiment were planned. The greatest source of error was expected to be the process of cleaning the sample before removal from the process chamber, transportation of the sample to a powder handling space, and the handling of the sample during weighing and powder removal. Similarity to the simulated environment was also considered important. With these priorities and concerns in mind, the sample was defined as follows:

- The shape of the sample was decided to follow the rectangular shape of the sampling area in the simulation. The sample would be a square, with corners rounded at a 10 mm radius, to make it easier to remove powder from the wall corners using a paint brush.

- The wall height should be as low as possible to emulate the very shallow simulation powder bed, but sufficiently high so that the residual powder can be brushed away without disturbing the sampled powder. 5 mm was estimated to be a good compromise.
- The area of the sample should theoretically be as large as possible to minimise the amount of powder removal and clean-up. A large area also means a larger mass of sampled powder, which reduces the relative significance of any error. However, the very edges of the powder bed should not be included. The final outer dimensions were 178x178 mm.
    - *PD* has been found to decrease towards the end of recoater travel in the x-axis due to separation of different sized particles [38, 60]. Therefore, only the first 2/3 or so of recoater travel where *PD* is stable, would be sampled.
    - Internal studies at EOS have also showed reduced *PD* at the y-axis edges of the powder bed, and for this reason the sampling area was centered and edges left unsampled.
- Wall thickness was chosen to be 2.5 mm, which is relatively high, but makes it easier to brush away powder outside the walls without disturbing the powder within the walls. The brush bristles can be expected to get bent or be otherwise pointing in different directions, so 2.5 mm of "buffer zone" between the brushed area and the sampled area was thought to be a good idea.

7.2 Validation experiment

Sources of uncertainty were identified while planning the validation experiment, and the methodology was planned so that the effect of these uncertainties could be quantified from the results. The sampled powder would be weighed at three different steps to catch any variation in results which could indicate loss of powder or inclusion of residues. In addition the measured volume would be compared to nominal values to estimate the dimensional accuracy of the samples and process-related variance in *PD* measurements.

The validation experiment samples were built using a default 40 µm layer height EOS IN718 process with automatic dosing control. The building platform was levelled using a feeler gage between the recoater blade and platform, and the platform-recoater gap was ensured to be less

than 40 µm in all points with a depth gage. After this, a single layer was deposited by driving the recoater from end to end once as shown in Figure 27.

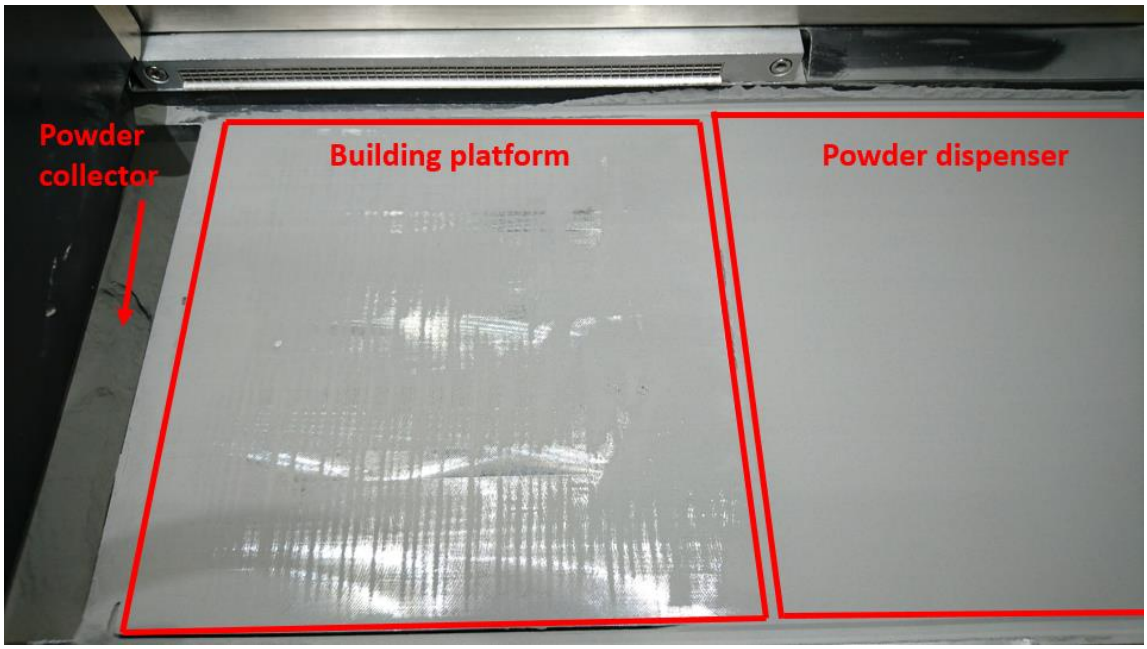

Figure 27 View into the building chamber after depositing a first layer of an open cup sample build job.

As seen in Figure 27, the platform was not always perfectly flat after removal of previous parts and machining. The first layer was purposely left too thin as opposed to covering the entire platform. Too thin a layer will not cause problems, but too high layer thickness (even locally) can cause lack of fusion and possibly cause the entire job to fail. The second layer would even out most of these µm-scale differences in platform surface elevation.

After depositing the first layer, the process conditions were established, and the job started. Job duration was approximately one hour, and the first 10 minutes of the job were supervised. A recoater crash into the sample occurred in the first exposed layer of the first sample (OL1), but this did not visibly deform the sample, so the job was continued as normal after the recoater was reset and the platform lowered by one layer height. This increases the height of OL1 by ~40 µm. After completion, the building platform was raised to its maximum Z-axis position as seen in Figure 28 and all powder outside the sample walls was carefully brushed into the collector bin with a 30 mm paint brush.

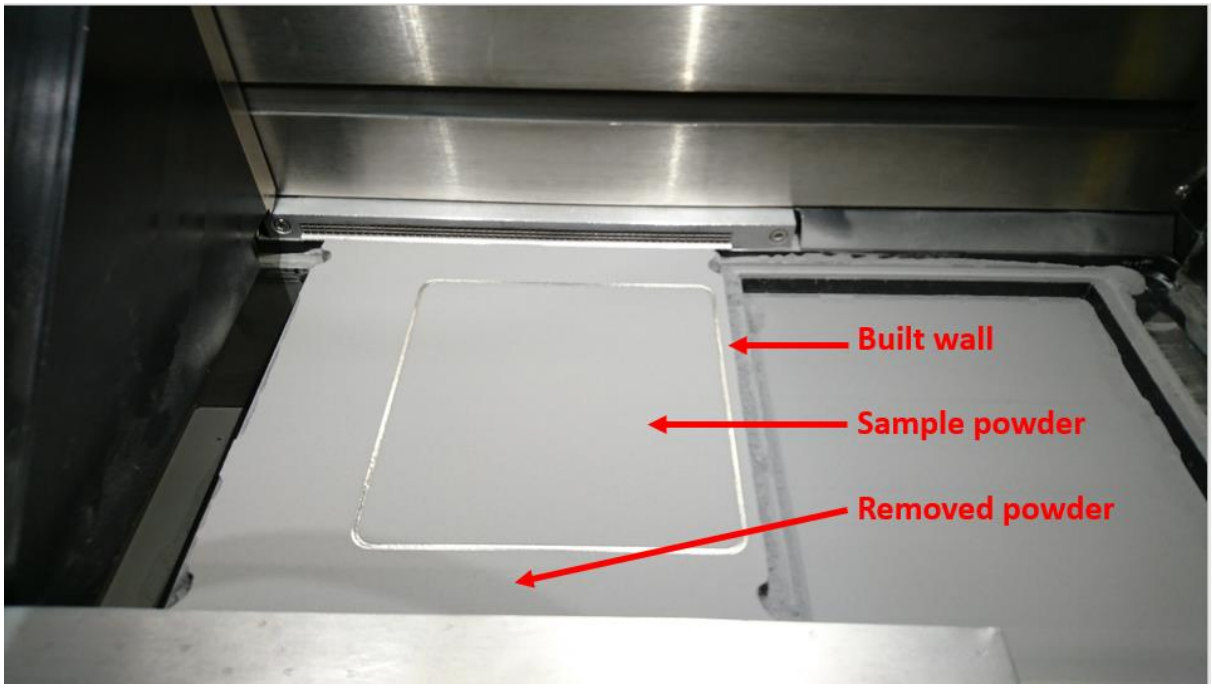

Figure 28 View into building chamber after a job is completed. The building platform is elevated for clean-up and removal.

As seen in Figure 28, most of the unused powder can be wiped directly into the powder collector bin on the left. The rest of the powder was carefully brushed into the collector bin.

A set of five identical samples, produced and measured back-to-back as quickly as possible, was decided to be the minimum to reach good statistical confidence in the results.

7.2.1 Sample measurements

Measurement process Phase 1: The sample was carefully lifted from the build chamber onto a wheeled cart. As seen in Figure 29, the sample was covered with a cardboard box to prevent unexpected airflows caused by e.g., opening doors from disturbing the sampled powder. The cart was slowly pushed to a powder handling space (a travelled distance of about 40 meters), paying attention not to dust the powder due to e.g., vibrations from the wheels. Inside the powder handling space, the cardboard box was removed and the sample carefully placed on a scale to record the weight of the full sample, m_{full}, as seen in Figure 30.

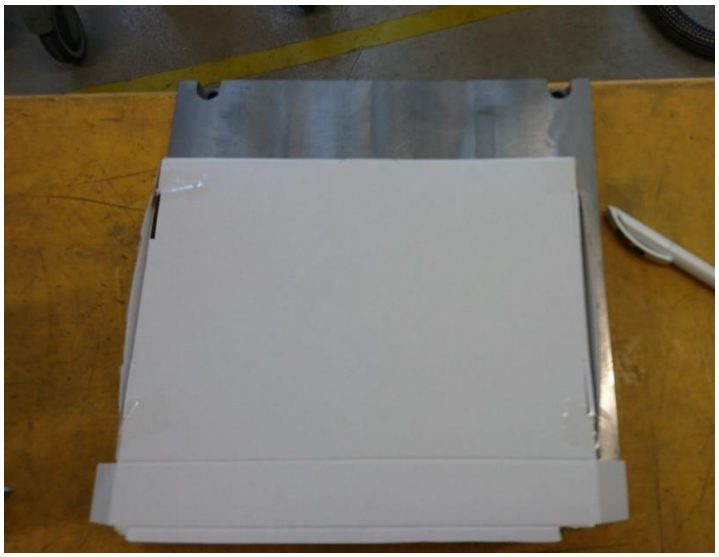

Figure 29 Full sample on a cart during transit in Phase 1, covered with a cardboard box.

Figure 30 Full sample on scale in Phase 1.

Figure 29 and Figure 30 show how the sample was always covered with a cardboard box, except during weighing. The box did not contact or otherwise disturb the sample.

Phase 2: The sample was placed back on the cart, after which the powder inside the walled sampling area was carefully moved into a pre-weighed plastic “Ziploc”-style bag with a 30mm paint brush and a scoop, which are shown in Figure 31. The bag was weighed as seen in Figure 32, and the known weight of the bag was subtracted from the reading. This gives us the minimum possible powder mass m_{powder_min}, since only powder from within the sample is weighed.

Figure 31 Equipment used for removing sampled powder.

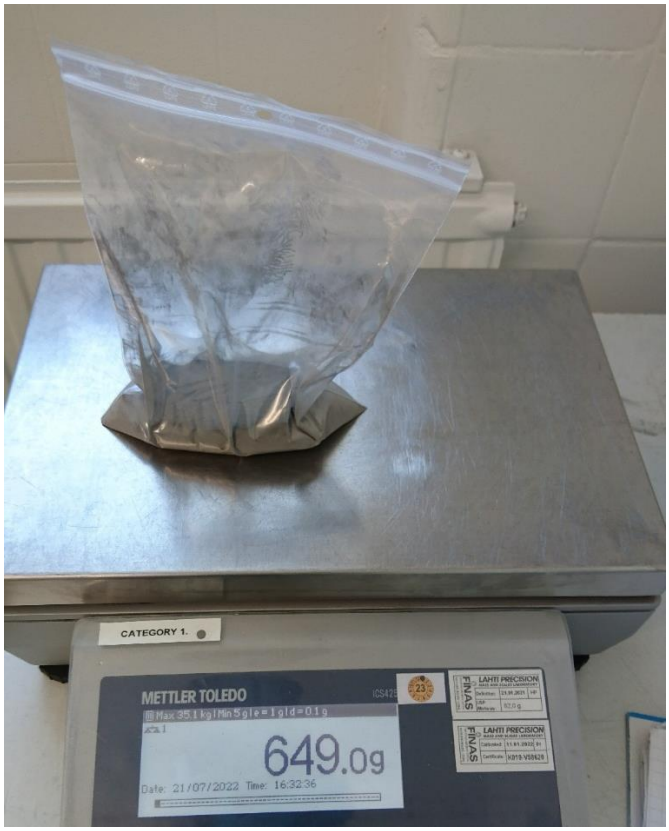

Figure 32 Weighing sampled powder in pre-weighed bag (m_{powder_min}).

As seen in Figure 31 and Figure 32, the powder was manually transferred into a sealable plastic bag, which was weighed to obtain m_{powder_min}. M_{powder_min} is assumed to be lower than the true powder mass, as some powder is likely always dusted off during brushing, missed altogether,

or dusted off while scooping as visualised in Figure 33. A thin layer of powder on the platform, likely dusted off during scooping, can be seen Figure 34 .

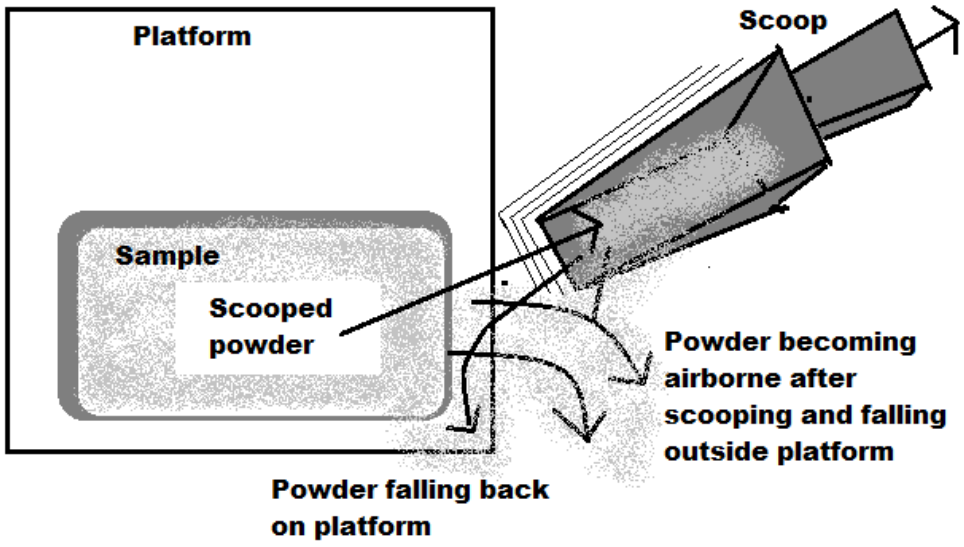

Figure 33 Presentation of the mechanisms of powder loss.

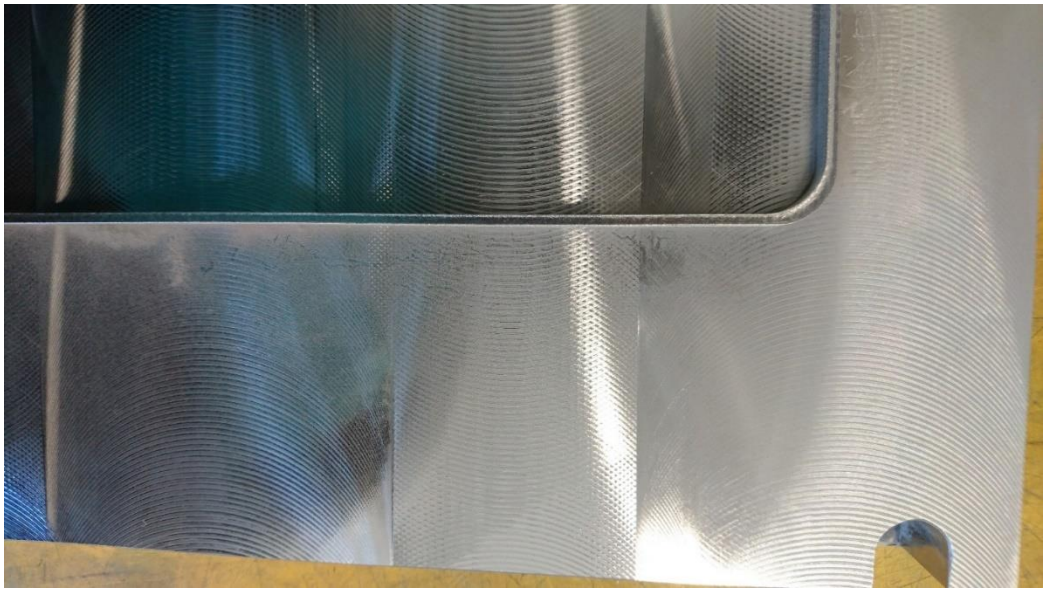

Figure 34 A thin layer of powder residue outside the built wall, likely dusted off from the scoop and onto the platform during emptying of the sample. The mass of this residue would be included in $m_{emptied}$, but not $m_{cleaned}$.

The mechanisms of powder loss during sample emptying are illustrated in Figure 33. Figure 34 presents likely evidence of the dusting phenomenon shown in Figure 33.

Phase 3: The emptied, but not cleaned, sample was again weighed, giving $m_{emptied}$. Equation 2 can be used to find the likely most accurate figure of powder mass $m_{powder\_measured}$.

Here m_{full} is the mass of the platform, sampled powder, and any powder residue, while $m_{emptied}$ is the mass of the platform and residues after the sampled powder is removed.

$$m_{powder\_measured} = m_{full} - m_{emptied} \quad (2)$$

Phase 4: The sample was then thoroughly vacuum-cleaned and wiped with a rag and isopropyl alcohol (IPA) spray (AT-Tuote Oy, Finland) on all sides, and weighed again after any residual IPA had evaporated. This mass is $m_{cleaned}$. The maximum possible powder mass m_{powder_max} can be found using Equation 3.

$$m_{powder\_max} = m_{full} - m_{cleaned} \quad (3)$$

Since some residual powder in e.g., screw holes, wall corners, scratches and other crevices outside the sampling area was likely removed in the cleaning and thus featured in the removed mass, m_{powder_max} is assumed to be slightly larger than the true powder mass. Figure 35 shows a small amount of powder residue in the corner between the outside edge of the built wall and platform, likely a combination of powder missed during initial cleaning in the process chamber and sampled powder dusted off during transit or sample scooping.

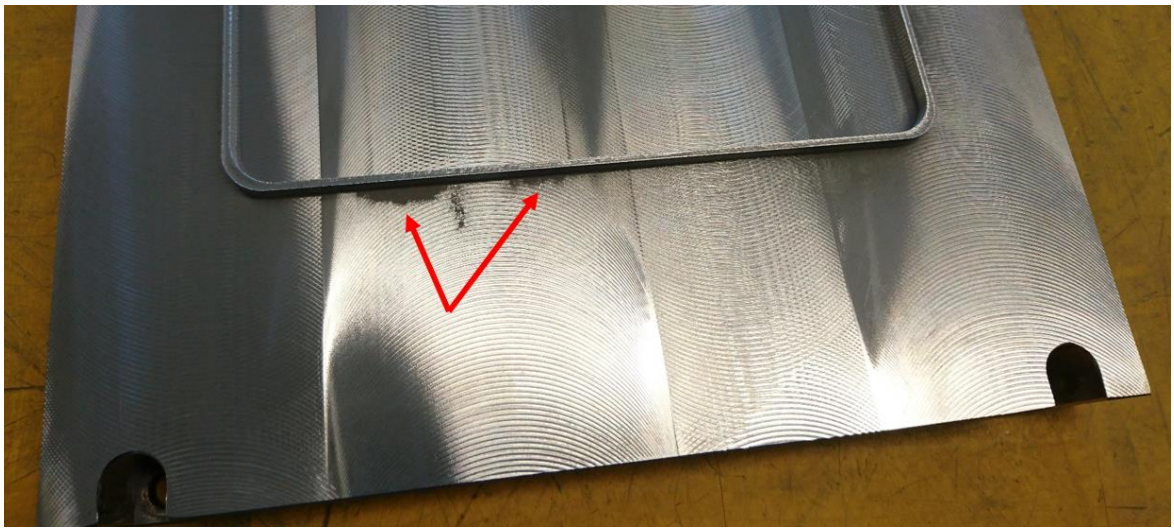

Figure 35 Residual powder outside sampling area, marked with arrows.

The powder residue marked with red arrows in Figure 35 would be included in $m_{emptied}$, but not $m_{cleaned}$. The m_{powder_max} and m_{powder_min} were determined in order to quantify the maximum range of error resulting from residual powder and the dusting of powder during handling.

Phase 5: The empty sample was allowed to settle into ambient temperature of 25 degrees Celsius overnight. Then, the sample dimensions were measures. The height of the built wall was measured with a Mitutoyo digital depth gage at each corner as shown in Figure 36.

Figure 36 Wall height measurement method with digital depth gage.

As shown in Figure 36, the flat bottom was placed in a 45˚ angle over the corner and a height measurement was taken at each corner, called h_1-h_4. Then, width and length measurements w_1-w_3 and l_1-l_3 of the sample were taken as shown in Figure 37 at locations indicated in Figure 38.

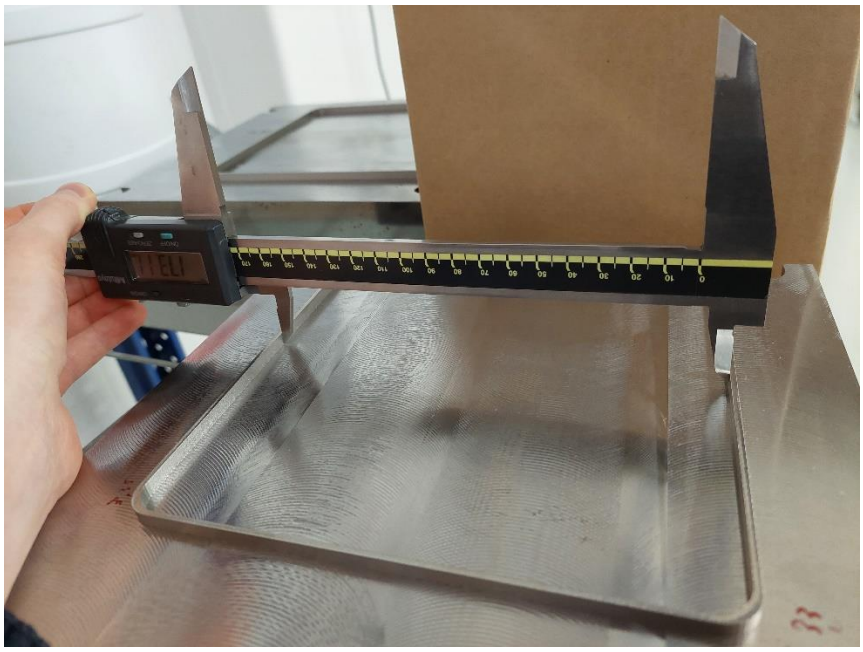

Figure 37 Length and width measurement method with the calliper.

Figure 37 shows how the calliper was used to take width/length measurements. The measured locations are shown in Figure 38.

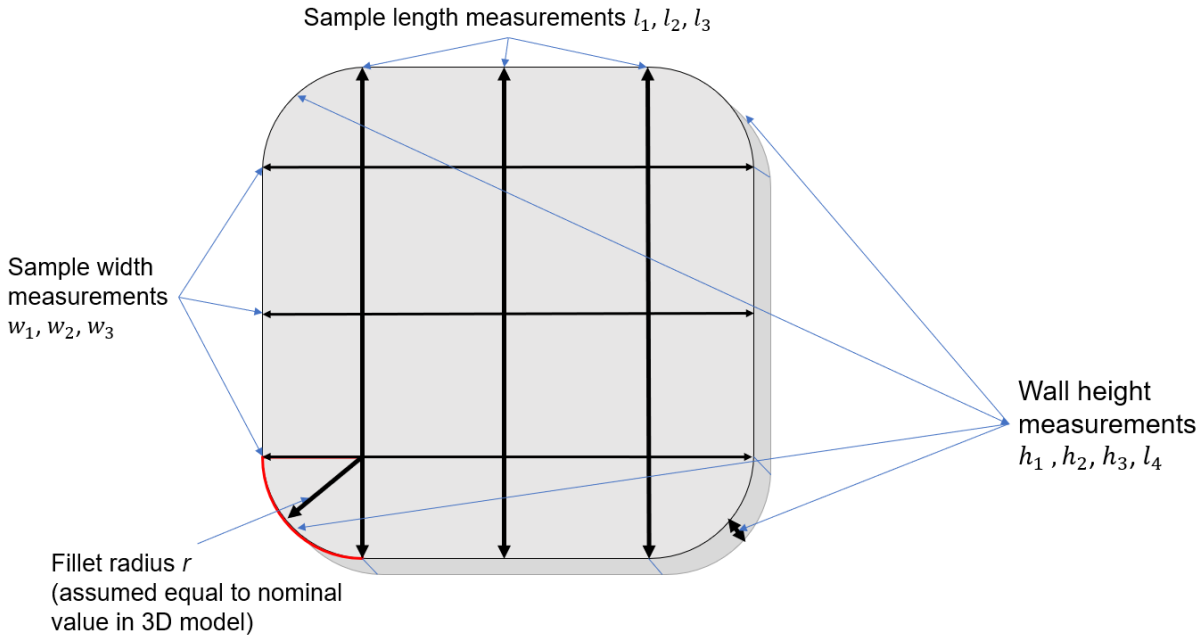

Figure 38 Measured dimensions of OL sample and measurement locations.

As shown in Figure 38, each length/width measurement was taken at 3 locations along the length of the wall; at midpoint and right before the corner fillet. Measurements at different locations are numbered by subscript $_{1\text{-}3}$ and $_{1\text{-}4}$.

7.3 Calculations

Sample volume *($V_{sample\_measured}$)*

The total sample volume $V_{sample\_measured}$ was calculated based on average width *w,* average length *l* and average height *h.* These were calculated as shown in Equations 4, 5, and 6, where l_n are measurements of length (l_1, l_2, l_3) w_n measurements of width (w_1, w_2, w_3), and h_n measurements of height (h_1, h_2, h_3, h_4).

$$l = \frac{\sum l_n}{3} \tag{4}$$

$$w = \frac{\sum w_n}{3} \tag{5}$$

$$h = \frac{\sum h_n}{4} \tag{6}$$

The contained volume of the sample $V_{sample\_measured}$ was calculated as shown in Equation 7, with the average length, width, and height (*l*, *w*, and *h* respectively), and the corner fillet radius *r* (assumed identical to the nominal fillet radius in the 3D model), all in [mm]. A graphical representation of this calculation is provided in Figure 39 and a calculation example in Appendix 6.

$$V_{sample\_measured}\,[cm^3] = \frac{(w-2r)*l*h + \pi*r^2*h + (l-2r)*2r*h}{1000} \tag{7}$$

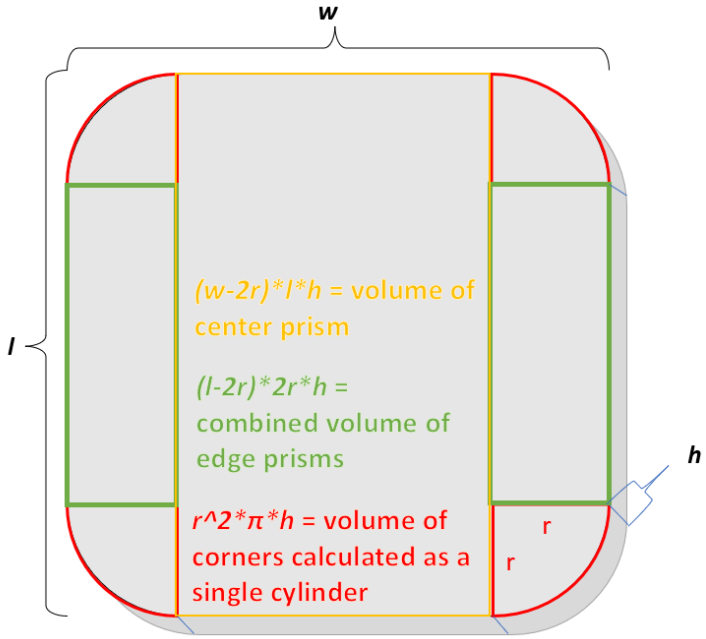

Figure 39 Graphical representation of calculating the internal volume of an OL sample from measurements.

Powder volume (V_{powder})

The volume occupied by powder particles was calculated from the measured mass and ρ_s values, which together with the measured (and nominal) sample volumes would be used to determine four powder packing density values, as shown in Figure 40.

The different powder packing density values and what measurements or values are needed to calculate them are illustrated in Figure 40. For example, "measured packing density" is calculated with the measured volume $V_{sample\_measured}$ and $V_{powder\_measured}$, which in turn is calculated from $m_{powder\_measured}$ using a value of 8.2 g/cm^3 for ρ_s. The same logic is applied to minimum and maximum *PD*. It should be noted that there are no estimates for V_{sample_min} or $_{max}$, only the measured sample volume is used. Nominal *PD* is calculated using the nominal volume, which is provided by the 3D CAD model, and $V_{powder\_measured}$.

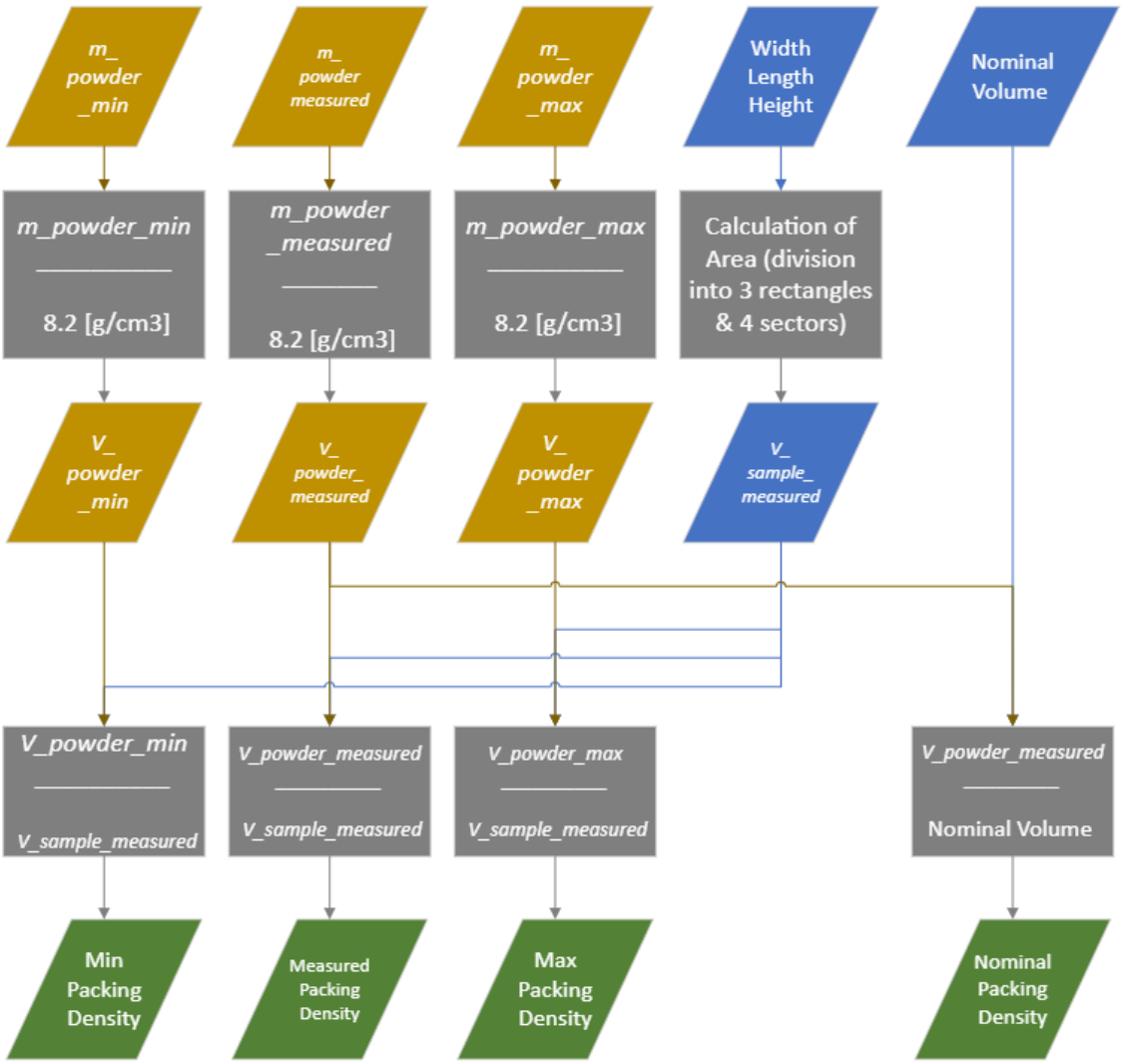

Figure 40 Flowchart depicting connections between measured and calculated values.

Min, measured and max volumes occupied by powder particles (V_{powder}) can be calculated with Equation 8, using the respective powder mass measurement and the characterised ρ_s.

$$V_{powder} = \frac{m_{powder}}{\rho_s} \tag{8}$$

Min, measured and max *PD* were calculated using their corresponding powder volumes and the shared measured sample volume. In the case of nominal packing density, measured powder volume was used with nominal volume, which is based on the theoretical volume of the 3D CAD model of the sample. Every *PD* value was calculated using Equation 1.

$$PD = \frac{V_{powder}}{V_{sample}} \tag{1}$$

A calculation example of powder mass, volume and *PD* is provided in Appendix 7.

8 Experimental procedure (part B: Simulation)

8.1 Particle parameters

The DEM model used by FLOW-3D is a linear spring-dashpot Voigt model. The input parameters for this DEM model and their initial values for IN718 are listed in Table 10.

Table 10 Input parameters for FLOW-3D DEM simulation.

Property	Unit	IN718 value
Particle density	[g/cm^3]	8.2
Restitution coefficient *e*, normal	[-]	0.6
Restitution coefficient *e*, tangential	[-]	0.6
Spring constant	[N/m]	10
Coefficient of friction, dynamic (particle-particle) μD_{pp}	[-]	0.3
Coefficient of friction, static (particle-particle) μS_{pp}	[-]	0.6
Coefficient of friction, dynamic (particle-wall) μD_{pw}	[-]	0.4
Coefficient of friction, static (particle-wall) μS_{pw}	[-]	0.4
Adhesion energy (particle-particle) *SE*	[mJ/m^2]	-
Adhesion energy (particle-wall) *SE*	[mJ/m^2]	-
Particle size range (min - max)	[µm]	10 – 70

The values seen in Table 10 were found by literature review, preliminary simulation tests and practical measurements. Restitution and adhesion are challenging to measure in practice, so they were searched from literature. Restitution coefficient *e* in normal and tangential directions were decided as 0.6 for IN718, which is the lower end of values for *e* as measured by Li et al. (1999) [89], which is in line with values in previous L-PBF simulation works, as is seen in Table 5.

Values of adhesion or surface energy *SE* in literature vary, and thus should be calibrated separately. Due to time constraints and uncertainty on the significance and effects of adhesion on powder particles as described in section 4.1.2, adhesion was not included in the model. The smallest particles are likely affected by VDW forces, but this seemingly does not have a large effect on the powder flow behaviour since the powder does not show signs of agglomeration or low values of Jenike flow function as measured from the shear yield locus [8, 116]. Values for *SE*, should it be implemented later, were aggregated from literature values seen in Table 5.

Spring constant k was found by repeating a simple powder pouring and spreading simulation with different values of k, incremented by 5 N/m from 50 to 5 N/m until flow behaviour begun to be affected. This resulted in k of 10 N/m, as it was the lowest value which did not alter flow behaviour.

Characterised parameters include density, friction coefficients, and PSD. Skeletal density of IN718 measured by pycnometry (ASTM B923-22 [41]) is used as the density of particles. PSD was found by dynamic image analysis (ISO 13322-2 [113]) and friction by rheometry (ASTM D7891-15 [115]).

8.1.1 Conversion of PSD to size classes

Particle size distribution for the simulation is input as 10 size classes and their concentrations. These were found from the measured PSD histogram. The measured PSD histogram and input simulation size classes are shown in Figure 41.

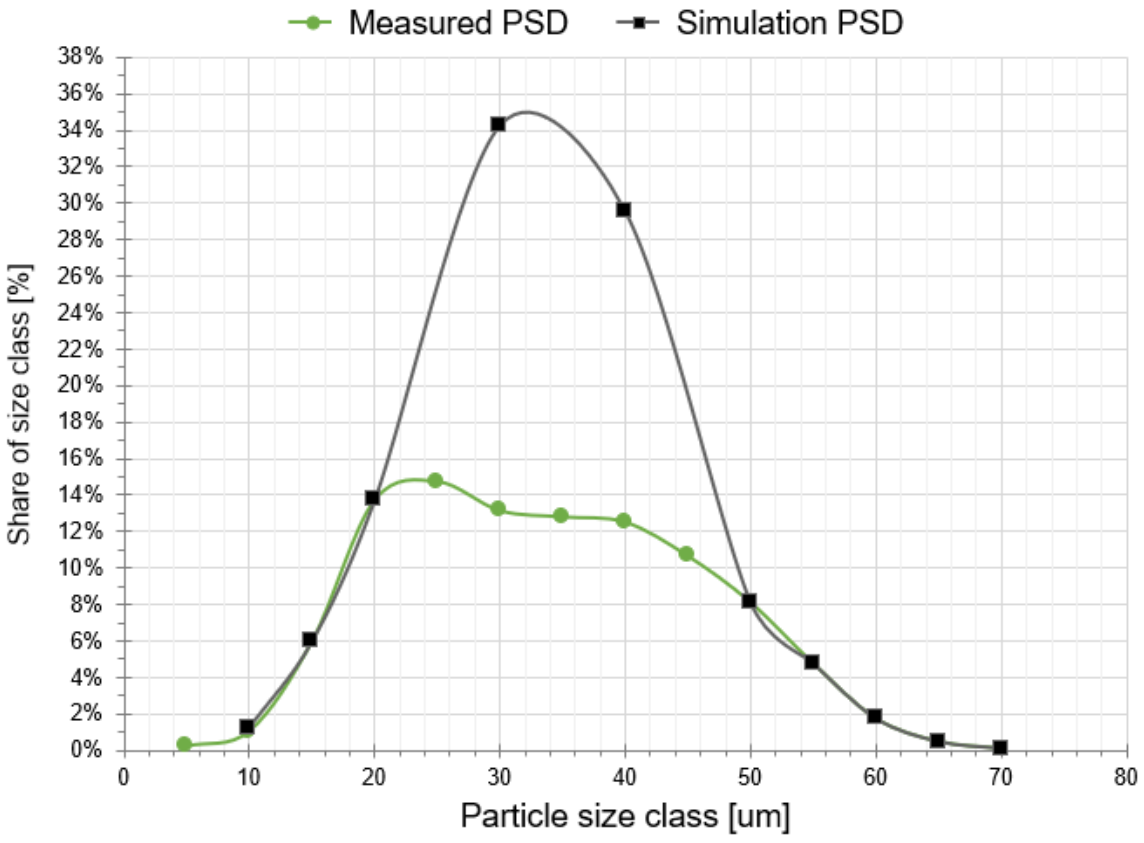

Figure 41 Share of each particle size class of the total particle count of the PSD input into simulation compared to the real PSD characterised by dynamic image analysis.

As Figure 41 shows, the 10 particle size classes were found by removing three of the medium size classes (25, 35, and 45 µm) as well as the smallest class (5 µm) from the measured PSD of the IN718 powder. More emphasis was placed on representing the smallest and largest size classes as their influence on the packing behaviour was expected to be relatively higher compared to the medium sizes between 20-45 µm. These centre size classes were combined into only two size classes, which gives them a very high relative concentration. The smallest class was removed due to its relative insignificance, only representing <0.5 % of the total particles. These very small particles were also found to impact runtime negatively.

8.1.2 Friction parameters adapted from rheometry

The friction coefficients shown in Table 10 were found by using the Freeman Technology FT4 (United Kingdom) rheometer to conduct unconfined flow energy, shear, and wall friction experiments. Unconfined flow is tested by lifting a spinning blade through a powder column, which yields the specific energy Em [mJ/g] of the powder, i.e., the amount of mechanical interlocking and friction which resists flow [122]. Shear cell testing with a shear tool and a wall friction tool (ASTM D7891-15 [115]) yields the angle of internal friction AIF [˚] which can be used to approximate an overall particle-particle friction coefficient, as well as the angle of wall friction AWF [˚] which can be used to approximate an overall particle-wall friction coefficient [122]. Angle of friction is demonstrated in Figure 42.

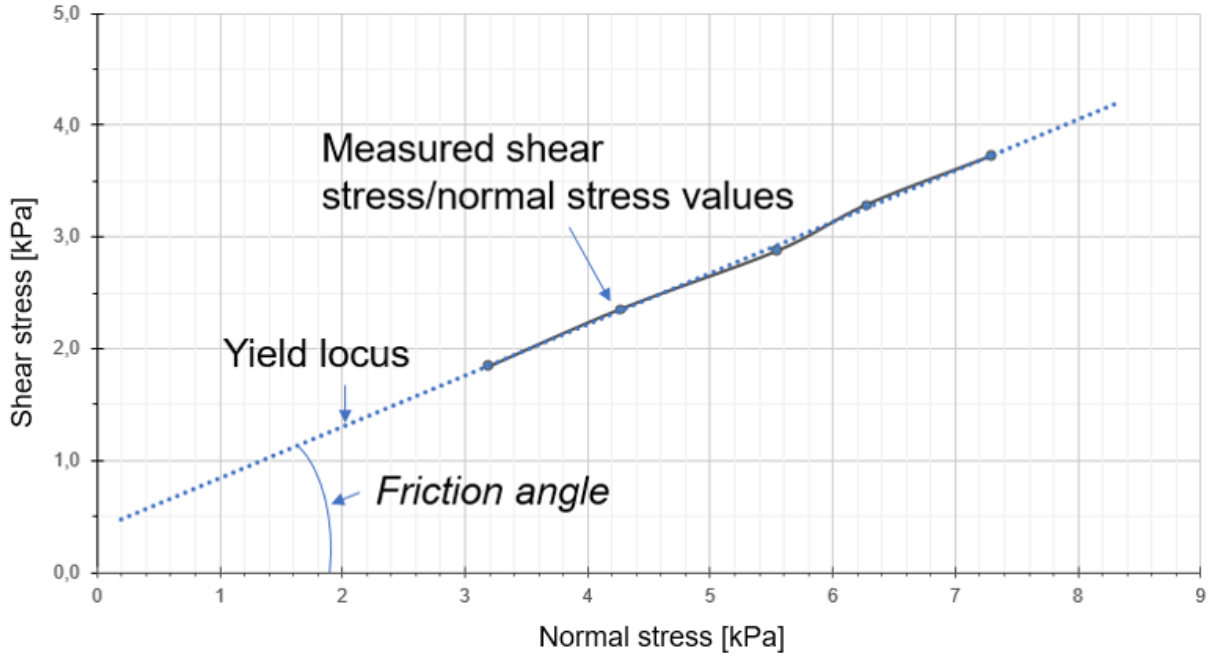

Figure 42 Example graph of shear yield locus and determining friction angle.

As seen in Figure 42, friction angle is the angle of the yield locus of measured normal and translational forces, i.e., the point at which the translational force overcomes the frictional force produced by a normal force and the coefficient of friction. Therefore, the tangent of friction angle is used as the coefficient of friction, μ_{pp} [-] for particle-particle friction and μ_{pp} [-] for particle-wall friction.

Since high values of E_m indicate high interlocking between particles [122], it was assumed that they would correspond to higher particle-particle static friction as well. This could be used to split the overall friction coefficients found by shear cell testing into static and dynamic components. To estimate the scale of E_m from one extreme to the other, highly spherical and non-spherical powder feedstocks were tested on the FT4, as seen in Table 11.

Table 11 FT4 rheometer testing results on IN718 and two benchmark powder materials.

Material	E_m [mJ/g]	μ_{pp} [-]	μ_{pw} [-]
Spherical, smooth particles	1.5	0.33	0.21
Near-spherical IN718	2.9	0.46	0.35
Polyhedral particles	4.1	0.51	0.32

As Table 11 shows, highly smooth, hard, and spherical (sphericity >95%) powder feedstocks were tested as a "low static friction" benchmark, producing values of E_m = 1.5 mJ/g and μ_{pp} = 0.33. It is assumed that for these particles, static friction is small and the total particle-particle friction coefficient (μ_{pp} = 0.33) is mostly formed by the dynamic friction component. On the "high static friction" end of the spectrum, a powder with highly irregular, non-spherical and polyhedral particles was used as a benchmark. This powder has values of E_m = 4.1 mJ/g and μ_{pp} = 0.51. It is assumed that for these particles, friction is mostly formed by the static component.

For the near-spherical (sphericity 89%) IN718 powder, E_m = 2.9 mJ/g and μ_{pp} = 0.46. Due to the rougher surface of the IN718 particles compared to the benchmark smooth particles, dynamic friction is assumed higher, at μDpp = 0.3. Due to the elevated E_m and near-spherical shape (friction coefficients have been successfully used in literature to emulate non-sphericity [123]), static friction is assumed also higher, at μSpp = 0.6. These approximations agree with literature as can be seen in Table 5.

As shown in Table 11, particle-wall friction is ~65% lower than particle-particle friction. It could be reasonable to multiply the already established particle-particle friction components by 65%, but there are some uncertainties. The building platform and blade surfaces are likely rougher than the used *Ra* 1.2 µm wall friction testing coupon, and especially the building platform often features scratches from machining. The wall friction was decided to not be divided into static/dynamic components, and the final values were approximated to be as measured, rounded upwards; $\mu Dpw = 0.4$ and $\mu Spw = 0.4$. Again this is in agreement with literature presented in Table 5.

8.2 Modelled environment

The modelled environment consists of the mesh block, solid geometry, velocities and timing of moving components, the surrounding fluid, and the ambient temperature. The geometry, mesh block and particle generation volume are shown in Figure 43.

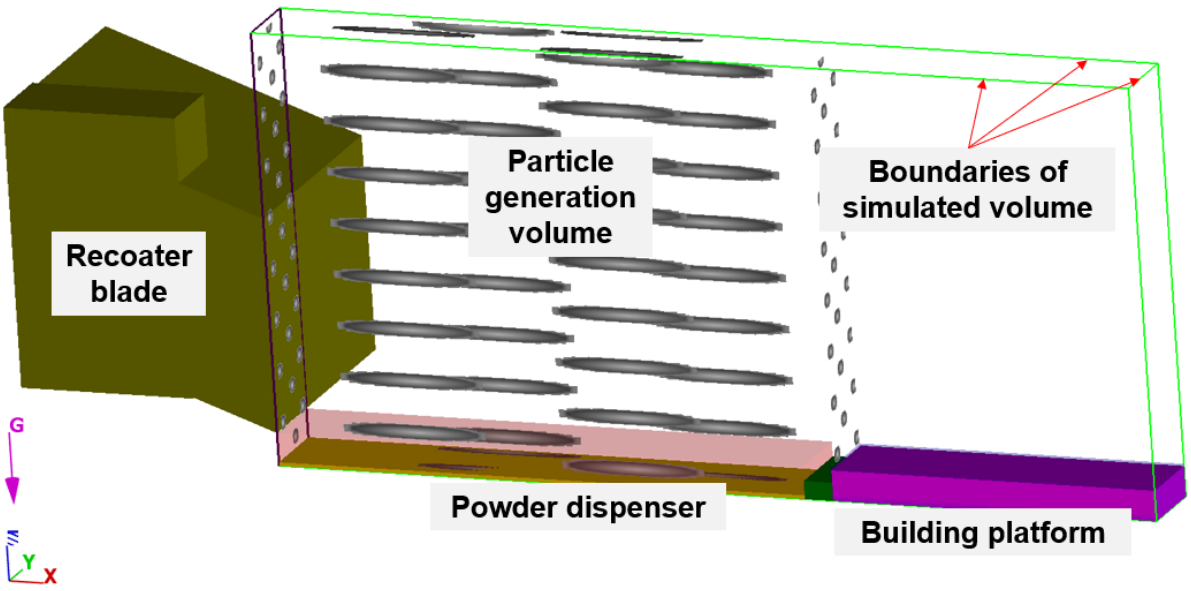

Figure 43 Simulated environment.

As is shown in Figure 43, the environment is a simplified sample of the M 290 L-PBF system. The extents of the mesh block, which act as the boundaries of the simulated volume, are shown with green lines. Particles are generated instantaneously inside the dotted particle generation box on top of the dispenser, after which they are allowed to settle. The dispenser is raised, and the blade moves across the simulated environment in the x-direction, spreading a layer of powder from the dispenser to the building platform, and then returns to its initial location.

As many negligible features were excluded as possible, to simplify iteration and reduce workload and complexity in planning. These features include material properties of solid geometry, controlled ambient and platform temperatures, and the Argon atmosphere. They will be implemented in the future when laser-material interaction is considered. The modelled environment went through a significant number of iterations to improve runtime and improve realism. The common adjustments include powder dosing for recoating (powder dispenser movement), mesh and geometry alignment, mesh dimensions, particle count, and cell size. Number of recoats was also reduced from ten to four to reduce runtime. The parameters of the initial and final model are presented in Table 12.

Table 12 Simulated environment and process parameters.

Property		Initial model	Final iteration
Mesh cell size	[µm]	70	71
Mesh cell count	[-]	351 120	617 253
FAVOR-algorithm iso-surface	[-]	0.5	0.5
Gravity	[m/s^2]	9.81	9.81
Surrounding fluid	[-]	Air	Air
Temperature of fluid	[˚C]	15	15
Boundaries (x min, y min, y max)	[-]	Wall	Wall
Boundaries (z min, z max, x max)	[-]	Outflow	Outflow
Particle generation	[-]	Instant (“block”)	Instant (“block”)
Number of particles generated	[-]	~270 000	~370 000
Model volume (mesh x, y, z dimensions)	[mm]	19.95 x 1.54 x 3.15	17,54 x 1,49 x 8,44
Building platform dimensions (x, y)	[mm]	8.89 x 1.54	6,44 x 1,49
Dispenser dimensions (x, y)	[mm]	10.01 x 1.54	10,05 x 1,49
Recoater blade dimensions (x, y)	[mm]	0.14 x 1.54	5 x 1,49
Recoated layer height (z-axis)	[µm]	40	40
Recoated first layer height (z-axis)	[µm]	40	80
Number of recoats	[-]	10	4
Recoater velocity (x-axis)	[mm/s]	150	150
Recoater return velocity (x-axis)	[mm/s]	-	500
Dispenser movement velocity (z-axis)	[mm/s]	5	variable
Platform movement velocity (z-axis)	[mm/s]	-5	-5

Of the parameters listed in Table 12 one of the most important is the mesh cell size. The cell size should be minimised to increase resolution of solid objects. A hard minimum limit for this is the size of the largest modelled particle. Experimenting with cell sizes significantly larger or barely larger than the largest particle seemed to have little to no impact on runtime or simulation result, so a size barely larger than the largest particle was selected. In order to increase the precision and "sharpness" of corners, the dimensions of both solid objects and the mesh itself should be multipliers of cell size, and preferably all features should be larger than the cell size. In this model the recoated layer height and therefore the difference in level of the building platform and the blade is smaller than the cell size, which is a problem. This was aided by the FLOW-3D FAVOR-algorithm, which interpolates object shapes when they do not follow cell boundaries, as shown in Figure 11. The FAVOR iso-surface value effects the smoothing of these edges, which in this case is unwanted as most surfaces in the M 290 are at a right angle. An optimal iso-surface value of 0.5 was found by experimentation. With this value, the interpolation effect is low and most surfaces are at a right angle, which was desired due to the small size of geometry features compared to the minimum cell size.

The dimensions of the simulated space, i.e., the mesh block, were always set as multipliers of cell size. The mesh block is very narrow in the y-direction, since the width is not expected to affect the packing behaviour, while *PD* is expected to change along the length of recoater travel. Therefore, length was prioritised over width, in order to keep computation time reasonable.

The relative sizes of the building platform and dispenser went through extensive iteration and adjustment to find a good balance between runtime and result quality. The size of the building platform should be maximised as it is the region of interest. But the dispenser will usually need to be larger; a 1:1 size ratio would likely not feed enough powder to cover the building platform in a full powder layer, as some number of particles are usually lost during recoating or the recoating is not perfectly even.

Other modelled geometry includes the dispenser-platform gap and the recoater blade. The gap between the dispenser and building platform was expected to influence particle behaviour during recoating so it was also modelled, though miniaturised by an order of magnitude to the length of 1 mm on x-axis. The recoater blade was modelled after the real steel M 290 blade, as a 70˚ parallelogram profile with a length of 5 mm in the x-axis, as seen in Figure 44.

The y-dimensions of all geometry objects were to extents of the mesh block.

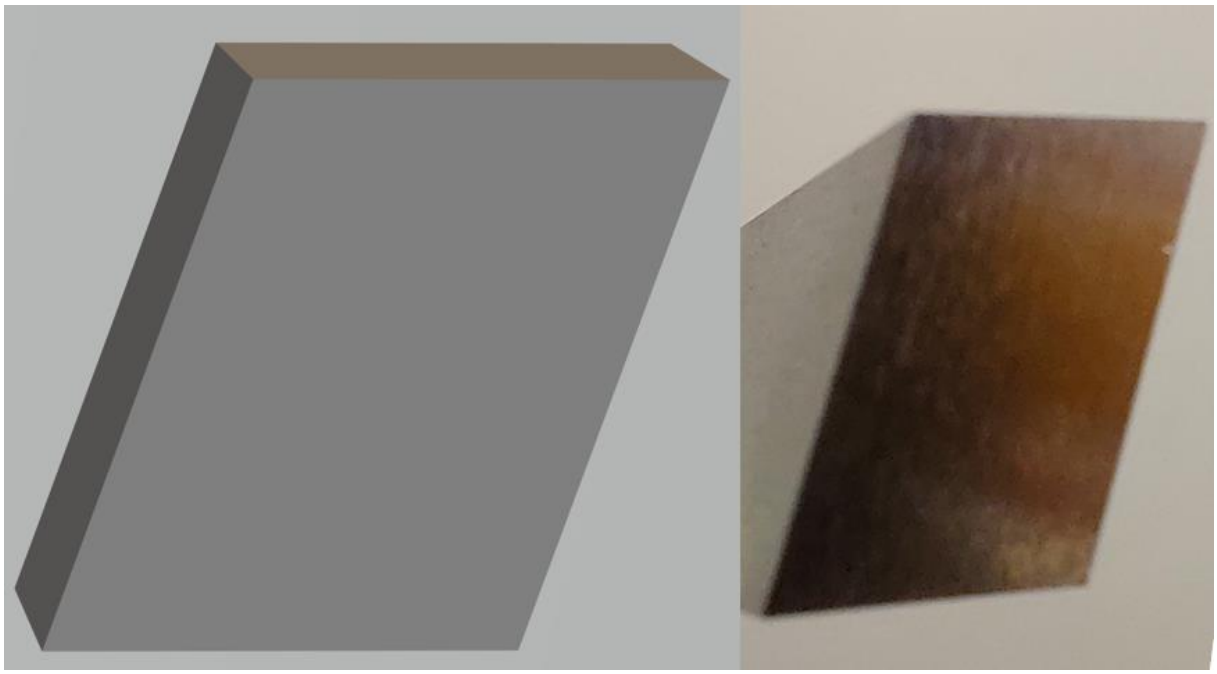

Figure 44 Comparison of modelled and actual M 290 steel blade profiles.

As seen in Figure 44, the recoater blade was modelled after the real blade. It should be noted that due to the relatively coarse cell size of the mesh, the slanted front and back edge of the blade are somewhat “pixelated” in the simulation.

Most processing parameters listed in Table 12 were directly implemented from the M 290 process parameters for the IN718 40 µm layer height process. Some were adjusted to better suit the simulation:

- Dispenser movement velocity was increased and the time between component motions were reduced in effort to reduce computation time, as these parameters are not expected to influence the packing behaviour.

- The real M 290 moves its building platform down multiple millimetres before the recoater returns to its starting position behind the dispenser, and only then moves it up to the desired height. This back-and-forth motion of the building platform was not modelled to save on computation time and complexity, instead the modelled platform simply moves down by one layer height after recoating.

- Argon atmosphere in the real process was replaced by room temperature air at ambient pressure (100 kPa), as it was available as a comprehensively parametrised template in

FLOW-3D. The effect of the surrounding gas composition was not expected to effect packing behaviour.

- Thermodynamic properties were not specified to geometry. In the real process, the building platform would be heated to 80 ˚C, but the effect on packing behaviour was considered negligible. Inclusion of thermodynamic physics models would also increase computation time.

8.2.1 Parameter calibration

After the initial simulated environment was built and particle parameters found through measurements and literature review, the simulation could be ran and preliminary results analysed. An inbuilt particle packing density tool in FLOW-3D was used to find the simulated *PD*. The simulation model was modified to steer the *PD* towards the *PD* found in validation, until the simulated *PD* matched that of the validation experiment.

Calibration of input parameters such as coefficients of friction is a common method in literature, as seen in Table 6. However, it was decided that material property calibration is left as a last resort, as it requires time-consuming iteration and is not guaranteed to affect *PD* significantly [70]. The largest effect on *PD* was expected to be from h_l, the number of recoated layers, and PSD. The following features or parameters were adjusted iteratively:

- Adapting PSD from measurement data to a 10 size class distribution for FLOW-3D can be done in many ways, so different methods for adapting this data were be tried and the one with best match to validation was chosen.

- Layer count was initially aimed to be 10, but runtime constraints limited it to four.

- The first layer height was doubled to 80 µm, as a single 40 µm layer deposited very few particles. In effect, the simulated powder bed is five layers thick despite only having four recoats.

- Powder dispenser was timed to increase powder dosing towards the end of simulation

- Cell sizes between 71 and 80 µm were experimented with, but no effect was seen.

8.3 Result characterisation method

The simulation result is the powder packing density in the simulated powder bed which is equivalent to the developed validation experiment. *PD* is measured from the completed simulation run using a particle-to-STL converter tool included with FLOW-3D, which features a particle packing density calculator. This tool uses a rectangular sampling volume defined with cartesian planes. Since *PD* is a fraction of volume occupied by particles, the way this volume is defined may have a significant impact on the *PD* value. The following methods were intuitively recognised or found in literature:

1. By nominal dimensions. In a case of powder being recoated on a building platform, an obvious choice could be to define the volume as the entire area of the platform multiplied by the nominal layer height. This produces a low packing density as the true layer height rarely reaches nominal layer height. Sometimes this can be the wanted density, e.g., to meet the measured *PD* of a tightly controlled validation experiment, but it does not describe the actual density of the powder bed on which the laser beam is focused. Also, if an open cup type validation experiment is used (such as in this thesis), the height of the cup walls will likely not be the same as the nominal height of the layers due to the apparent shrinking of the metal material as powder melts and solidifies. Therefore, this method may not yield accurate PD values in most practical cases.

2. By the extents of the outermost particles. This way the particles are completely contained within said volume but there is little empty space between the outermost particle and the planes of the sampling volume. This method can produce a more accurate absolute *PD* value of the powder bed but is difficult to execute repeatably.

3. By fully embedding the sampling volume in the powder bed. Here, the planes and edges of the volume always cut through particles. In this case, unlike in the two previous methods, there are no wall-particle interfaces, which will result in a higher packing density compared to the previous methods. The sampling volume planes cutting through particles is much more efficient in terms of packing structure, compared to a particle-wall interface which interferes with efficient packing of the particles. The advantage is that the planes of the sampling volume can be predefined and repeated across experiments, as there is no need for fine tuning the volume according to particle extents. [70, 124]

4. By a combination of these three, which is the method used in this thesis. In this example, the bottom and sides (bottom xy- and both xz-planes respectively) of the powder bed are defined by method 2 to contact the extents of outermost particles. The top surface of the powder bed (top xy-plane) is defined as passing through an approximated average height, so that approximately an equal area of cut particles and empty space is included. The front of the powder bed (bottom yz-plane) had to be defined as embedded planes (method 3) as the powder reservoir and powder bed do not have a "cut off" or physical division between them. The top yz-plane was placed according to method 3 at the location where the height of the powder bed began to decline near the end of recoater travel, likely due to insufficient dosing of powder from the powder dispenser.

To find the magnitude of possible error resulting from mixing these sampling volume definitions, *PD* is measured using each method (note that the bottom yz-plane at the front of the powder bed is always measured with method 3). These measurements are called $PDmin_{sim}$, $PDmax_{sim}$, and $PDmeasured_{sim}$. $PDmin_{sim}$ is measured using method 2. This method is expected to yield the lowest *PD*. $PDmax_{sim}$ is measured using method 3 and is expected to yield the highest *PD*. $PDmeasured_{sim}$ is measured using method 4 and is expected to be the closest analogue to the way *PD* is measured in the validation experiment.

In addition, these three measurements are taken from both the visually identified "stable region" where the powder bed thickness does not change, as well as the entire length of the powder bed. This was done to see whether there is notable change in *PD* between the entire length and the stable region, as this information may be important for the *PD* measurement of future simulations. Additionally, it is thought that sampling only the stable region is more representative of the validation experiment where only the first half of the powder bed, which is expected to be more stable than the rear half [60], is sampled.

9 Results and discussion (part A: Validation)

9.1 Powder packing density

The open cup validation experiment was repeated with five samples, named OL1-OL5 (Open cup, Large). Packing density values are presented in Table 13 and illustrated in Figure 45, while the full dataset with all measured and calculated values can be found in Appendix 7. The minimum and maximum values represent the greatest negative and positive error resulting from the sample removal and weighing process, and the measured value is the baseline *PD* measurement, which is expected to be closest to reality.

Table 13 Validation experiment packing density results.

PD	OL1	OL2	OL3	OL4	OL5	Mean	Standard deviation	Coefficient of variation
Minimum	51,9%	51,9%	52,2%	52,6%	52,5%	52,2%	0.29%	0.006
Measured	52,2%	52,2%	52,3%	52,6%	52,6%	52,4%	0.20%	0.004
Maximum	52,2%	52,2%	52,3%	52,7%	52,7%	52,4%	0.22%	0.004
Nominal	54,0%	52,4%	53,0%	52,8%	53,5%	53,2%	0.56%	0.010

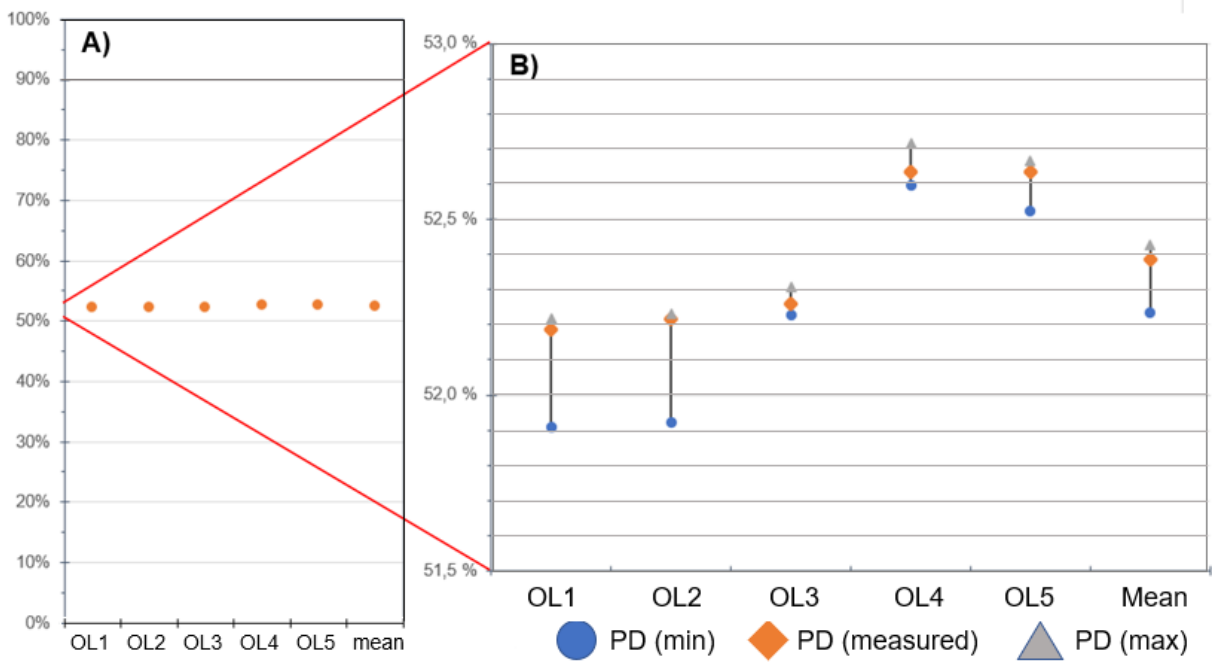

Figure 45 Validation experiment packing density results visualised. A: measured *PD* on a full scale, B: zoomed-in section with minimum and maximum *PD* values presented.

As can be seen from Figure 45 B and Table 13, *PD* in the sample regardless of measurement technique is approximately 52 %, except for when using nominal volume values. The measured *PD* are between minimum and maximum *PD* in all samples, as expected.

9.2 Sources of uncertainty

The minimum and maximum PD values were measured to find the error resulting from powder spillage or residue which might result from cleaning or emptying the sample. Greatest difference between min and measured values is in samples OL1 and OL2, with a difference of 0.3 percentage points (or a difference of 0.6 %). The maximum *PD* values on the other hand have less difference to measured values, indicating that the samples have low error due to residual powder and other debris, and powder loss is the most significant error from handling. I.e., the error resulting from too thorough clean-up is much lower than the potential error from inadequate clean-up. Overall, the results show that the used measuring and cleaning method has very low error, especially in the positive direction.

In the bottom row of Table 13, *PD* values for "nominal *PD*" are presented. This is a value where the *PD* is calculated using $m_{measured}$ and $V_{nominal}$ which is the volume of the 3D CAD model of the sample. The purpose of this value is to quantify the difference in physical dimensions of the samples and its effect on the *PD*. An intuitive thought would be that the sample size, internal volume, and powder volume always grow linearly, and therefore the sample dimensions should not affect the *PD*. But this should not be taken as an obvious fact. Some L-PBF process mechanics which affect the sample dimensions may not affect the powder volume, for example the thickness, uniformity, and levelling of the manually deposited first layer. Also, a scratched or dimpled building platform will naturally hold a different volume of powder than a perfectly flat platform, even though the measured dimensions of the samples are the same and therefore no indication of this change in volume is seen in the sample measurements. The nominal *PD* values are normalised by sample volume, and therefore when compared to measured *PD* values, give indication for unseen deviations in sample volume; the larger the nominal *PD*, the larger the true powder volume. Measured dimensions of OL samples can be found in Appendix 8.

As Table 13 shows, the coefficient of variance in nominal *PD* is 0.01, indicating very low deviation in sample dimensions, first layer deposition, or building platform geometry. Also, there is no meaningful correlation between minimum, measured, or maximum *PD*s and nominal *PD*s; greatest correlation can be found between nominal and measured *PD*, with a correlation factor of -0.16. This gives sufficient confidence that *PD* determined with the presented method

is not affected by L-PBF process -related deviations in sample volume. The impact of these dimensional inaccuracies is crucial to know, since the simulated environment will always be ideal, with no stochastic deviations in built part dimensions, surface irregularities in the building platform, or human error in depositing the first layer, but in the real world these variations are practically unavoidable. A strong correlation between nominal and measured *PD* could have indicated that *PD* (as measured with this method) varies as a function of some sample dimension, which would need to be further studied and somehow accounted for in powder bed simulations. Since no correlation was seen, the effect of sample dimensions or building platform geometry on *PD* does not need to be considered in future applications – at least as long as the sample dimensions are known to fall within the range of the sample dimensions measured in this experiment.

Interestingly, all samples had a larger volume than the 3D CAD model. This was against expectations, since L-PBF built parts that are short in the z-direction, such as the OL samples, can be expected to be slightly shorter than their CAD model due to thinner true h_l in the first 10 or so layers [41]. A likely explanation could be simple measuring error, or that the hand-coated first layer was too thick.

The *PD* seems to have an increasing trend, but this can mostly be explained by human factor. As proficiency in handling the samples increases with each sample, less powder is lost.

The maximum variance in the sample set is between the minimum *PD* of OL1 and the maximum *PD* of OL4; 0.8 percentage points or 1.6 %. Therefore +-1.6% can be considered as the maximum range of results variability for the presented open cup *PD* characterisation method for future applications. The largest unanswered uncertainty with this method is that of sample clean-up in the system chamber. Powder may be accidentally brushed off or carried by airflows resulting from hand movements inside the chamber, and this cannot be accounted for with this method. An in-situ version of this *PD* characterisation method would be needed to determine a more comprehensive error range.

10 Results and discussion (part B: Simulation)

10.1 Powder packing density

The three *PD* sampling volumes and resulting *PD* values for the stable region of the powder bed are shown in Figure 46.

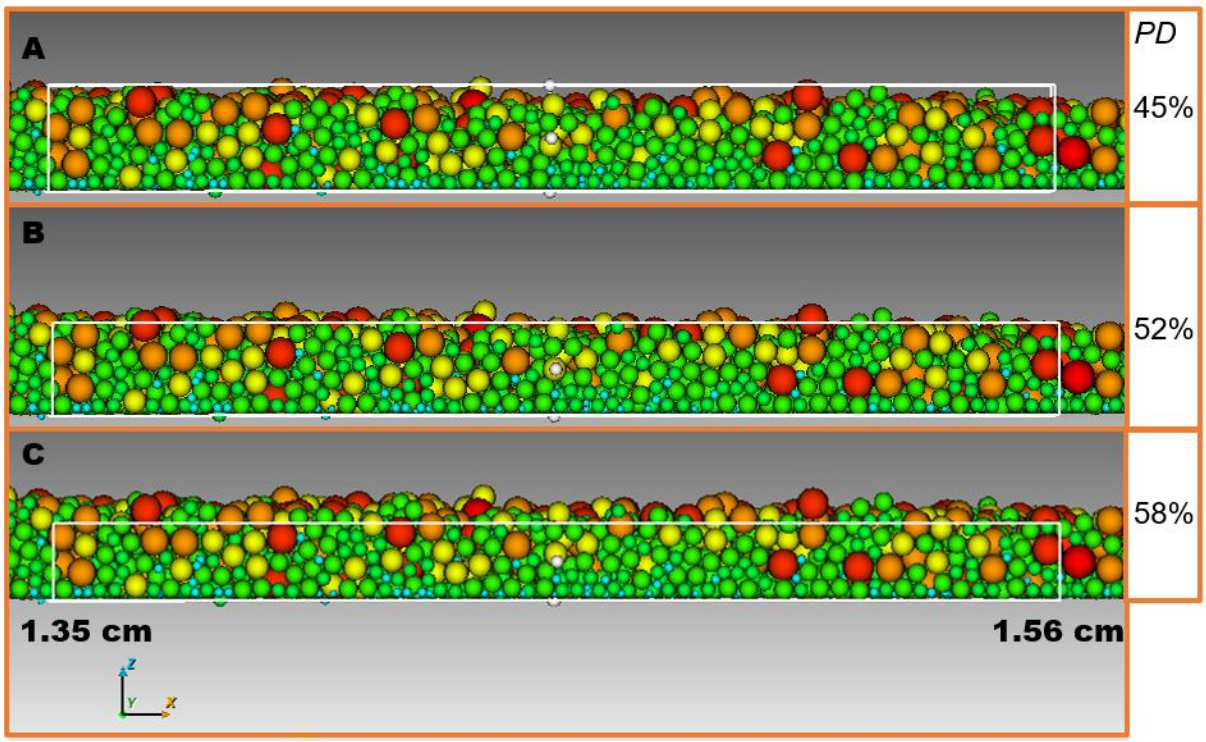

Figure 46 *PD* in stable region of the simulated powder bed. A: measurement method 2 ($PDmin_{sim}$), B: method 4 ($PDmeasured_{sim}$), C: method 3 ($PDmax_{sim}$).

As is seen from Figure 46, *PD* varies between 45-58 % depending on the measurement method. Methods 2 and 3 were used for Figure 46 A and Figure 46 C respectively and yielded slightly lower and higher values as was expected. The method 4 measurement from the stable region as seen in Figure 46 B was considered the best representation of the *PD* measured from the validation experiment, and thus its value needs to match the validation experiment to validate the simulation. This measurement produced a *PD* value of 52 %, which matches that of the validation experiment within one percentage point, and the simulation model can be considered validated by *PD*. A tilted perspective view of $PDmeasured_{sim}$ is provided in Figure 47.

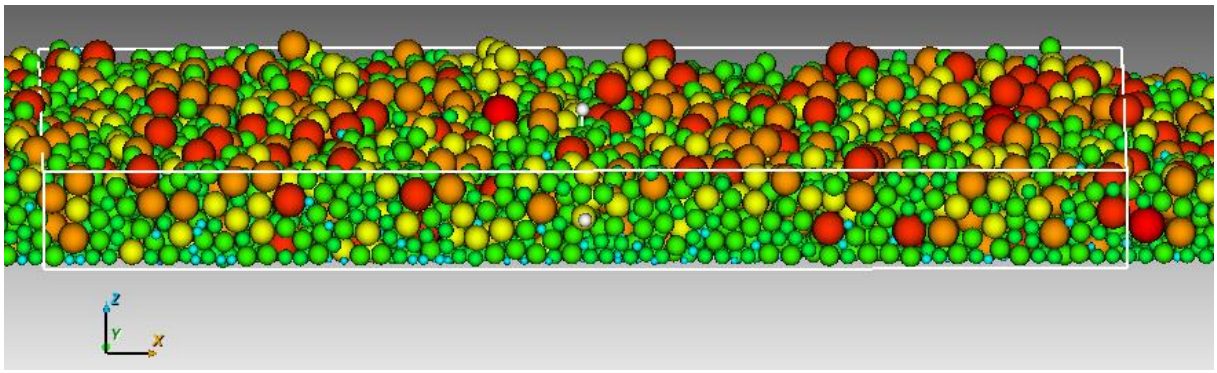

Figure 47 Tilted view of *PDmeasured*$_{sim}$.

As shown in Figure 47, the top xy-plane is placed so that the area of cut particles and empty space are approximately equal. Small variations in the plane location (i.e. variations that are small enough to not be reasonably considered method 2 or 3 type measurements) had no more than two percentage points difference in *PD*.

The simulation run was repeated with same parameters, and identical measurements were taken. These resulted in identical *PD* values for *PDmin*$_{sim}$ and *PDmax*$_{sim}$, while *PDmeasured*$_{sim}$ was 53%, one percentage point higher than in the first run. It should be noted that the simulations are not completely deterministic as the initial particle generation is randomised.

The same three *PD* sampling volumes and resulting *PD* values for the full length of the powder bed are shown in Figure 48.

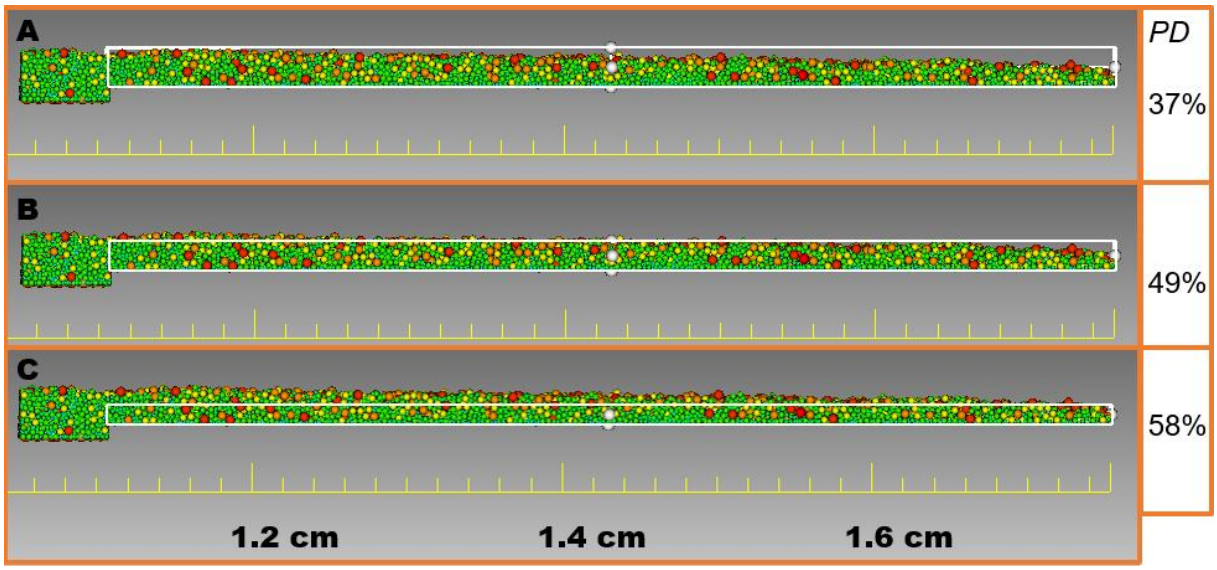

Figure 48 *PD* in entire length of the simulated powder bed. A: measurement method 2 (*PDmin*$_{sim}$), B: method 4 (*PDmeasured*$_{sim}$), C: method 3 (*PDmax*$_{sim}$).

As is seen in Figure 48, the *PD* for the entire length is lower than for the stable region, as expected. This is mostly likely due to the fact that the powder bed surface dips below the top xy-plane of the sampling volume near the end of recoater travel, leaving more empty space in the sampling volume. This is supported by the fact that the measurement using method 3 in Figure 48 C has identical *PD* to the corresponding measurement in the stable region, while the method 2 value in Figure 48 A is 8 percentage points lower compared to the stable region. For the method 4 measurement in Figure 48 B, *PD* is three percentage points lower, likely caused by the same lack or powder at the end of recoater travel. This indicates that using the full length of the powder bed for *PD* measurements may yield low values, unless the powder dosing issue can be solved. This is important since the validation experiment likely does not have a similar issue due to the frontal location of the sampling area.

It should be noted that *PD* in simulation should not be higher than in validation, but there may be reason to believe it can be lower than validation *PD* while being considered validated. This is because intuitively *PD* should increase with the number of layers as the weight of the powder compresses itself, and the simulation has an order of magnitude fewer layers than the validation.

In the repeated simulation run, values of $PDmin_{sim}$ and $PDmeasured_{sim}$ were two percentage points higher (51% and 39% respectively) while $PDmax_{sim}$ was unchanged (58%). The sampling methods 2 and 4 (min and measured *PD*) are most affected by changes in powder bed thickness, and the repeat run featured a visibly more uniform bed thickness. Therefore it can be safely assumed there is little to no variance in actual packing structure between simulation runs, though it is possible for the powder bed uniformity to change. It is recommended that in the future when comparing simulation runs to each other (and not a validation experiment), the measurement method 3 is used.

More details on the repeat simulation run are provided in Appendix 9.

10.2 Particle behaviour during recoating

In order to understand the particle packing behaviour, the entire recoating process was analysed and *PD* was also measured from the powder dispenser as shown in Figure 49.

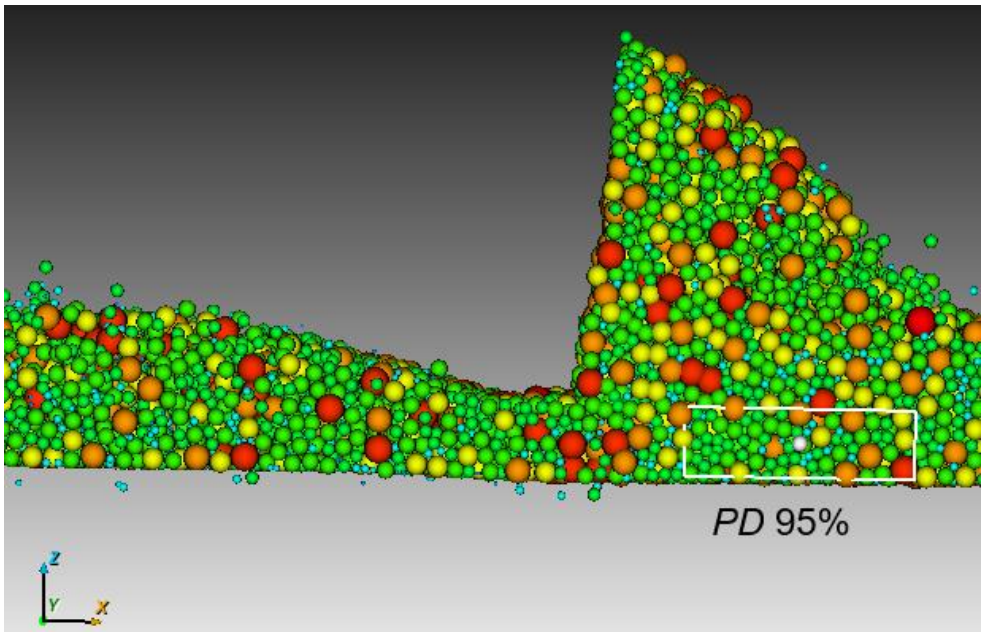

Figure 49 Compression in the dispenser before the recoater blade.

As seen in Figure 49, powder bulk in the dispenser is compressed in front of and under the recoater blade and decompressed after the blade, indicating that the blade has a compressive force on the powder bulk in the dispenser. *PD* measured from the white box is 95%, which should be practically impossible, suggesting the compressive force is large enough to cause a normally unallowed overlap between particles. However, it should be noted that the sampling volume is completely embedded in the powder bulk, which increases the *PD* measurement value by up to 10 percentage points compared to the likely true *PD*. The compression causing an elastic overlap in the particles is also evident from the fact that there is an updraft or wave of powder immediately following the blade as the powder decompresses and elastic force is released. Such a degree of elasticity is unlikely to occur in real metallic particles, which means that the spring constant may need its own calibration for future experiments. However, it is not likely that this elasticity under compressive force affects packing in the powder bed, as the particles are mostly deposited by gravity and not a significant normal force. Compressive force in the dispenser is larger likely due to the blade impacting relatively deep into the mass of the powder bulk.

Another effect of the blade impacting the powder bulk is the significant spray of particles seen in Figure 50.

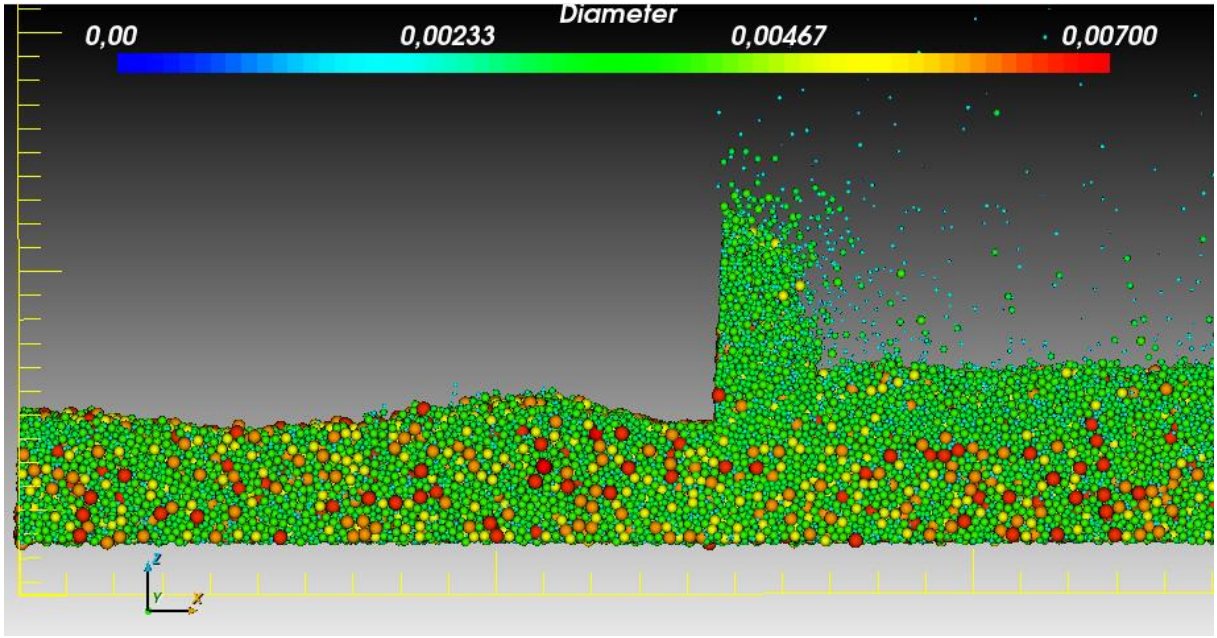

Figure 50 Finer particles being sprayed as the recoater contacts powder in the dispenser

As seen in Figure 50, small particles are sprayed far and wide as the blade enters the dispenser for the first time. It is not known whether the spray phenomenon occurs in a real L-PBF process as well, as the powder flow behaviour is not separately validated. It can be that this spray does not exist in reality in the same scale due to VDW forces binding together the smallest particles, which is not accounted for in this simulation.

Another interesting phenomenon seen in Figure 50 is the separation of small and large particles in front of the blade. As the blade moves through the powder bulk, the smaller half of particles seem to percolate to the top due to some internal flow in the powder bulk. A rotating flow or vortex likely exists in front of the blade though, as large particles are eventually picked up as well, as is seen in Figure 51. Similar vortex and compression phenomena were also observed by Wu et al. (2022) [52].

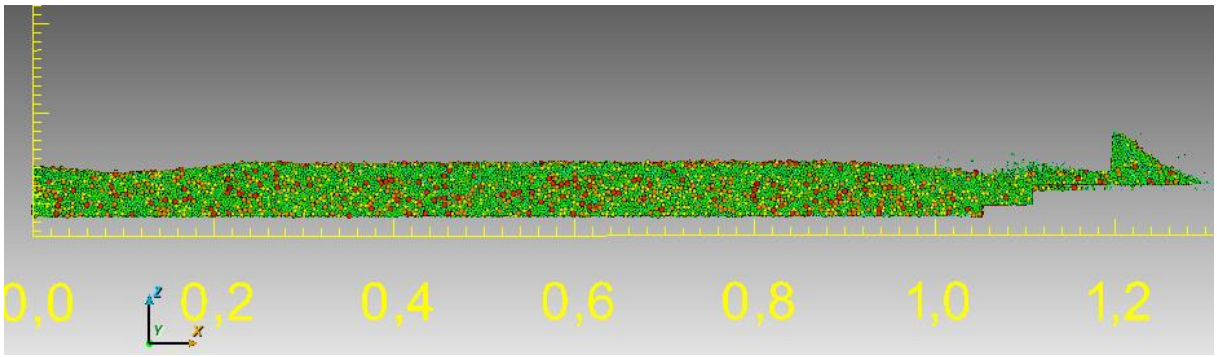

Figure 51 Powder dispenser after the blade has picked up powder for first recoat.

As is seen in Figure 51, large particles are mostly separated to the bottom of the powder bed, though there is a concentration of larger particles on the very surface as well, which could support the vortex theory. Once the recoater blade has exited the dispenser, it begins depositing powder onto the building platform as seen in Figure 52.

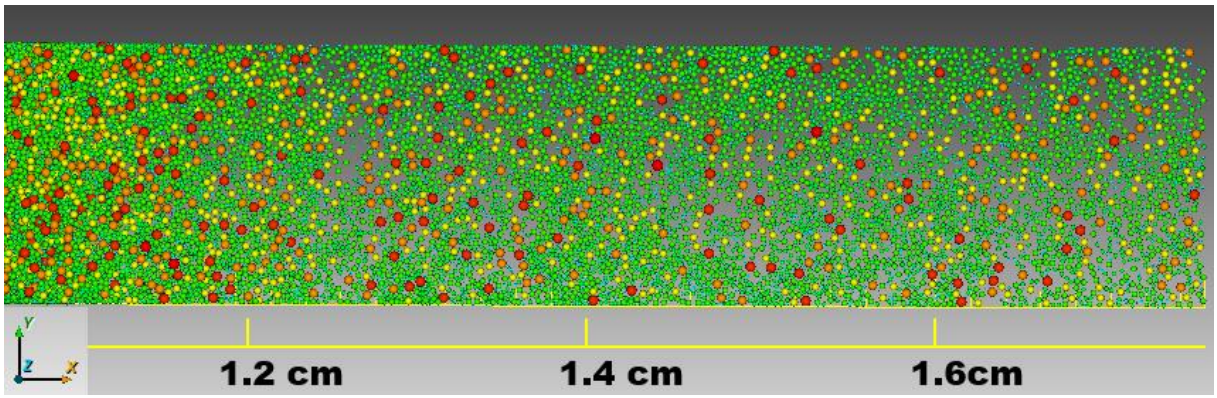

Figure 52 Top-down view of the first recoated layer.

In Figure 52 a top-down view of the first powder layer is seen. It is ununiform and the coverage is not complete, which was expected. Interestingly, the share of large particles is not drastically smaller than in the dispenser despite the observed separation phenomenon. Especially the front of the powder bed seems to have a high concentration of large particles. A side profile view of the first layer is shown in Figure 53.

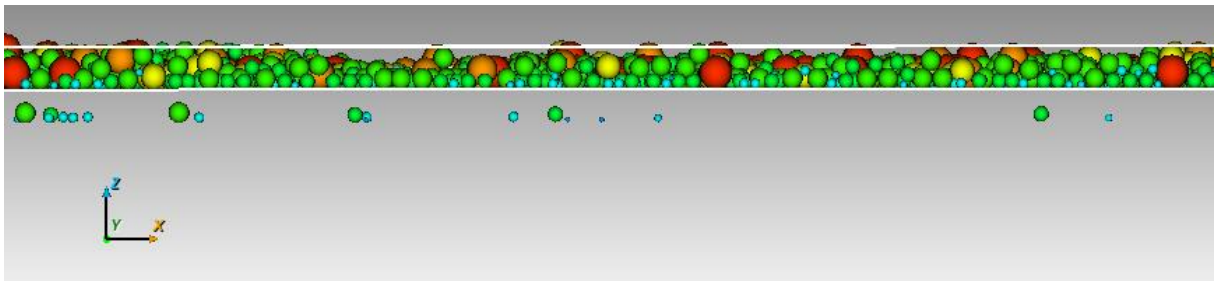

Figure 53 Detail of the side profile view of the first recoated layer.

As seen in Figure 53, the areas where particles are deposited are nearly equal to nominal layer height (80 µm for the first layer), indicated by the white line. Some particles seem to be sunken inside the building platform, which may decrease *PD* slightly as particles are "lost" during recoating. Reason for this sinking is unclear.

Figure 54 shows a side-by-side view of the second layer during and after recoating.

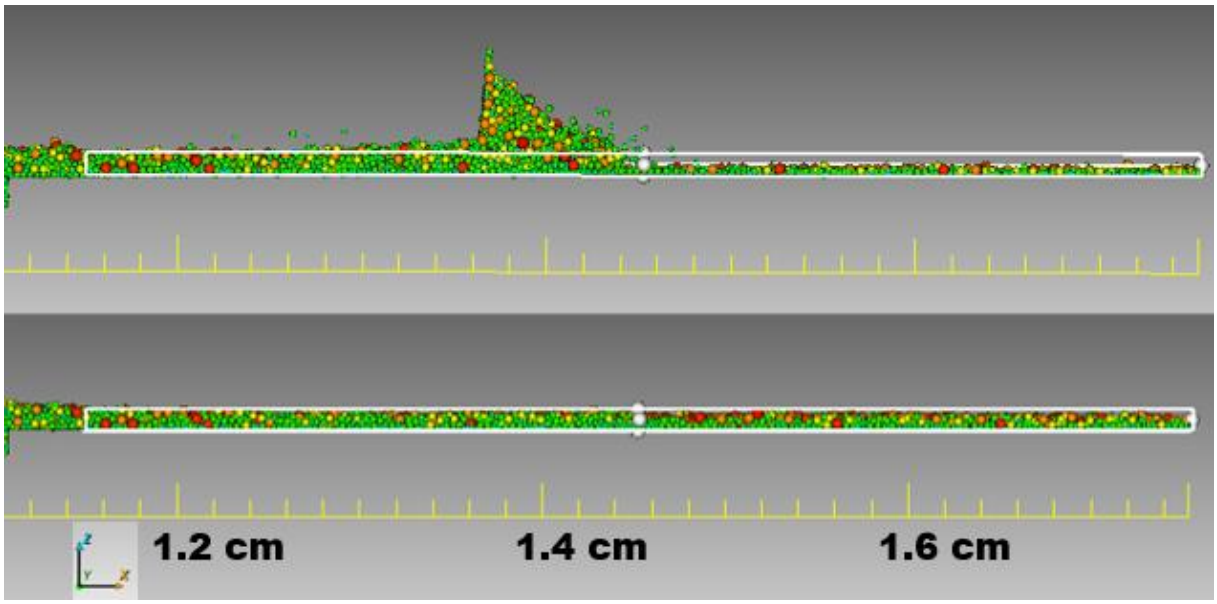

Figure 54 The second layer during and after recoating.

As seen from Figure 54, the second layer is also near to nominal total powder bed depth (80 µm + 40 µm = 120 µm) indicated by the white box. Powder seems to be running out at the end of recoater travel, leading to the aforementioned dip in powder bed depth at the end of the powder bed. The previously noted compression/decompression and spray is again observed as the blade deposits powder onto the powder bed.

The third layer after recoating is shown in Figure 55.

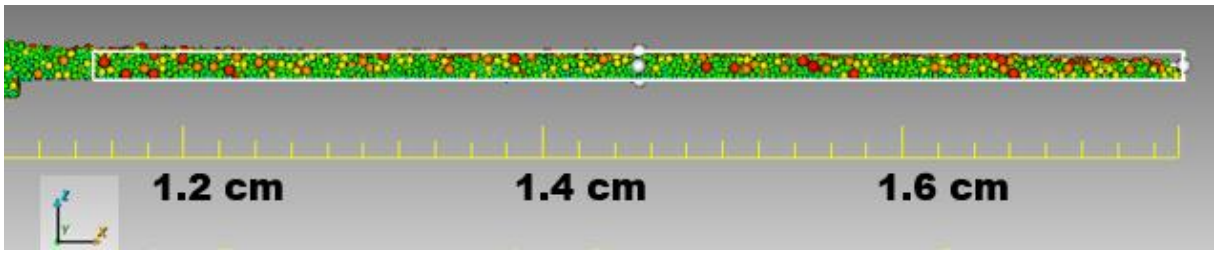

Figure 55 Third layer after recoating.

As seen in Figure 55, the powder bed is near to its nominal depth (160 µm) indicated by the white box. The dip at the end of the powder bed is becoming more pronounced.

The fourth and final layer is shown in Figure 56.

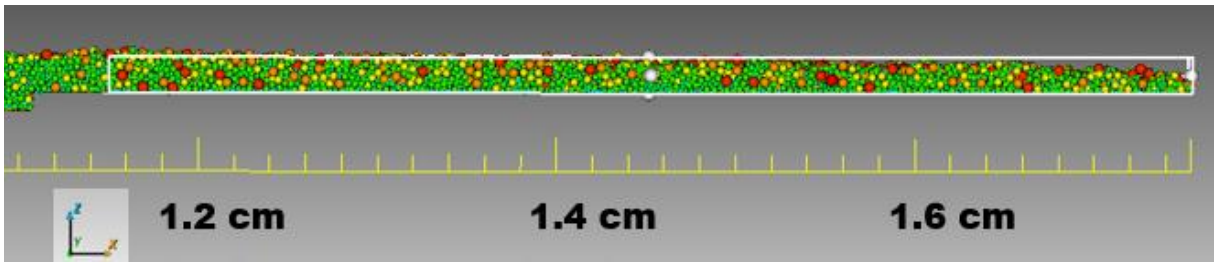

Figure 56 Fourth and final layer after recoating.

As seen in Figure 56, the front of the powder bed is above the nominal powder bed height (200 µm) indicated by the white box, which could again hint at the compression of powder in front of the blade and a decompression behind it. The end of the powder bed is below nominal height, and between the two extremes is a stable region with a good match to nominal powder bed depth.

10.3 Sources of uncertainty

Since the simulation is a representation of reality based on rough measurements and estimates, there are always many uncertainties. Physical measurements always have error, though in a simulation such as this the measurement error may be negligible compared to the error resulting from translating the measurements into input parameters, which are only simplified representations of the real physical properties that were measured. For example, the friction coefficient of a particle is only a simplification of multiple physical phenomena; interlocking, rolling resistance, adhesive forces, contaminant particles, and friction.

A parameter with a large effect on packing is the PSD. PSD is inputted as 10 size classes, which is a very coarse approximation of the true PSD. Depending on which size classes are chosen from the dynamic image analysis or laser diffraction data, the resulting input PSD may change significantly. Also it should be decided whether to use a constant “resolution” of size classes or focus on large, small, or mid-size classes, all of which affect packing behaviour differently.

Besides PSD, the particles are simplified in shape as well. Real particles feature defects and may not be completely spherical. FLOW-3D only supports spherical particles for now, so an effort was made to choose higher values of friction to emulate the rolling resistance of non-spherical particles. The effect on *PD* of non-spherical particles compared to spherical particles was found by Gao et al. (2020) [108] to be less than two percentage points, so it can be assumed that error in *PD* arising from sphericity is not the main concern.

In this simulation work, many physical properties of the objects and particles are simplified to a simple friction coefficient and a smooth surface. Some surfaces, like the backside of the blade, are pixelated. The simulated powder bed is also a small sample of the real system with a higher solid surface area to powder volume ratio, which may cause a pronounced wall effect in powder packing; packing structures at the wall-powder interface are less dense than in bulk powder.

Many process features are also ignored in this simulation; for example, the real building platform is moved down and up after each recoat, which may compact the powder. Also, the powder is poured into the dispenser from higher altitude than in simulation, which may compact it. Other vibrations during processing may also influence *PD*.

Besides parameters, there are uncertainties regarding the discrepancies between validation and simulation. The powder bed thickness of the validation sample was about 20 times higher than in the simulations which was only recoated four times. It could be assumed that a thicker powder bed compresses under its own weight, increasing *PD*. Furthermore, measuring the exact volume of the *PD* sampling volume in the validation sample is difficult and measurements often featured up to 0.1 mm of deviation, though the *PD* values between samples were very uniform. Also, applying the sampling volume measurement directly to the simulation is impossible. In the validation sample, only the volume of the sample is measured, but mass of powder outside the volume is also included in the *PD* calculations. For example, the powder bed may well be taller than the built wall which is measured, in which case the measurement yields too high *PD* values and cannot be exactly replicated in simulation.

11 Conclusions

EOS Finland aims to aid the development of Tungsten powder feedstock by computer simulation. The goal of this thesis was to develop a simulation model of the powder bed recoating process to act as a proof of concept and platform for future development of a more comprehensive simulation model. Development of this preliminary simulation model would also include its validation using a purpose-built validation experiment.

Literature on previous powder bed simulations and powder bed characterisation studies was reviewed to compile information about the relevant powder bed parameters, calibration methods, validation methods, and typical input values for material properties. Powder packing density *PD* was found to be the most relevant powder bed parameter, and the best-suited characterisation method was considered to be the "open cup" experiment. A variety of calibration experiments were also found and their ideal use cases identified. All necessary simulation input parameters were also available in literature.

An "open cup" validation experiment was developed based on findings in literature. In this experiment, a thin wall enclosure is built with the L-PBF process, trapping a known volume of powder inside the formed enclosure, or "cup". The sampled powder is weighed enabling the calculation of the powder packing density of the recoated powder bed, which is then compared to the *PD* of the simulated powder bed.

The validation experiment was repeated five times. Measures were taken to reduce and quantify error resulting from various stages of the process, and all the tested sources of error were negligible. Average powder packing density characterised in the validation experiment was 52 %, with a standard deviation of 0.2 %.

Input values for the simulation model were mostly characterised by rheometry, pycnometry, dynamic image analysis. Calibration experiments were not implemented as they are time consuming and unnecessary in this case; the powder was thoroughly characterised by the EOS Finland laboratory and any unknown parameters were available in literature.

The simulation model featured a building platform of about 6 mm x 1.5 mm size. Approximately 370 000 particles were generated in a dispenser, which was enough to recoat the powder bed four times, with the first layer being of double height. After four recoats, the simulation run ended and *PD* was measured with different methods and from both the full length of the powder bed, and at a recognised stable region. The combination most

representative of the validation experiment conditions was considered to be a measurement from the stable region using a measuring method where the sampling volume is partly embedded into the powder bed surface. With this method the simulated powder bed had a *PD* of 52 %, which was a match to validation.

With this work done, the original research questions can be answered;

- The chosen FLOW-3D DEM software can be used to build a realistic powder bed model which corresponds well to a validation experiment.
    - A variety of validation methods can be found in literature, but none were directly applicable. A purpose-built method was developed and tested.
- Dynamic image analysis, pycnometry, and rheometry can be used to define most input parameters. Some parameters such as coefficient of restitution or adhesion should be approximated from literature. Friction and adhesion can also be estimated via calibration experiments, but this was not found to be necessary in this case, since rheometry provided a good approximation of friction, and adhesion was ignored.
- The simulation runtime was about three days, which may not be competitive compared to conventional testing. However, this method avoids the purchase of physical powder for testing. The amount of experimentation and knowledge building required to build the first model was significant, but it can mostly be applied for all future DEM models, making it a one-time investment. The important information, powder packing density, is easy to measure from the simulation results. Particle movement during recoating and packing behaviour can easily be observed from the simulation, which is interesting for powder feedstock development and difficult or impossible to observe in situ. Overall, the simulation model shows high promise for reducing the expense of powder feedstock development.

11.1 Future work

The simulation model and validation method created in this thesis are intended for use as a platform for future development and expansion, and planning this future development is not within the scope of this thesis. However, there are many other interesting observations and areas of development which were not explored further in this thesis due to time constraints.

11.1.1 Part A: Validation

Some areas of optimisation for the validation sample were recognised. For example, the height of the built wall should be reduced as much as possible without making the clean-up or measuring process too difficult or prone to error. This would make the validation experiment more analogous to the shallow simulated powder bed. It may also be beneficial to increase the area of the sample in this case, to increase the sampled mass of powder, which should reduce the significance of small measurement errors.

It was found during the literature review of this thesis that *SR* and *PD* seem to correlate. The mechanics of this correlation could be explored with practical experiments.

11.1.2 Part B: Simulation

The effects of adhesion were not studied in this thesis, but in the future it may be of interest to develop a calibration experiment based on the literature review conducted in this thesis, and calibrate a fitting value for surface energy. Simulations with and without *SE* could be compared to see if it has a significant effect on *PD* or other phenomena of interest, and decide whether it will be included as a standard parameter in future simulations or not. The effects of surrounding atmosphere and material properties for solid geometry may also be worth exploring.

To speed up future iterations, it may be useful to fully investigate relationships between computation time and various parameters. The spring constant is known to affect computation time negatively, but e.g., increasing the fraction of fine particles in a PSD may have a similar effect based on observations made during this thesis.

To increase confidence in the simulation model, it may be of interest to compare the powder bed surface profiles of simulated and recoated powder beds with SEM or similar equipment. Some assumptions made in this thesis (such as that of the built walls being lower than the surface of the powder bed) could also be tested with this method.

Building the simulation model is iterative work. In a commercial application where simulations are run back-to-back for research and development purposes, artificial intelligence could be used for automating or optimising design of experiments. I.e., which parameters should be adjusted to affect some powder bed parameter, based on the results of the previous simulation run. Characterisation of the simulated powder bed can also be automated with scripts.

References

[1] I. Gibson, “Powder Bed Fusion,” in *Additive Manufacturing Technologies*, Cham, Springer, 2021, pp. 125-235.

[2] ISO/ASTM, “ISO/ASTM 52900:2021 Additive manufacturing — General principles — Fundamentals and vocabulary,” 11 2021. [Online]. Available: https://www.iso.org/standard/74514.html. [Accessed 29 09 2022].

[3] EOS GmbH, “Quality management and quality assurance,” EOS, 2022. [Online]. Available: https://www.eos.info/en/industrial-3d-printing/3d-printing-quality-assurance. [Accessed 29 09 2022].

[4] A. Kracke, “Superalloys, the most succesful alloy system of modern times - past, present and future,” in *7th international symposium on superalloy 718 and derivatives*, Pittsburgh, 2010.

[5] M. Kirka, A. Plotkowski, P. Nandwana, A. Chaudhary, S. Baby and R. Dehoff, “Progress in the processing and understanding of Alloy 718 fabricated through powder bed additive manufacturing processes,” in *9th international symposium on superalloy 718 & derivatives: energy, aerospace, and industrial applications*, Pittsburgh, 2018.

[6] A. Müller, G. Schlick, R. Neu, C. Anstätt, T. Klimkait, J. Lee, B. Pascher, M. Schmitt and C. Seidel, “Additive manufacturing of pure tungsten by means of selective laser beam melting with substrate preheating temperatures up to 1000 ∘,” *Nuclear materials and energy,* vol. 19, pp. 184-188, 2019.

[7] I. Anderson, E. White and R. Dehoff, “Feedstock powder processing research needs for additive manufacturing development,” *Current opinion in solid state and materials science,* vol. 22, pp. 8-15, 2018.

[8] S. Farzadfar, M. Murtagh and N. Venugopal, “Impact of IN718 bimodal powder size distribution on the performance and productivity of laser powder bed fusion additive manufacturing process,” *Powder technology,* vol. 375, pp. 60-80, 2020.

[9] A. Averardi, C. Cola, S. Zeltmann and N. Gupta, “Effect of particle size distribution on the packing of powder beds: A critical discussion relevant to additive manufacturing,” *Materials today communications,* vol. 24, p. 100964, 2020.

[10] ISO, “ISO/ASTM 52907:2019 Additive manufacturing — Feedstock materials — Methods to characterize metal powders,” 11 2019. [Online]. Available: https://www.iso.org/standard/73565.html. [Accessed 26 04 2022].

[11] J. Dawes, R. Bowerman and R. Trepleton, “Introduction to the Additive Manufacturing Powder Metallurgy Supply Chain,” *Johnoson Matthey technology review,* vol. 59, no. 3, pp. 243-256, 2015.

[12] J. Tan, W. Wong and K. Dalgarno, “An overview of powder granulometry on feedstock and part performance in the selective laser melting process,” *Additive manufacturing,* vol. 18, pp. 228-255, 2017.

[13] J. Dunkley, “Metal Powder Atomisation Methods for Modern Manufacturing,” *Johnson Matthey technology review,* vol. 63, no. 3, pp. 226-232, 2019.

[14] E. Hryha and D. Riabov, “Metal powder production for additive manufacturing,” in *Encyclopedia of materials: metals and alloys, volume 3*, Gothenburg, Elsevier Science Publishing Co Inc, 2022, pp. 264-271.

[15] G. Chen, “Forming metal powders by electrolysis,” in *Advances in powder metallurgy*, Cambridge, Woodhead Publishing, 2013, pp. 19-41.

[16] P. Desai, A. Mehta, P. Dougherty and C. Higgs, “A rheometry based calibration of a first-order DEM model to generate virtual avatars of metal Additive Manufacturing (AM) powders,” *Powder technology,* Vols. 441-456, p. 342, 2019.

[17] J. Clayton, D. Millington-Smith and B. Armstrong, “The Application of Powder Rheology in Additive Manufacturing,” *JOM,* vol. 67, no. 3, pp. 544-548, 2015.

[18] ASTM, “Standard Test Methods for Flow Rate of Metal Powders Using the Hall Flowmeter Funnel,” 07 04 2020. [Online]. Available: https://www.astm.org/b0213-20.html. [Accessed 02 09 2020].

[19] C. Vakifahmetoglu, B. Hasdemir and L. Biasetto, “Spreadability of Metal Powders for Laser-Powder Bed Fusion via Simple Image Processing Steps,” *Materials,* vol. 15, p. 205, 2022.

[20] A. Spierings, M. Voegtlin, T. Bauer and K. Wegener, “Powder flowability characterisation methodology for powder-bed based metal additive manufacturing,” *Progress in additive manufacturing,* vol. 1, pp. 9-20, 2016.

[21] S. Geer, M. Bernhardt-Barry, E. Garboczi, J. Whiting and A. Donmez, “A more efficient method for calibrating discrete element method parametres for simulations of metallic powders used in additive manufacturing,” *Granular matter,* vol. 77, pp. 20-37, 2018.

[22] H. Sehhat and A. Mahdianikhotbesara, “Powder spreading in laser-powder bed fusion process,” *Granular matter,* vol. 23, p. 89, 2021.

[23] H. Chen, Q. Wei, S. Wen, Z. Li and Y. Shi, “Flow behavior of powder particles in layering process of selective laser melting: Numerical modeling and experimental verification based on

discrete element method," *International journal of machine tools and manufacture,* vol. 123, pp. 146-159, 2017.

[24] M. Balbaa, A. Ghasemi, E. Fereiduni, M. Elbestawi, S. Jadhav and J. Kruth, "Role of powder particle size on laser powder bed fusion processability of AlSi10mg alloy," *Additive manufacturing,* vol. 37, p. 101630, 2021.

[25] Q. Nguyen, M. Nai, Z. Zhu, C. Sun, J. Wei and W. Zhou, "Characteristics of Inconel Powders for Powder-Bed Additive Manufacturing," *Engineering,* vol. 3, 2017.

[26] A. Sutton, C. Kriewall, M. Leu and J. Newkirk, "Powder characterisation techniques and effects of powder characteristics on part properties in powder-bed fusion processes," *Virtual and physical prototyping,* vol. 12, no. 1, pp. 3-29, 2017.

[27] C. K. Chua, C. H. Wong and W. Y. Yeong, "Material characterization for additive manufacturing," in *Standards, Quality Control, and Measurement Sciences in 3D Printing and Additive Manufacturing*, London, Academic Press, 2017, pp. 95-137.

[28] ASTM, "Standard Test Method for Apparent Density of Free-Flowing Metal Powders Using the Hall Flowmeter Funnel," 10 09 2012. [Online]. Available: https://www.astm.org/b0212-09.html. [Accessed 1 8 2022].

[29] ASTM, "Standard Test Method for Determination of Tap Density of Metallic Powders and Compounds," 11 08 2014. [Online]. Available: https://www.astm.org/b0527-06.html. [Accessed 1 8 2022].

[30] S. Vock, B. Klöden, A. Kirchner, T. Weißgärber and B. Kieback, "Powders for powder bed fusion: a review," *Progress in additive manufacturing,* vol. 4, pp. 383-397, 2019.

[31] P. Kuznetsov, I. Shakirov, A. Zukov and V. S. M. Bobyr, "Effect of particle size distribution on the structure and mechanical properties in the process of laser powder bed fusion," in *Journal of physics: conference series 1758*, Suzdal, 2021.

[32] L. Haferkamp, S. Liechti, A. Spierings and K. Wegener, "Efect of bimodal powder blends on part density and melt pool fuctuation in laser powder bed fusion," *Additive manufacturing,* vol. 6, pp. 407-416, 2021.

[33] P. Avrampos and G.-C. Vosniakos, "A review of powder deposition in additive manufacturing by powder bed fusion," *Journal of manufacturing processes,* vol. 74, pp. 332-352, 2022.

[34] A. Spierings, N. Herres and G. Levy, "Influence of the particle size distribution on surface quality and mechanical properties in AM steel parts," *Rapid prototyping journal,* vol. 17, no. 3, pp. 195-202, 2011.

[35] S. Weaver, J. Whiting, V. Tondare, C. Beauchamp, M. Peltz, J. Tarr, T. Phan and A. Donmez, "The effects of particle size distribution on the rheological properties of the powder and the

mechanical properties of additively manufactured 17-4 PH stainless stteel," *Additive manufacturing,* vol. 39, 2021.

[36] B. Zhang, S. X. J. Liu, Y. Chen and Y. Tang, "Investigation of the experiment and simulation on TiH2 powder packing by a novel irregular 3D model," *Materials research express,* vol. 8, no. 2, p. 026510, 2021.

[37] R. Iacocca, "Surfce area, density, and porosity of powders," in *ASM Handbook Volume 7: Powder metal technologies and applications*, Materials Park, ASM International, 1998, p. 274.

[38] S. Yim, H. Bian, Aoyagi, K. Yamanaka and A. Chiba, "Spreading behavior of Ti–48Al–2Cr–2Nb powders in powder bed fusion additive manufacturing process: Experimental and discrete element method study," *Additive Manufacturing,* vol. 49, 2022.

[39] A. Rogalsky, I. Rishmawi, L. Brock and M. Vlasea, "Low cost irregular feed stock for laser powder bed fusion," *Journal of manufacturing processes,* vol. 35, pp. 446-456, 2018.

[40] ASTM, "Standard Test Method for Metal Powder Skeletal Density by Helium or Nitrogen Pycnometry," 07 04 2022. [Online]. Available: https://www.astm.org/b0923-22.html. [Accessed 06 10 2022].

[41] H. Chen, T. Cheng, Z. Li, Q. Wei and W. Yan, "Is high-speed powder spreading really unfavourable for the part quality of laser powder bed fusion additive manufacturing?," *Acta materialia,* vol. 231, 2022.

[42] A. Mussatto, R. Groarke, A. O'Neill, M. Obeidi, Y. Delarure and D. Brabazon, "Influences of powder morphology and spreading parameters on the powderbed topography uniformity in powder bed fusion metal additive manufacturing," *Additive manufacturing,* vol. 38, 2021.

[43] J. Oliveira, A. LaLonde and J. Ma, "Processing parameters in laser powder bed fusion metal additive manufacturing," *Materials and design,* vol. 193, 2020.

[44] S. Sanchez, P. Smith, Z. Xu, G. Gaspard, C. Hyde, W. Wits, I. Ashcroft, H. Chen and A. Clare, "Powder Bed Fusion of nickel-based superalloys: A review," *International journal of machine tools and manufacture,* vol. 165, 2021.

[45] M. Gor, H. Soni, V. Wankhede, P. Sahlot, K. Grzelak, I. Szachgluchowicz and J. Kluczynski, "A Critical Review on Effect of Process Parameters on Mechanical and Microstructural Properties of Powder-Bed Fusion Additive Manufacturing of SS316L," *Materials,* vol. 14, 2021.

[46] J. Choi, G. Shin, H. Lee, D. Yang, S. Yang, C. Lee, M. Brochu and J. Yu, "Evaluation of Powder Layer Density for the Selective Laser Melting (SLM) Process," *Materials transactions,* vol. 58, no. 2, pp. 294-297, 2017.

[47] R. Penny, P. Praegla, M. Ochsenius, D. Oropeza, R. Weissbach, C. Meier, W. Wall and J. Hart, "Spatial mapping of powder layer density for metal additive manufacturing via transmission X-ray imaging," *Additive manufacturing,* vol. 46, 2021.

[48] F. Sillani, R. Schiegg, M. Schmid, E. MAcDonald and K. Wegener, "Powder Surface Roughness as Proxy for Bed Density in Powder Bed Fusion of Polymers," *Polymers,* vol. 14, 2022.

[49] H. Chen, Y. Chen, Y. Liu, Q. Wei, Y. Shi and W. Yan, "Packing quality of powder layer during counter-rolling-type powder spreading process in additive manufacturing," *International journal of machine tools and manufacture,* vol. 153, p. 103553, 2020.

[50] H. Chen, Q. Wei, Y. Zhang, F. Chen, Y. Shi and W. Yan, "Powder-spreading mechanisms in powder-bed-based additive manufacturing: Experiments and computational modeling," *Acta materialia,* vol. 179, pp. 158-171, 2019.

[51] L. Cordova, T. Bor, M. Smit, M. Campos and T. Tinga, "Measuring the spreadability of pre-treated and moisturized powders for laser powder bed fusion," *Additive manufacturing,* vol. 32, p. 101082, 2020.

[52] S. Wu, Z. Lei, M. Jiang, J. Liang, B. Li and Y. Chen, "Experimental investigation and discrete element modeling for particle-scale powder spreading dynamics in powder-bed-fusion-based additive manufacturing," *Powder technology,* vol. 403, 2022.

[53] G. Jacob, A. Donmez, J. Slotwinski and S. Moylan, "Measurement of powder bed density in powder bed fusion additive manufacturing processes," *Measurement science and technology,* vol. 27, 2016.

[54] C. Boley, S. Khairallah and A. Rubenchik, "Calculation of laser absorption by metal," in *Additive Manufacturing Handbook - Product Development for the Defense Industry*, Boca Raton, CRC Press, 2017, pp. 507-518.

[55] T. Abu-Lebdeh, R. Damptey, V. Lamberti and S. Hamoush, "Powder packing density and its impact on SLM-based additive manufacturing," in *TMS 2019 148th Annual Meeting & Exhibition Supplemental Proceedings*, Pittsburgh, 2019.

[56] V. Lampitella, M. Trofa, A. Astarita and G. D'Avino, "Spreading of Powders in Powder Bed Additive Manufacturing: an Experimental Approach," in *ESAFORM*, Liége, 2021.

[57] A. Elliott, P. Nandwana, D. Siddel and B. Compton, "A Method for Measuring Powder Bed Density in Binder Jet Additive Manufacturing Process and the Powder Feedstock Characteristics Influencing the Powder Bed Density," in *Proceedings of the 27th Annual International Solid Freeform Fabrication Symposium*, Austin, 2016.

[58] J. Oh, S. Nahm, B. Kim and H. Choi, “Anisotropy in Green Body Bending Strength due to Additive Direction in the Binder-Jetting Additive Manufacturing Process,” *Korean journal of metals and materials,* vol. 57, no. 4, pp. 227-235, 2019.

[59] B. L, R. Wildman, C. Tuck, I. Ashcroft and R. Hague, “Investigation the effect of particle size distribution on processing parameters optimisation in selective laser melting process,” in *22nd annual international solid freeform fabrication symposium*, Austin, 2011.

[60] U. Ali, Y. Mahmoodkhani, S. Shahabad, R. Esmaeilizadeh, F. Liravi, E. Sheydaeian, K. Huang, E. Marzanbanrad, M. Vlasea and E. Toyserkani, “On the measurement of relative powder-bed compaction density in powder-bed additive manufacturing processes,” *Materials and design,* vol. 155, pp. 495-501, 2018.

[61] J. Li, G. Gao, S. Zhang and Y. Du, “Calibration and Measurement Study on Density of Selective Laser Sintered 3D Printing Powder Bed,” in *Journal of physics: conference series*, 2019.

[62] T. Wischeropp, C. Emmelmann, M. Brandt and A. Pateras, “Measurement of actual powder layer height and packing density in a single layer in selective laser melting,” *Additive manufacturing,* vol. 28, pp. 176-183, 2019.

[63] P. Cundall and O. Strack, “A discrete numerical model for granular assemblies,” *Géotechnique,* vol. 29, no. 1, pp. 47-65, 1979.

[64] M. Marigo and E. Stitt, “Discrete Element Method (DEM) for Industrial Applications: Comments on Calibration and Validation for the Modelling of Cylindrical Pellets,” *KONA Powder and particle journal,* vol. 32, pp. 236-252, 2015.

[65] P. Cleary, “DEM prediction of industrial and geophysical particle flows,” *Particuology,* vol. 8, pp. 106-118, 2010.

[66] C. Coetzee, “Review: Calibration of the discrete element method,” *Powder technology,* vol. 310, pp. 104-142, 2017.

[67] E. Parteli and T. Pöschel, “Particle-based simulation of powder application in additive manufacturing,” *Powder technology,* vol. 288, pp. 96-102, 2016.

[68] A. Di Renzo and F. Maio, “Comparison of contact-force models for the simulation of collisions in DEM-based granular fow codes,” *Chemical engineering science,* vol. 59, pp. 525-541, 2004.

[69] J. Rojek, “Contact Modeling in the Discrete,” in *Contact Modeling for Solids and Particles*, Cham, Springer International Publishing AG, 2018, pp. 177-228.

[70] Y. Lee, P. Nandwana and W. Zhang, “Dynamic simulation of powder packing structure for powder bed additive manufacturing,” *International journal of advanced manufacturing technology,* vol. 96, pp. 1507-1520, 2018.

[71] Flow Science, “FLOW-3D AM & FLOW-3D WELD Training,” 2022. [Online]. Available: https://users.flow3d.com/. [Accessed 08 09 2022].

[72] Flow Science Inc, *FLOW-3D User Manual,* 2020.

[73] M. Khorasani, A. Ghasemi, M. Leary, W. O'Neil, I. Gibson, L. Cordova and B. Rolfe, “Numerical and analytical investigation on meltpool temperature of laser-based powder bed fusion of IN718,” *International journal of heat and mass transfer,* vol. 177, 2021.

[74] T. Zohdi, “PART II—Discrete Element Method (DEM) Approaches: Dynamic Powder Deposition,” in *modeling and simulation of functionalised materials for additive manufacturing and 3D printing- continous and discrete media*, Cham, Springer International Publishing AG, 2018, pp. 83-119.

[75] P. Böhling, “Modeling of non-spherical particles in the Discrete Element Method (DEM) simulations,” Technischen Universität Graz, Graz, 2014.

[76] K. Marchais, J. Girardot, C. Metton and I. Iordanoff, “A 3D DEM simulation to study the influence of material and process parameters on spreading of metallic powder in additive manufacturing,” *Computational particle mechanics,* vol. 8, pp. 943-953, 2021.

[77] C. Meier, R. Weissbach, J. Weinberg, W. Wall and J. Hart, “Modeling and characterization of cohesion in fine metal powders with a focus on additive manufacturing process simulations,” *Powder technology,* vol. 343, pp. 855-866, 2019.

[78] V. Ganesan, A. Amerinatanzi and A. Jain, “Discrete Element Modeling (DEM) simulations of powder bed densification using horizontal compactors in metal additive manufacturing,” *Powder technology,* vol. 405, 2022.

[79] M. Shaheen, A. Thornton, S. Luding and T. Weinhart, “The influence of material and process parameters on powder spreading in additive manufacturing,” *Powder technology,* vol. 383, pp. 564-583, 2021.

[80] L. Dai, Y. Chan, G. Vastola, N. Khan, S. Raghavan and Y. Zhang, “Characterizing the intrinsic properties of powder – A combined discrete element analysis and Hall flowmeter testing study,” *Advanced powder technology,* vol. 32, pp. 80-87, 2021.

[81] L. Dai, V. Sorkin, G. Vastola and Y. Zhang, “Dynamics calibration of particle sandpile packing characteristics via discrete element method,” *Powder technology,* vol. 347, pp. 220-226, 2019.

[82] Y. Lee and W. Zhang, “Modeling of heat transfer, fluid flow and solidification microstructure of nickel-base superalloy fabricated by laser powder bed fusion,” *Additive manufacturing,* vol. 12, pp. 178-188, 2016.

[83] L. Wang, E. Li, H. Shen, R. Zou, A. Yu and Z. Zhou, “Adhesion effects on spreading of metal powders in selective laser melting,” *Powder technology,* vol. 363, pp. 602-610, 2020.

[84] Q. Han, H. Gu and R. Setchi, “Discrete element simulation of powder layer thickness in laser additive manufacturing,” *Powder technology,* vol. 352, pp. 91-102, 2019.

[85] D. Yao, X. Liu, J. Wang, W. Fan, H. Fu, H. Zhang, X. Yang, Q. Zou and X. An, “Numerical insights on the spreading of practical 316 L stainless steel powder in SLM additive manufacturing,” *Powder technology,* vol. 390, pp. 197-208, 2021.

[86] Z. Xiang, M. Zhang, R. Yan, R. Yin, Q. Yin and K. Zhang, “Powder-spreading dynamics and packing quality improvement for laser powder bed fusion additive manufacturing,” *Powder technology,* vol. 389, pp. 278-291, 2021.

[87] Y. Tian, L. Yang, D. Zhao, Y. Huang and J. Pan, “Numerical analysis of powder bed generation and single track forming for selective laser melting of SS316L stainless steel,” *Journal of manufacturing processes,* Vols. 964-974, p. 58, 2020.

[88] J. Steuben, J. Michopoulos and A. Iliopoulos, “Discrete Element Modeling of particle-based additive manufacturing processes,” *Computer methods in applied mechanics and engineering,* vol. 305, pp. 537-561, 2016.

[89] X. Li, P. Dunn and R. Brach, “Experimental and numerical studies on the normal impact pf microspheres with surfaces,” *Journal of aerosol sciences,* vol. 30, no. 4, pp. 439-449, 1999.

[90] A. Phua, C. Doblin, P. Owen, C. Davies and G. Delaney, “The effect of recoater geometry and speed on granular convection and size segregation in powder bed fusion,” *Powder technology,* vol. 394, pp. 632-644, 2021.

[91] Y. Fouda and A. Bayly, “A DEM study of powder spreading in additive layer manufacturing,” *Granular matter,* vol. 22, no. 10, 2020.

[92] Y. He, J. Gardy, A. Hassanpour and A. Bayly, “A digital-based approach for characterising spread powder layer in additive manufacturing,” *Materials & design,* vol. 196, 2020.

[93] C. Meier, R. Weissbach, J. Weinberg, W. Wall and J. Hart, “Critical influences of particle size and adhesion on the powder layer uniformity in metal additive manufacturing,” *Journal of materials processing technology,* vol. 266, pp. 484-501, 2019.

[94] M. Marinack, R. Musgrave and F. Higgs, “Experimental Investigations on the Coefficient of Restitution of Single Particles,” *Tribology transactions,* vol. 56, no. 4, pp. 572-580, 2013.

[95] P. Tolias, S. Ratynskaia, A. Shalpegin, L. Vignitchouk, F. Brochard, M. De Angeli and H. van der Meiden, “Experimental validation of the analytical model for tungsten dust - wall mechanical impacts incorporated in the MIGRAINe dust dynamics code,” *Nuclear materials and energy,* vol. 12, pp. 524-529, 2017.

[96] S. Ratynskaia, P. Tolias, A. Shalpegin, L. Vignitchouk, M. Angeli, I. Bykov, K. Bystrov, S. Bardin, F. Brochard, D. Ripamonti, N. den Harder and G. De Temmermann, “Elastic–plastic

adhesive impacts of tungsten dust with metal surfaces in plasma environments," *Journal of nuclear materials,* vol. 463, pp. 877-880, 2015.

[97] J. Wagner, "The Frictional Behavior of Tungsten and Molybdenum Powders Sliding on Die Materials," *Powder technology,* vol. 35, pp. 47-50, 1983.

[98] H. Abbasfard, G. Evans and R. Moreno-Atanasio, "Effect of van der Waals force cut-off distance on adhesive collision parameters in DEM simulation," *Powder technology,* vol. 299, pp. 9-18, 2016.

[99] C. Wensrich and A. Katterfield, "Rolling friction as a technique for modelling particle shape in DEM," *Powder technology,* vol. 217, pp. 409-417, 2012.

[100] C. Richter, T. Rößler, G. Kunze, A. Katterfield and F. Will, "Development of a standard calibration procedure for the DEM parameters of cohesionless bulk materials – Part II: Efficient optimization-based calibration," *Powder technology,* vol. 360, pp. 967-976, 2020.

[101] A. Grima and P. Wypych, "Development and validation of calibration methods for discrete element modelling," *Granular matter,* vol. 13, pp. 127-132, 2011.

[102] T. Roessler, C. Richter, A. Katterfield and F. Will, "Development of a standard calibration procedure for the DEM parameters of cohesionless bulk materials – part I: Solving the problem of ambiguous parameter combinations," *Powder technology,* vol. 343, pp. 803-812, 2019.

[103] J. Zhang, Y. Tan, T. Bao, Y. Xu, X. Xiao and S. Jiang, "Discrete Element Simulation of the Effect of Roller-Spreading Parameters on Powder-Bed Density in Additive Manufacturing," *Materials,* vol. 13, p. 2285, 2020.

[104] L. Si, T. Zhang, M. Zhou, L. Maoyuan and H. Zhou, "Numerical simulation of the flow behavior and powder spreading mechanism in powder bed-based additive manufacturing," *Powder technology,* vol. 394, pp. 1004-1016, 2021.

[105] L. Cao, "Study on the numerical simulation of laying powder for the selective laser melting process," *The International Journal of Advanced Manufacturing Technology,* vol. 105, pp. 2253-2269, 2019.

[106] Y. Zhao, Y. Koizumi, K. Aoyagi, K. Yamanaka and A. Chiba, "Characterization of powder bed generation in electron beam additive manufacturing by discrete element method (DEM)," in *Materials today: Proceedings 4*, 2016.

[107] L. Liu, M. Huang, Y. Ma, M. Qin and T. Liu, "Simulation of Powder Packing and Thermo-Fluid Dynamic of 316L Stainless Steel by Selective Laser Melting," *Journal of materials engineering and performance,* vol. 29, pp. 7369-7381, 2020.

[108] X. Gao, G. Faria, W. Zhang and K. Wheeler, “Numerical analysis of non-spherical particle effect on molten pool dynamics in laser-powder bed fusion additive manufacturing,” *Computational materials science,* vol. 179, 2020.

[109] EOS GmbH, “EOS NickelAlloy IN718 Material data sheet,” 09 2022. [Online]. Available: https://www.eos.info/en/additive-manufacturing/3d-printing-metal/dmls-metal-materials/nickel-alloys. [Accessed 14 10 2022].

[110] C. Rock, C. Ledford, M. Garcia-Avila, H. West, V. Miller, M. Pankow, R. Dehoff and T. Horn, “The influence of powder reuse on the properties of nickel super alloy ATI 718 in laser powder bed fusion additive manufacturing,” *Metallurgical and material transactions B,* vol. 52, pp. 676-688, 2021.

[111] B. Hann, “Powder Reuse and Its Effects on Laser Based Powder Fusion additive manufactured Alloy 718,” *SAE international journal of aerospace,* vol. 9, no. 2, pp. 209-213, 2016.

[112] L. Cordova, M. Campos and T. Tinga, “Revealing the Effects of Powder Reuse for Selective Laser Melting by Powder Characterization,” *JOM,* vol. 71, no. 3, pp. 1062-1072, 2019.

[113] ISO, “ISO 13322-2:2006 Particle size analysis — Image analysis methods — Part 2: Dynamic image analysis methods,” 11 2006. [Online]. Available: https://www.iso.org/standard/38665.html. [Accessed 14 10 2022].

[114] ASTM, “ASTM B212-21 Standard Test Method for Apparent Density of Free-Flowing Metal Powders Using the Hall Flowmeter Funnel,” 15 09 2021. [Online]. Available: https://www.astm.org/b0212-21.html. [Accessed 14 10 2022].

[115] ASTM, “D7891-15 Standard Test Method for Shear Testing of Powders Using the Freeman Technology FT4 Powder Rheometer Shear Cell,” 27 12 2016. [Online]. Available: https://www.astm.org/d7891-15.html. [Accessed 06 10 2022].

[116] A. Jenike, Storage and flow of solids, Salt Lake City: University of Utah, 1964.

[117] H. Wang, C. Zheng, P. Zou, S. Yang, L. Hu and B. Wei, “Density determination and simulation of Inconel 718 alloy at normal and metastable liquid states,” *Journal of materials science and technology,* vol. 34, pp. 436-439, 2018.

[118] Flow Science, “Flow-3D,” Flow Science Inc., [Online]. Available: https://www.flow3d.com/products/flow-3d/. [Accessed 29 07 2022].

[119] Dassault Systémes, “Solidworks - Design/Engineering,” Dassault Systémes A.S., [Online]. Available: https://www.solidworks.com/domain/design-engineering#brick--5002--custom-text-condensed--en. [Accessed 27 07 2022].

[120] EOS, “EOSPRINT 2 - Data optimization and process management,” EOS GmbH, [Online]. Available: https://www.eos.info/en/additive-manufacturing/software-3d-printing/data-preparation-3d-printing. [Accessed 27 07 2022].

[121] EOS, “EOS M 290,” 06 2022. [Online]. Available: https://www.eos.info/03_system-related-assets/system-related-contents/_pdf_system-data-sheets/eos_system_data_sheet_eos_m_290_en.pdf. [Accessed 27 07 2022].

[122] Freeman Technology Ltd., “FT4 powder rheometer training presentation,” Freeman Technology, 2017.

[123] E. Santos, L. Carvalho, A. Mesquita, L. Gomes, K. Pinheiro and A. Mesquita, “Discrete element modeling of non-spherical particles using a spherical shape,” *International engineering journal,* vol. 73, no. 3, pp. 361-369, 2020.

[124] S. Haeri, Y. Wang, O. Ghita and J. Sun, “Discrete element simulation and experimental study of powder spreading process in additive manufacturing,” *Powder technology,* vol. 306, pp. 45-54, 2016.

[125] R. Iacocca, “Particle size and size distriution,” in *ASM Handbook Volume 7: Powder metal technologies and applications*, Materials Park, ASM International, 1998, pp. 234-236.

[126] V. Bhavar, S. Khot, P. P. V. Kattire, K. Gujar and R. Singh, “A review on powder bed fusion technology of metal additive manufacturing,” in *4th International conference and exhibition on Additive Manufacturing Technologies-AM-2014*, Banglore, 2014.

[127] P. Gokuldoss, S. Kolla and J. Eckert, “Additive Manufacturing Processes: Selective Laser Melting, Electron Beam Melting and Binder Jetting—Selection Guidelines,” *Materials,* vol. 10, no. 6, p. 672, 2017.

[128] C. Emmelmann, D. Herzog and J. Kranz, “Design for laser additive manufacturing,” in *Laser additive manufacturing - materials, design, technologies, and applications*, Duxford, Woodhead Publishing, 2017, pp. 259-279.

[129] C. Lindemann and U. Jahnke, “Modelling of laser additive manufactured product lifecycle costs,” in *Laser additive manufacturing - materials, design, technologies, and applications*, Duxford, Woodhead Publishing, 2017, pp. 281-316.

[130] ISO, “ISO/ASTM 52910:2018 Additive manufacturing — Design — Requirements, guidelines and recommendations,” 07 2018. [Online]. Available: https://www.iso.org/standard/67289.html. [Accessed 26 04 2022].

[131] ISO, “ISO/ASTM 52911-1:2019 Additive manufacturing — Design — Part 1: Laser-based powder bed fusion of metals,” 07 2019. [Online]. Available: https://www.iso.org/standard/72951.html. [Accessed 26 04 2022].

[132] M. Mehrpouya, A. Dehghanghadikolaei, B. Fotovvati, A. Vosooghnia, S. Emamiam and A. Gisario, “The Potential of Additive Manufacturing in the Smart Factory Industrial 4.0: A Review,” *Applied sciences,* vol. 9, p. 2865, 2019.

[133] I. Gibson, “Post-processing,” in *Additive manufacturing technologies*, Cham, Springer Nature Switzerland, 2021, pp. 457-489.

[134] EOS GmbH, “DMLS materials for additive manufacturing of metal parts - material overview,” 08 2022. [Online]. Available: https://www.eos.info/en/additive-manufacturing/3d-printing-metal/dmls-metal-materials. [Accessed 27 09 2022].

[135] E. Malekipour and H. El-Mounayri, “SCANNING STRATEGIES IN THE PBF PROCESS – A CRITICAL REVIEW,” in *ASME 2020 International mechanical engineering congress and exposition* , Portland, 2020.

[136] S. Sun, M. Brandt and M. Easton, “Powder bed fusion processes; an overview,” in *Laser Additive Manufacturing*, Duxford, Woodhead Publishing, 2017, pp. 55-77.

[137] B. Cheng, S. Shrestha and K. Chou, “Stress and deformation evaluations of scanning strategy effect in selective laser melting,” *Additive manufacturing,* vol. 12, pp. 240-251, 2016.

[138] J. Robinson, I. Ashton, P. Fox, E. Jones and C. Sutcliffe, “Determination of the effect of scan strategy on residual stress in laser powder bed fusion additive manufacturing,” *Additive manufacturing,* vol. 23, pp. 13-24, 2018.

[139] J. Robinson, I. Ashton, E. Jones, P. Fox and C. Sutcliffe, “The effect of hatch angle rotation on parts manufactured using selective laser melting,” *Rapid prototyping journal,* vol. 25, no. 2, pp. 289-298, 2019.

[140] J. Oliveira, T. Santos and R. Miranda, “Revisiting fundamental welding concepts to improve additive manufacturing: From theory to practice,” *Progress in material science,* vol. 107, p. 100590, 2020.

[141] F. Caiazzo, V. Alfieri and G. Casalino, “On the Relevance of Volumetric Energy Density in the Investigation of Inconel 718 Laser Powder Bed Fusion,” *Materials,* vol. 13, no. 3, 2020.

[142] W. Wang and S. Liang, “Prediction of molten pool height, contact angle, and balling occurrence in laser powder bed fusion,” *The international journal of advanced manufacturing technology,* vol. 119, pp. 6193-6202, 2022.

[143] H. Lee, C. Lim, M. Low, N. Tham, V. Murukeshan and Y.-J. Kim, “Lasers in Additive Manufacturing: A Review,” *International journal of precision engineering and manufacturing,* vol. 4, no. 3, pp. 307-322, 2017.

[144] S. Katayama, “Introduction: fundamentals of laser welding,” in *Handbook of Laser Welding Technologies*, Cambridge, Woodhead Publishing Ltd, 2013, pp. 1-15.

[145] S. Patel and M. Vlasea, “Melting modes in laser powder bed fusion,” *Materialia,* vol. 9, pp. 2589-1529, 2020.

[146] A. Aggarwal, S. Patel and A. Kumar, “Selective Laser Melting of 316L Stainless Steel: Physics of Melting Mode Transition and Its Influence on Microstructural and Mechanical Behavior,” *JOM,* vol. 71, pp. 1105-1116, 2019.

[147] X. Zhang, W. Chen, J. Ren, Y. H. G. Wang and H. Zhang, “Effects of processing parameters on mode and stability of laser welding,” in *Lasers as tools for manufacturing of durable goods and microelectronics*, San Jose, 1996.

[148] T. Le, X. Wang, K. Davidson, J. Fronda and M. Seita, “Experimental analysis of powder layer quality as a function of feedstock and recoating strategies,” *Additive manufacturing,* vol. 39, p. 101890, 2021.

[149] K. Yuasa, M. Tagami, M. Yonehara, T. Ikeshoji, K. Takeshita, A. H and H. Kyogoku, “Influences of powder characteristics and recoating conditions on surface morphology of powder bed in metal additive manufacturing,” *The International Journal of Advanced Manufacturing Technology,* vol. 115, pp. 3919-3932, 2021.

[150] H. Salehi, J. Cummins, E. Gallino, N. Harrison, A. Hasanpour and M. Bradley, “A new approach to quantify powder's bed surface roughness in additive manufacturing,” *Powder technology,* vol. 407, 2022.

Appendices

Appendix 1: Particle size characterisation

There are many methods of characterising the size of powder particles. The most common methods include sieving, laser diffraction, dynamic image analysis, and microscopy [125, 12]

- The sieving method is simple and capable of processing large sample sizes. Multiple sieves are stacked on top of each other, in decreasing order with the largest aperture sizes on top. Powder is poured on the top sieve and after powder flow through the sieves ends, the mass of powder is measured from each sieve. It is also common to vibrate or the sieves to promote particle dispersion on the sieve surface and "bounce" the particles so that they can land narrow side first onto the apertures. [12, 125]

- Laser diffraction is a common method for characterising powder size distributions. It works by passing particles in front of a laser beam and sensing the intensity and angle of the light diffracted from the particles. This data is processed by an algorithm to calculate the diameter of each particle. [12, 125]

- Dynamic image analysis is similar to laser diffraction in procedure, though instead of sensing diffracted light, the particles are imaged by cameras which use image processing to define particle size and shape. [12, 125]

- Measurement by microscopy is a relatively atypical method since it is inefficient if done manually, though automated machine vision can also be used to speed up the process. The upside is that the equipment is relatively common and multi-purpose, and the method can simultaneously yield both a numerical and a visual description on particle morphology. [12, 125]

It should be noted that the particle morphology can significantly affect the measured particle size. The size is expressed with diameters, but a precise diameter can only be measured from spherical particles; diameters measured from irregular particles using diffraction, image analysis, or microscopy, are the result of a mathematical model that defines a sphere-equivalent diameter for the irregular particle, and different models may yield different diameters for the same particle. Also, some measuring methods only measure the size of a random projection of the particle, while sieving usually measures the smallest projection of the particle that fits through the mesh apertures, excluding large aspect ratios. [125]

Appendix 2: Introduction to laser-based powder bed fusion

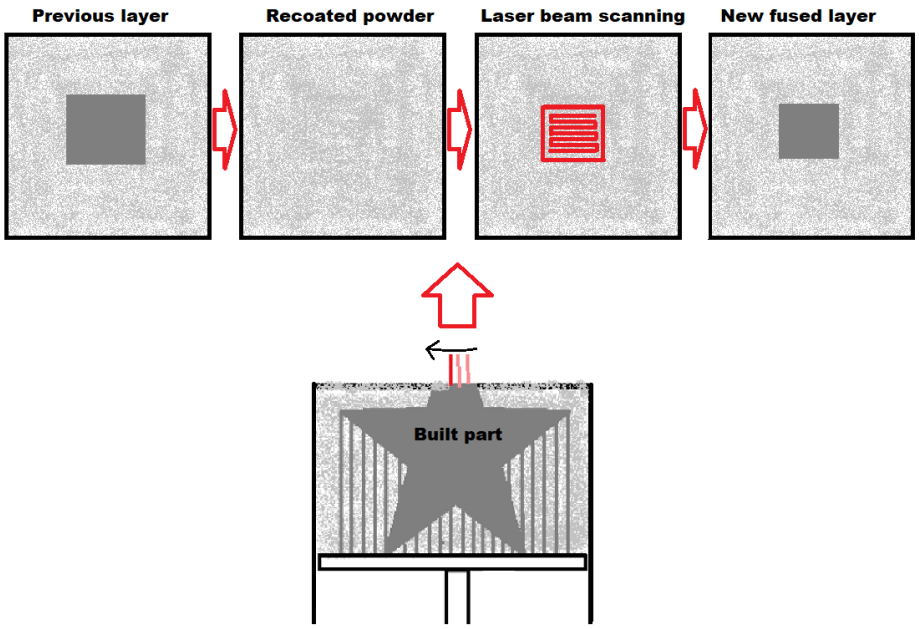

Figure 57 Top-down view of powder recoating and laser beam scanning.

As seen in Figure 57, the scanner "draws" the shape of the current layer of the built part, melting and fusing the powder onto the previously fused layer. The scanned shape is usually filled in as a hatch pattern, formed of individual straight vectors. This process is repeated until the part is completely built. [1, 126]

L-PBF process chain

L-PBF is a digital manufacturing technology where every build job starts from a digital 3D object, usually designed using computer-aided design (CAD) tools [1, 127]. However, the 3D model cannot be simply inputted as-is into the L-PBF machine – some pre-processing must be done, as demonstrated in Figure 58.

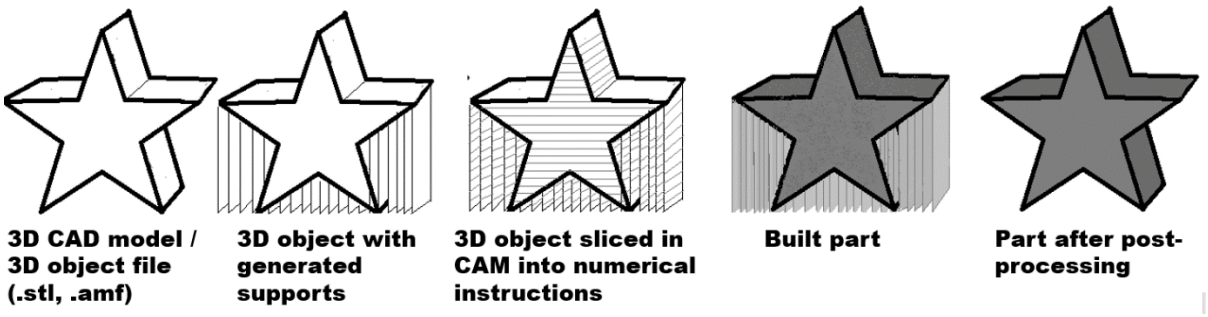

Figure 58 Phases of a part built with L-PBF; From a 3D model, to numerical instructions divided into "slices" or layers, to an as-built part, and finally a post-processed usable part.

As shown in Figure 58, The CAD file is converted into a universal 3D object file format, such as .stl or .amf, and transferred to computer-aided manufacturing (CAM) software that slices the 3D object into layers and translates it into numerical instructions for the L-PBF machine. This is also where necessary process parameters (e.g. layer height, scanning speed, power of the laser beam, etc.) are defined. [1] Also, 3rd party software is often used to generate support structures, compensate for heat-induced deformations, or otherwise adjust the model between CAD and CAM. Practically all functional parts produced by L-PBF need support structures to attach the part to the building platform and to dissipate heat more effectively and uniformly. A design for additive manufacturing (DfAM) approach to CAD work can reduce the need of supports drastically and improve the overall buildability of the part, compared to traditional design approaches based on subtractive machining. [1, 126, 128, 129] International standards ISO/ASTM 52910:2018 [130] and ISO/ASTM 52911-1:2019 [131] have been developed to unify design practices as well as to recognise the opportunities and limitations of the L-PBF process in part design.

Before the part can be built, the L-PBF system and powder feedstock must be prepared. Powder is sieved and loaded into the L-PBF system. The building platform plate must be machined to remove fused material from the previous build job, and inserted into the L-PBF system. The platform then needs to be levelled horizontally and the height calibrated to one layer height below the recoater blade. The build chamber is closed, and depending on the used powder material, the air inside is replaced with an inert gas and the building platform is pre-heated. When the correct process conditions are set, the building process can begin. [1, 129] After the part is built, some amount of post-processing is needed. The part must be sawed off the building platform, and as seen in Figure 58 the remaining support structures need to be detached.

Functional parts often need heat treatment, hot isostatic pressing, and/or surface machining to improve the mechanical properties of the parts. [132, 126, 133]

Powder bed forming and recoating

The powder bed in L-PBF is formed by spreading thin, <100 µm thick coats of powder on top of the building platform. This spreading is referred to as recoating. [1, 134] Different equipment manufacturers use their own variations of the process, but this thesis will be considering recoating as seen in the process called direct metal laser sintering (DMLS) used in the EOS M 290 system. A diagram of this process is presented in Figure 59.

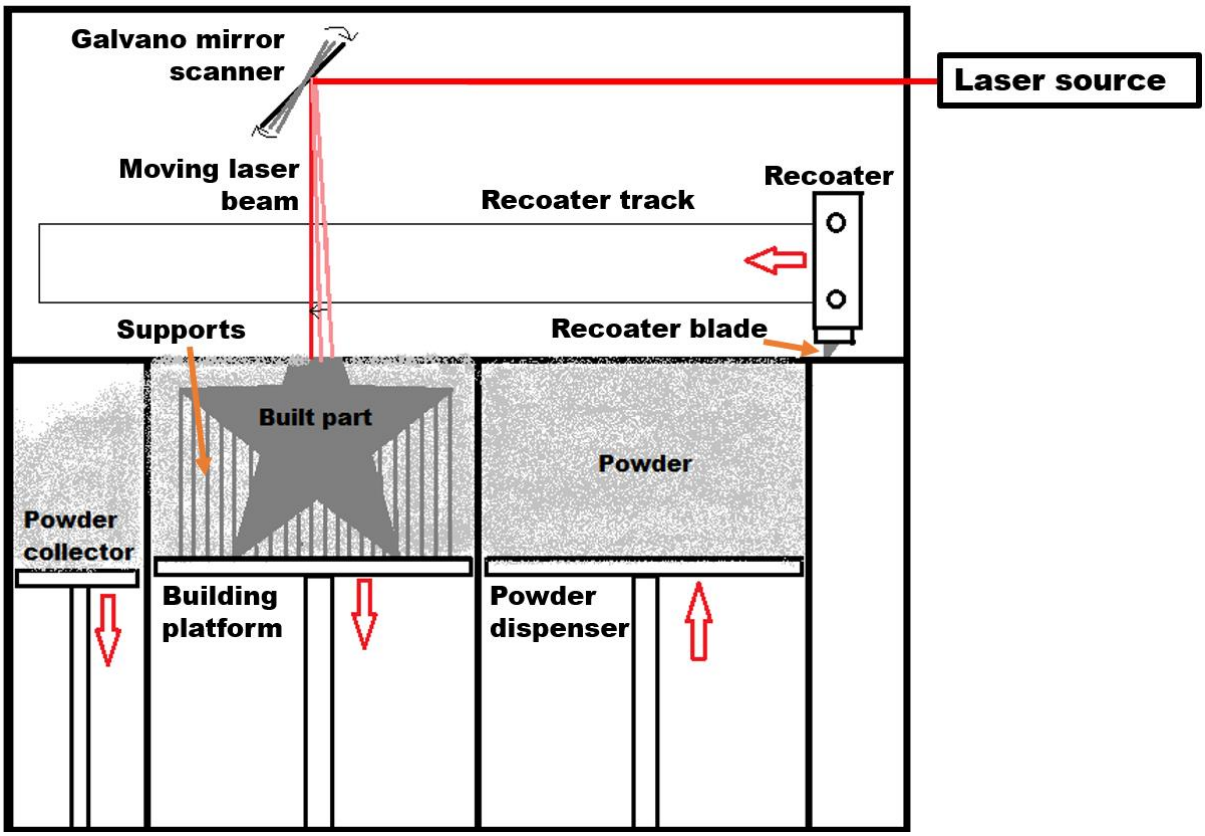

Figure 59 Simplified diagram of the operating principle of an EOS M 290 L-PBF system.

As seen in Figure 59, the system has three moving reservoirs of powder: the dispenser, the building platform, and the collector. The powder feedstock is initially loaded into the dispenser and levelled. The building platform is lowered by the height of one layer, and the dispenser is raised in inverse relation to the platform. Then, the recoater pushes the topmost layer of powder off the dispenser and deposits it on the building platform. Excess powder is pushed into the collector bin. [1, 126]

One of the most important recoating-related process parameters in L-PBF is the layer height h_l [µm]. Layer height refers to the thickness of each powder layer spread on the building platform by the recoater. Layer heights used in EOS processes, for example, range from 20-90 µm. Small h_l provides higher resolution in the vertical direction of the finished part, i.e. smaller features can be accurately built in a vertical direction. Using a too large layer height also has a risk of not fully fusing the layers to each other, though this maximum depends on other process parameters and the alloy used. On the other hand, using a small h_l will increase build times, as more recoats and laser beam exposures are needed. [134, 41, 22]

There is no such thing as "a perfect h_l", it should be optimised for the material, application and the type of product being built. If cost per part is critical, a higher h_l may be preferred to increase throughput of products, and a specialised part with detailed features or smooth surfaces may benefit from a lower h_l. [134, 41, 1] Equally important as choosing the correct layer height is the capability to build layers that match the planned h_l. As the powder packing density is much lower than the density of the melted and fused solid metal, the fused areas are much thinner than the powder layer, which has to be compensated for to reach the correct h_l. [41]

Another important recoating parameter is the movement velocity of the recoater during recoating. Multiple studies indicate that higher recoating velocities reduce the smoothness, true layer height accuracy, and density of the powder bed, both of which are unwanted for producing dimensionally accurate, strong, dense parts [33, 86, 90]. It is still attractive to use higher recoating velocities as this reduces build time. In addition, in a study by Chen et al. (2022) [41] it was found that the total negative effect of increased recoating velocity to the mechanical properties of finished parts is actually very small, the greatest drawback being reduced dimensional accuracy of the finished part.

Laser-material interaction

Once the powder bed is recoated, the part is exposed to a laser beam via a scanner. The laser beam scans, or "draws", the shape of the current layer, melting and fusing the powder layer into a layer of solid metal.

The scanner is a set of mirrors that are tilted extremely quickly and precisely using a galvanometer, according to the numerical instructions provided the CAM software. Moving the

mirrors moves the point of impact of the laser beam on the powder bed, allowing for extremely precise control of the melted and fused areas. [1]

Scanning can be done with different patterns or strategies, but commonly the outer edge of the part layer is scanned at least once (this edge-following path is called a contour) and the rest of the space is scanned fully with a hatching pattern. [1, 135] Hatching can be done e.g. by filling the area in small separately hatched squares, or by longer lines from one edge of the layer to the other. The distance between each hatch vector, called hatch distance, can be varied as well. Typically, the pattern is rotated for every layer in order to reduce isotropy in mechanical properties of the finished part. [135] The top and bottom surfaces of the part are called up-skin and down-skin respectively. Contours, hatches, and up- or down-skins may be scanned with different laser powers and scanning speeds, as there may be, for example, different surface finish requirements for the top, bottom, or vertical surfaces of the part. The pinpoint heat delivered by the laser beam on the otherwise "cool" part creates a significant thermal gradient, which, as it rapidly cools, leaves residual stress into the part. Residual stress can cause cracking, distortions and even delamination of layers, which may ruin the entire finished part. [1, 136, 135]

The prevalent understanding is that the largest portion of residual stresses in L-PBF produced parts are stresses created parallel along the scanning path. Therefore long scan paths are considered to produce higher residual stresses, which has led many authors to investigate the possibility to reduce stresses in finished parts by optimising scanning strategies with shorter or less unidirectional paths for example. [135] Multiple studies with both simulation and practical experiments have found minimal improvement or even contradicting effects in mechanical performance, residual stresses, or deformation by angling, alternating, 2,5 mm checkerboarding, or spiralling the hatch pattern as opposed to regular square-filling hatching. [137, 138, 139]

Theoretically the highest possible scanning speed should be used to minimise build times. It is not so simple in practice, however. Depending on the material, high scanning speeds may degrade surface quality or mechanical properties. [140] In addition, increased scanning speed will reduce the density of thermal energy transferred to the powder from the laser beam. This is called volumetric energy density or *VED* [J/mm^3], which can be calculated using Equation (9 where laser beam power is P [W], scanning velocity is v_s [m/s], layer height is h_l [µm], and hatch distance is d_h [mm]. [141]

$$VED = \frac{P}{h_l * v_s * d_h * 1000} \quad (9)$$

Each powder material has its own range of optimal *VED* values (depending on the thermal properties and absorptivity of the material) which will result in successfully built parts. In theory, if *VED* is unchanged, the powder should melt and fuse similarly regardless of the values of individual parameters. This is not the case in reality, due to the mechanics of powder interacting with the laser beam, as shown in Figure 60, adapted from Oliveira et al. (2020) [43].

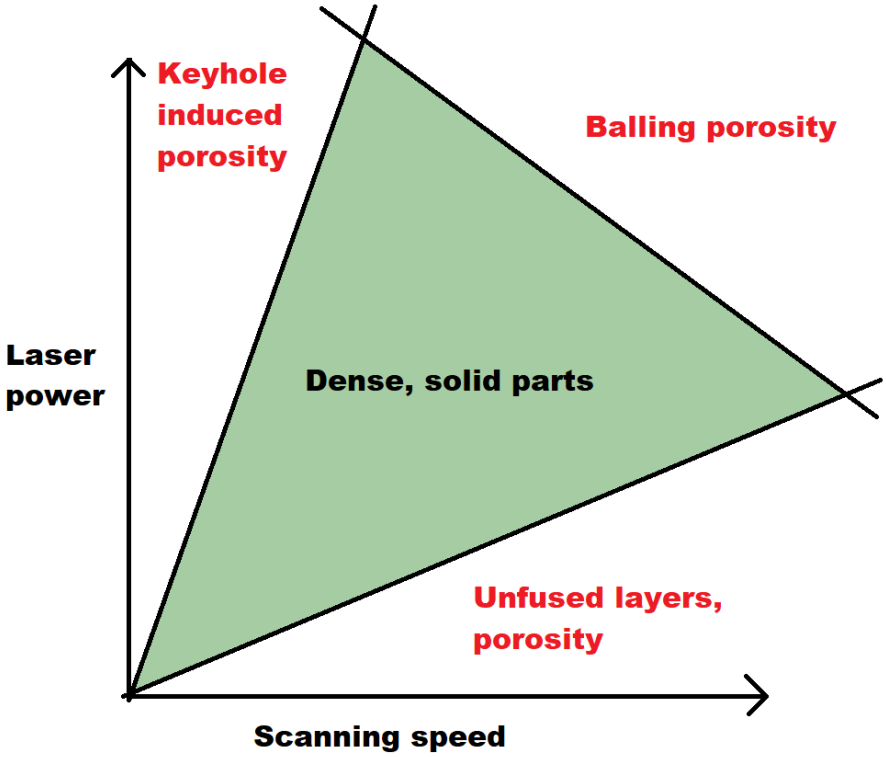

Figure 60 Illustration of the zone where dense parts can be produced as a function of scanning speed and laser power.

In the green area of Figure 60 is the zone where fully dense parts can be produced. Here, the powder is being melted in conduction mode, which means the powder is melted into a shallow U-shaped meltpool which slightly re-melts the underlying solid metal, fusing the new layer to the previous layer. Very high laser power will cause to meltpool to deepen uncontrollably into a so-called keyhole meltpool. Keyhole mode melting will cause gas bubbles to become trapped inside the solid material as the deep keyhole meltpool collapses on itself, leading to porosity in the finished part. Too low laser power or too fast scanning on the other hand will not enable the meltpool to become deep enough to melt the entire powder layer and the underlying solid metal,

leading to delaminated layers and porosity. [43] Increasing both the laser power and scanning speed is not a solution either, as it will cause instability in the meltpool. This instability leads to the formation of isolated molten droplets instead of a continuous meltpool, called balling. Balling causes porosity and increased surface roughness in the finished part. [142]

Early L-PBF machines used CO_2 lasers, which were common in high-power laser applications at the time. However, the CO_2 laser has some practical issues, mainly its long ~10 μm infrared wavelength which is poorly absorbed by metal powders and cannot be delivered via optical fibre. Over time, L-PBF manufacturers have moved to fibre lasers (today mainly ytterbium-doped fibre lasers), that have high efficiency, beam quality, and reliability – and importantly, can be delivered via optical fibre. All these laser types are capable of multi-kilowatt powers, but typically metal L-PBF lasers are in the 200-1000W range. [143, 144] Some L-PBF machines are also being offered in a multi-laser configuration with up to 4 simultaneously operating beams, in an effort to decrease build times.

There are two main modes of melting. The first is called conduction mode and it is a typical mode for L-PBF processes. In conduction mode, a U-shaped meltpool is formed, which does not penetrate deep into the into the material. There is a risk of underpenetration and unmelted powder, especially if the powder layer is very thick. [145, 136] The other typical mode is keyhole mode, which occurs when using a laser beam with a very high energy density, leading to partial vaporisation of the metal and deep penetration of the laser beam into the solid material. Due to the deep penetration, there are fewer opportunities for the laser beam to reflect out of the meltpool, leading to higher energy absorption by the material, which further exacerbates the overpenetration and vaporisation. As the beam moves forward, the hole collapses on itself, trapping pockets of gas inside the now solidified metal. This phenomenon causes porosity in the finished part, which degrades the mechanical properties of the finished part as large voids often act as crack propagators. The keyhole mode can therefore be considered a defect mechanism in L-PBF. [145]

A third possible melting mode is the transition mode, which occurs with laser beam energy densities between conduction and keyhole mode and has properties of both [145, 146]. The transition mode was described in laser welding already in 1996 by Zhang et al. [147], then called “unstable mode welding”. An important metric for distinguishing between these modes is laser beam absorptivity. An increasing absorptivity means that less radiation is escaping the meltpool via reflections, which is a direct indicator of a deepening meltpool and thus the onset

of keyhole mode. If the absorptivity of a material is for example ~30% in conduction mode, the melting can be said to be in transition mode at ~55% absorptivity, while keyhole mode typically results in ~80% absorptivity. Using transition mode melting in L-PBF instead of conduction mode in effort to increase the size and depth of the meltpool and reduce risk of underpenetration or unmelted particles could be of interest. Patel & Vlasea (2020) [145] developed process diagrams and an analytical model capable of forecasting thresholds of melting mode transition in L-PBF, but research is needed on reliably maintaining this relatively unstable melting mode in L-PBF. [145, 146]

Appendix 3: Surface roughness as a powder bed parameter

SR was investigated as a possible powder bed parameter for validating the simulation. *SR* was not chosen for the purposes of this thesis, but an overview is provided in case it is explored in the future as a validated parameter, to replace or augment validation by *PD*.

Surface roughness of the powder bed can be generally described as a measure of the unevenness or variations in height of the powder bed surface [93]. High surface roughness can lead to poor surface quality in the finished part, dimensionally inaccurate parts, or even increase the risk of the recoater colliding with solidified metal [22, 33].

Characterisation

As with *PD*, a standard characterisation method does not exist. Multiple authors have presented their own methods for characterising *SR* with practical experiments, which are presented in Table 14.

Table 14 Results of literature review on powder bed surface roughness characterisation methods. *SR* = surface roughness, *PD* = packing density, *h* = layer height

Author, year	Property	Method	AM	Remarks	Ref.
Sillani et al. 2021	*SR, PD*	Profilometer	Polymer L-PBF	Pre-made cup recoated and analysed with profilometer to study relation of PD and Ra	[48]
Le et al. 2021	*h, SR*	Imaging	L-PBF	Scanner (contact image sensor). Versatile, possibly for in-situ as well	[148]
Vakifahmetoglu et al. 2021	*SR*	Imaging	L-PBF	Image processing of high contrast photographs	[19]
Mussatto et al. 2021	*SR*	3D microscopy	L-PBF	Point measurements, transported bed to microscope	[42]
Yuasa et al. 2021	*SR*	Imaging	-	Projected stripe pattern on bed, read deviations in stripes.	[149]
Salehi et al. 2022	*SR*	Imaging	-	Measuring greyscale of each pixel + pixel-counting to find amplitude and wavelength of roughness	[150]

As Table 14 shows, a wide variety of optical systems have been used to characterise surface roughness of powder beds, ranging from specialised profilometers to 3D microscopy and repurposed paper scanners. Different characterisation methods produce different surface roughness metrics, which makes it quite difficult to compare the results of these studies. Typical examples of used metrics could be a root mean square of profilometer height readings [48] or

the wavelength and intensity of light reflected off the powder bed with an ad-hoc imaging-based measurement [150].

Yuasa et al. (2021) [149] measured powder bed surface morphology by projecting a striped pattern on the powder bed, photographing it, and using image processing to convert the image of the powder bed with projected pattern into point group data from which a standard deviation of powder bed height can be extracted. Le et al. (2021) [148] produced a height map of their powder bed by photographing it and used the "blurriness" of out-of-focus particles as a metric to calculate their distance from the camera. Vakifahmetoglu et al. (2021) [19] used a wireless digital camera mounted on the ceiling of the build chamber to capture images of the recoated powder bed. These images were filtered and processed to produce an image of the powder bed where defects are pronounced as black shapes on a white background. Sillani et al. (2022) utilised a commercial laser profilometer mounted on the recoater to generate near real time data on powder bed surface heigh variations. Mussatto et al. (2021) used a 3D digital optical microscope with 300x magnification to measure the maximum profile height in the powder bed, as in the difference in elevation between lowest and highest point in the bed.

Interestingly, some of the ad-hoc systems provide more versatile and equally reliable data compared to commercial roughness measuring profilometers. For example the scanner method presented by Le et al. (2021) not only characterises the surface roughness, but can also be used to estimate packing density by detecting voids in the powder bed. However it should be noted that all of these systems require varying amounts of set-up, calibration and/or programming to produce reliable results, and so far the only other option is to procure special equipment such as profilometers and 3D microscopes.

Appendix 4: Results of literature review on DEM parameters

Table 15 Results of literature review; DEM parameters for IN718 and HX alloy powder. μ = friction coefficient, S = static friction, D = dynamic friction, pp = particle-particle, pw = particle-wall

Author, year, material if not IN718	*d50*	Density [kg/m^3]	*μSpp*	*μDpp*	*μSpw*	*μDpw*	Restitution coefficient	Surface energy [mJ/m^2]	Poisson's ratio	Young's modulus [GPa]
Lee et al. 2018	68	8150	0.2	0.577	0.2	0.176	0.75		0.3	193
Lee et al. 2016	20		0.3	0.3						
Marchais et al. 2021	31	8000	0.3				0.1	0-1		
Ganesan et al. 2022	40	8200	0.005	0.3	0.005	0.9	0.35		0.3	1
Lee et al. 2016	25		0.3							
Gao et al. 2020	33								0.3	
Thirugnanasambantham et al. 2015									0.28	
Lampitella et al. 2021	25	9187	0.15	0.7			0.7		0.3	0.2
Wang et al. 2020 HX	34	8200	0.005	0.3			0.35		0.3	1
Wang et al. 2021 (Values as above)										
Lin et al. 2022 (Values from Wang et al. 2020)										
Nguyen et al. 2017	31		0.42		0.26					
Han et al. 2019 HX	35	8220	0.005	0.4			0.4	1.6		
Dai et al. 2019	30	8192					0.3		0.3	205
Dai et al. 2021	30	8192	0.51	0.39	0.05	0.05	0.3	0.1-0.5	0.3	205

Table 16 Results of literature review on DEM parameters for AM powder. Values were either used by the corresponding authors in DEM simulation or icharacterised by them for other purposes. μ = friction coefficient S = static friction, D = dynamic friction, pp = particle-particle, pw = particle-wall

Author, year, material	*d50*	Density [kg/m^3]	*μSpp*	*μDpp*	*μSpw*	*μDpw*	Contact stiffness [kN/m]	Restitution coefficient	Surface energy [mJ/m^2]	Poisson's ratio	Young's modulus [GPa]
Lee et al. 2018 316L	20	7990	0.2	0.577	0.2	0.176		0.75		0.3	193
Meier et al. 2019	35								0.1		
Shaheen et al. 2021	37								0-0.4		
Yim et al. 2022 GA Ti48Al2Cr2Nb	72		0.23	0.54	0.58			0.287			
Yim et al. 2022 PREP Ti48Al2Cr2Nb	85		0.12	0.31	0.332			0.2			
Li et al. 1999 316L								0.6-0.8			
Yao et al. 2021 316L		7800	0.085	0.6				0.64	1		
Xiang et al. 2021 316L	20	7800	0.1	0.62				0.9	0.1	0.3	2.1
Wu et al. 2022 Al	40		0.01	1.268				0.7	0.2	0.31	
Tian et al. 2020 316L		7990	0.62					0.9	0.097		
Meier et al. 2019 Ti6Al4V	34	4430	0.4				0.2-0.05	0.4	0.1		
Fouda-bayly et al. 2019 Ti6Al4V	50	4300	0.01	0.5	0.1	0.5		0.5		0.3	
He et al. 2020 Ti6Al4V	50	4430	0.01	0.3				0.4		0.3	110
Steuben et al. 2016 316L		8000	0.25				0.0012				
Desai et al. 2019 Ti6Al4V			0.185		0.12						
Phua et al. 2021 Ti6Al4V			0.12		0.05		5		0.5		
Chen et al. 2019 316L		7800	0.62					0.9	0.097		

Appendix 5: Test results of rejected validation sample types

The initially planned validation experiment samples consisted of 10 mm tall, 90 mm diameter "open cup" type samples built on a smaller EOS M 100 system, as well as 50-100 mm tall, 24 mm diameter "closed container" type of samples built on the EOS M 290 system. In this approach, the packing density determined from the open cup would be the baseline powder bed packing density for validating the simulation, and the packing density measurements of taller samples would be used for estimating the effect of powder bed depth on powder bed density. This information would be used for estimating the error resulting from the fact that the simulated powder bed will be an order of magnitude shallower than in the practical experiment, due to computational limitations.

In order to determine packing density, the mass of powder contained in the open cup sample would be measured by weighing the sample before and after emptying the powder, and its volume measured by filling it with water and weighing it again. The same procedure would be done for the closed containers. The closed containers would be sealed by a thin cap, which could be punched open. The closed container sample designs were inspired by the works of Jacob et al. (2016) [53] and Elliott et al. (2016) [57] as well as previous experiences of colleagues at EOS Finland.

Preliminary experiments were done to judge the feasibility of measuring internal volumes and powder masses from the samples. First, mock-ups of all sample types were made from PLA polymer with a Prusa Mini (Prusa Research, Czechia) fused filament fabrication (FFF) desktop system. The mock-ups were repeatedly filled with water and weighed, to estimate the reliability of measuring their volume using water. Pouring tests were also done to estimate how large the opening in closed container type samples should be to allow water and IN718 powder to be poured out easily and reliably. It was found that a 5 mm aperture is the minimum, and the "neck" of the samples should be reduced or removed. It was also deemed impossible to reliably measure the volume of any sample using water, partly due to surface tension and partly due to simple difficulty in judging filling level. Therefore nominal, calculated volume of the 3D CAD model would be used.

After the design was refined using the polymer mock-ups, 36 closed container samples in two jobs (referred to as preliminary test 1 & 2) were built with an M 290 using IN718. The built samples are seen in Figure 61 (test 1), Figure 63 (test 2) and Figure 62 (test 2 sample cross

sections), and the types and quantities of test samples built are specified in Table 17 below. One 90 mm open cup sample (OS1) was also built using the M 100.

The caps on the first 12 samples in test 1 did not fuse properly, due to low energy density on the cap downskin (ds).

Test 2 featured samples with cone- or dome-shaped internal ceilings on the lids (that should be easier to build) on punch lids and hexagonal twist-off caps, as well as higher laser power on the downskins. All samples with higher downskin laser power or conical punch/twist-off caps were built successfully and were easy to open. Necked punch samples with straight ceilings failed on default downskin power.

Some samples were not weighed due to time constraints, as the closed sample method was quickly deemed impractical.

Table 17 Preliminary IN718 test samples

Sample type and job	Identifier	Height [mm]	Quantity
Preliminary test 1			
Default necked punch sample and parameters	1-4 R1 5	50	4
Default necked punch sample and parameters	1-4 R1 7	70	4
Default necked punch sample and parameters	1-4 R1 10	100	4
Preliminary test 2			
Default necked punch sample and parameters	1 T1 25	25	1
Default necked punch, 180 W downskin on cap	2-4 T1 25	25	3
20˚ cone punch, default parameters, no neck	1-2 25 D c20	25	2
20˚ cone punch, 180W downskin on cap, no neck	3-4 25 D c20	25	2
Twist-off cap with 20˚ internal cone, default parameters, no neck	1-2 25 TO3 c20	25	2
Twist-off cap with 20˚ internal cone, 180W downskin	3-4 25 TO3 c20	25	2
Twist-off cap with 30˚ internal cone, default parameters	1-4 25 TO3 c30	25	4
Twist-off cap with 45˚ internal cone, default parameters	1-4 25 TO3 c45	25	4
Twist-off cap with hemisphere internal dome, default parameters	1-4 T1 25 TO3	25	4
Preliminary M 100 open cup test			
90 mm diameter circular open cup	OS1	10	1

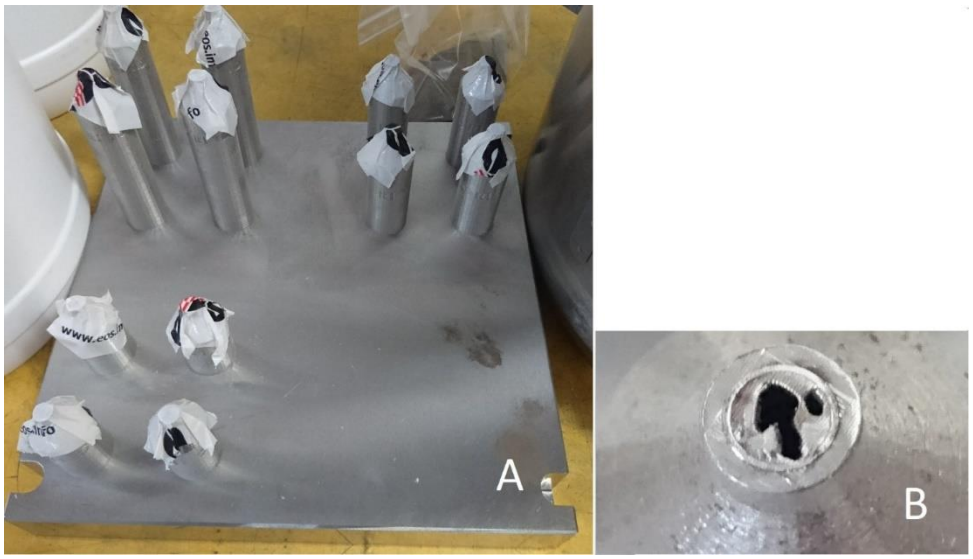

Figure 61 A) IN718 preliminary test 1, using default necked punch samples, default IN718 parameters. Caps covered with tape due to unfused caps exposing the powder inside. B) Close-up of unfused cap.

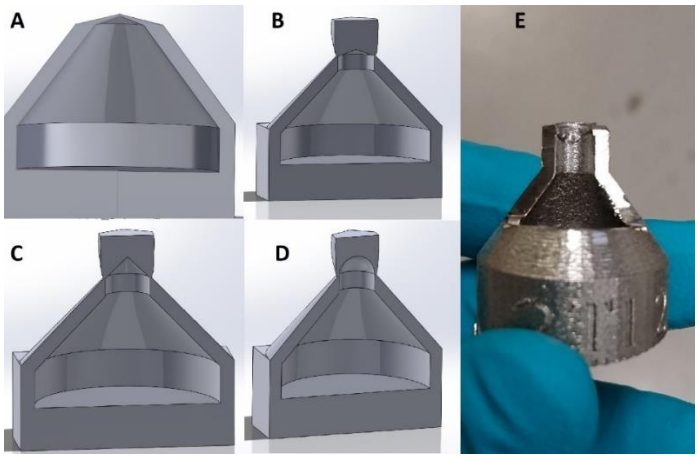

Figure 62 crossections of the CAD models for: A) 20˚ cone B) 20˚ cone twist-off C) 45˚ cone twist-off D) hemisphere twist-off E) crossection of a default necked sample - note the burr inside the neck, from puncing in the lid, and coarseness of downskin inside sample.

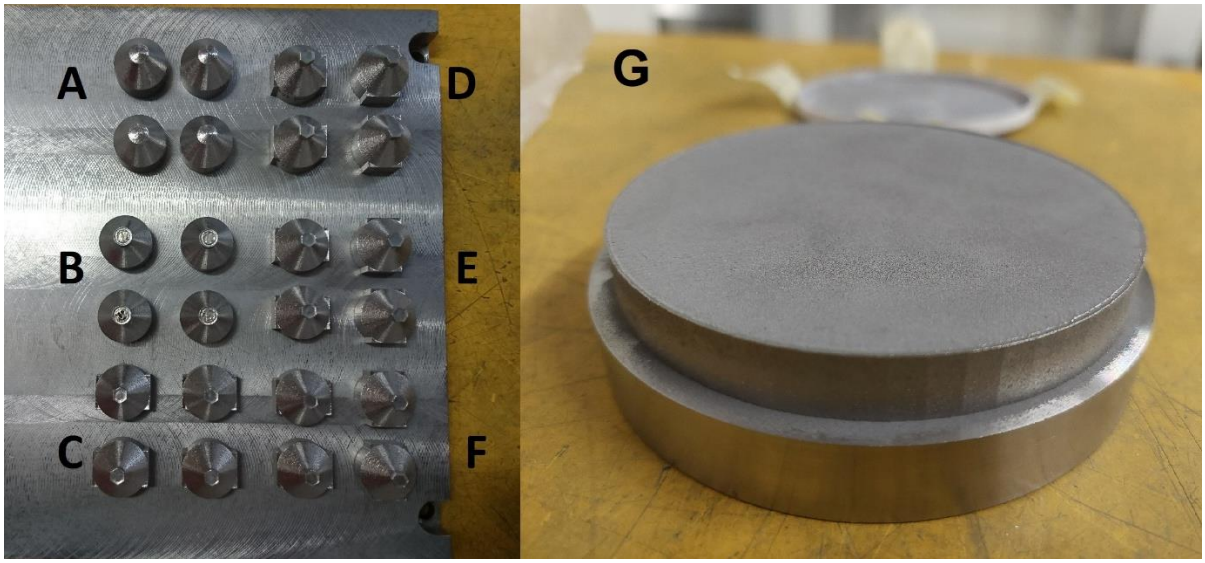

Figure 63 IN718 preliminary test 2, using 25mm samples and different parameters and opening mechanisms. A) 20˚ conical punch lid B) default necked punch sample C) Twist-off cap with hemisphere internal dome D) Twist-off cap with 20˚ internal cone E) Twist-off cap with 30˚ internal cone F) Twist-off cap with 45˚ internal cone G) M 100 Small open cup sample.

Packing density tests were conducted for those Test 2 samples which were built successfully. *PD* was calculated using the nominal volume of the 3D CAD model, as using water to measure true volume was deemed highly unreliable. Measurements and packing densities are presented in Table 8. There is significant variance in sample mass, which is best explained by the fact the samples were removed from the building platform with a bandsaw, and were not necessarily cut perfectly straight, and had significant burrs. The sample volume for the small open cup sample is a measured volume, not nominal unlike other samples.

Table 18 Preliminary test 2 & M 100 open cup packing density measurements

Sample height	class	spec	n.	Parameters	Comment	*m powder*	*V powder*	*V nominal*	*PD*
25	twistoff3	hemisphere	1	Default					
25	twistoff3	hemisphere	2	Default					
25	twistoff3	hemisphere	3	Default					
25	twistoff3	hemisphere	4	Default					
25	twistoff3	cone 20 ˚	1	Default		11.7	1.43	3.002	47.5 %
25	twistoff3	cone 20 ˚	2	Default		11.7	1.43	3.002	47.5 %
25	twistoff3	cone 20 ˚	3	Default	Spilled				
25	twistoff3	cone 20 ˚	4	Default	Spilled				
25	twistoff3	cone 30 ˚	1	Default		11.7	1.43	3.005	47.5 %
25	twistoff3	cone 30 ˚	2	Default		11.8	1.44	3.005	47.9 %
25	twistoff3	cone 30 ˚	3	Default		11.8	1.44	3.005	47.9 %
25	twistoff3	cone 30 ˚	4	Default		11.7	1.43	3.005	47.5 %
25	twistoff3	cone 45 ˚	1	Default		11.9	1.45	3.013	48.2 %
25	twistoff3	cone 45 ˚	2	Default		11.7	1.43	3.013	47.4 %
25	twistoff3	cone 45 ˚	3	Default		12	1.46	3.013	48.6 %
25	twistoff3	cone 45 ˚	4	Default		11.9	1.45	3.013	48.2 %
25	punch	neck	1	Default	Lid not fused				
25	punch	neck	2	180W ds	Spilled				
25	punch	neck	3	180W ds		13	1.59	3.5	45.3 %
25	punch	neck	4	180W ds		12.9	1.57	3.5	44.9 %
25	punch	cone 20 ˚	1	180W ds		13.1	1.6	3.44	46.4 %
25	punch	cone 20 ˚	2	180W ds		13.1	1.6	3.44	46.4 %
25	punch	cone 20 ˚	3	Default		12.9	1.57	3.44	45.7 %
25	punch	cone 20 ˚	4	Default		12.9	1.57	3.44	45.7 %
10	Open cup	Small	1	Estimated	Built well	265.1	32.3	62.4	51.8 %

Conclusions

- The closed container samples were dropped from the final validation plan.
    - Time-consuming to manufacture and challenging to measure.
    - Rough interior, difficult to empty the samples of powder/measure volume.
    - High deviation in *PD* results. *PD* also suspiciously low, near apparent density.
- The twist-off cap models were deemed the best closed sample type.
    - Easier and more repeatable opening.
    - Powder is not compacted during opening, making it easier to empty.
    - No risk of punched lid fragments being included in sampled powder.
    - Lower deviation in *PD* results.
    - The lowest ceiling cone (in this case a 20˚ cone) is recommended due to lower amount of "extra" powder being included in measurements.
        - However, the lower ceiling increases the brittleness of opening, which makes it easy to accidentally spill the sample as it suddenly cracks open.
- Preliminary open cup samples built with the M 100 were very promising
    - *PD* = 51.8 % is in line with final validation results (though not repeated)
    - Built well even though the M 100 does not have an IN718 process and estimated parameters were used.
- Since the M 290 sample is larger (= lower impact of small spillage and user error) and a better analogue of the simulation model, it was chosen for validation. However there are drawbacks:
    - Removing and transporting the 10-15 kg M 290 building platforms without disturbing the powder sample is more difficult than with the M 100
    - Less accurate industrial scales must be used instead of precision scales

Appendix 6: Example calculation of sample volume

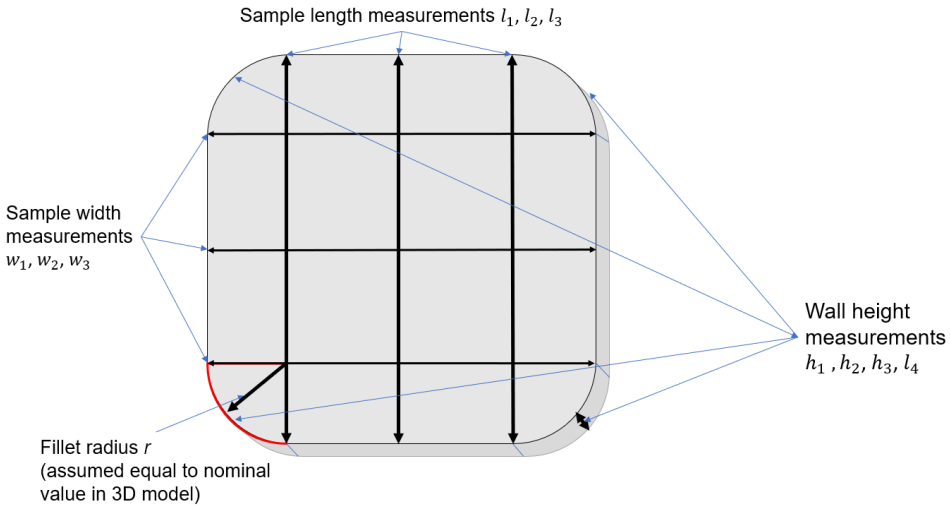

The mean value of all measurements per dimension (width, length, height) are calculated as shown in Equations 4, 5, and 6, using values given in Table 19.

$$l = \frac{\sum l_n}{3} = \frac{172.98 + 172.98 + 172.99}{3} = 172.98\ mm \tag{4}$$

$$\mathrm{w} = \frac{\sum w_n}{3} = \frac{172.95 + 172.98 + 172.98}{3} = 172.97\ mm \tag{5}$$

$$\mathrm{h} = \frac{\sum h_n}{4} = \frac{5.10 + 5.01 + 5.06 + 5.08}{4} = 5.06\ mm \tag{6}$$

Table 19 Example values for sample volume calculation

Dimension	1	2	3	4	Mean	Unit
Length	172.98	172.98	172.99		172.98	mm
Width	172.95	172.98	172.98		172.97	mm
Height	5.10	5.01	5.06	5.08	5.06	mm
radius					10	mm

The mean values are used to calculate the volume as shown in Equation 10.

$$V_{sample\_measured}\ [cm^3] = \frac{(w - 2r) * l * h + \pi * r^2 * h + (l - 2r) * 2r * h}{1000} \tag{10}$$

$$= \frac{(172.97 - 2 * 10) * 172.98 * 5.06 + (\pi * 10^2 * 5.06) + (172.98 - 2 * 10) * 2 * 10 * h}{1000}$$

$$= 150.9\ \mathrm{cm}^3$$

Appendix 7: Example calculation of powder mass, volume, and *PD*

When the sampled volume is known, the powder volume can be calculated.

$$m_{powder\_measured} = m_{full} - m_{emptied} \quad (11)$$
$$= 11083 - 10423$$
$$= 660g$$

Powder volume can be found through powder mass and density.

$$V_{powder} = \frac{m_{powder}}{\rho_s} \quad (12)$$
$$= \frac{660}{8.2}$$
$$= 80\ cm^3$$

PD can be calculated as shown in Equation 1

$$PD = \frac{V_{powder}}{V_{sample}} \quad (1)$$

$$PD = \frac{80}{150.9}$$

$$= 53\%$$

Appendix 8: Results and measurements of OL-samples

All calculated values that were used for determining min, max, and measured packing densities are presented in Table 20. Calculated values are highlighted with grey, measured values with white. Full height measurements of each OL-sample are presented in Table 21

Table 20 OL-validation experiment data

	OL1	OL2	OL3	OL4	OL5	Average	unit
Height	5,18	5,02	5,07	5,02	5,09	5,07	mm
Internal width	172,95	172,98	172,98	172,98	172,98	172,97	mm
Internal length	172,98	172,98	172,99	172,97	172,97	172,98	mm
m_full	18554	11151	11309,4	14076,7	15136,7	14045,56	g
m_empty	17893,4	10509,7	10660,8	13430,6	14481,6	13395,22	g
m_cleaned	17893	10509,5	10660,2	13429,6	14481,2	13394,70	g
m_min_powder (bag)	657,1	637,7	648,2	645,6	653,7	648,46	g
m_measured_powder	660,6	641,3	648,6	646,1	655,1	650,34	g
m_max_powder	661,0	641,5	649,2	647,1	655,5	650,86	g
V_min_powder	80,13	77,77	79,05	78,73	79,72	79,08	cm^3
V_measured_powder	80,56	78,21	79,10	78,79	79,89	79,31	cm^3
V_max_powder	80,61	78,23	79,17	78,91	79,94	79,37	cm^3
V_sample_measured	154,38	149,78	151,35	149,69	151,78	151,40	cm^3
V_sample_nominal	149,22	149,22	149,22	149,22	149,22	149,22	cm^3
Packing density (min)	51,9%	51,9%	52,2%	52,6%	52,5%	52,2%	%
Packing density (measured V)	52,2%	52,2%	52,3%	52,6%	52,6%	52,4%	%
Packing density (max)	52,2%	52,2%	52,3%	52,7%	52,7%	52,4%	%
Packing density (measured m, nominal V)	54,0%	52,4%	53,0%	52,8%	53,5%	53,2%	%

Table 21 Height measurements of OL-samples

Location	OL1	OL2	OL3	OL4	OL5	Unit
Front-left	5,06	5,02	5,01	5,01	5,04	mm
Front-right	5,04	5,02	5,05	5	5,09	mm
Rear-left	5,31	5,02	5,13	5,05	5,1	mm
Rear-right	5,29	5,02	5,1	5,01	5,12	mm
Mean	5,18	5,02	5,07	5,02	5,09	mm

Appendix 9: Repeated simulation run

The validated simulation was run again to ensure its repeatability and consistency. It was found that the simulations featured no discernible difference in packing structure, but the uniformity of the powder bed may vary slightly; in the repeated run, the stable region was slightly longer than in the initial run, which introduced 1-2 percentage points of variance in method 2 and 4 measurements (i.e. min and measured simulated *PD*). Comparison between full powder beds is provided in Figure 64. Another relevant observation is that runtime was roughly half of that of the initial run.

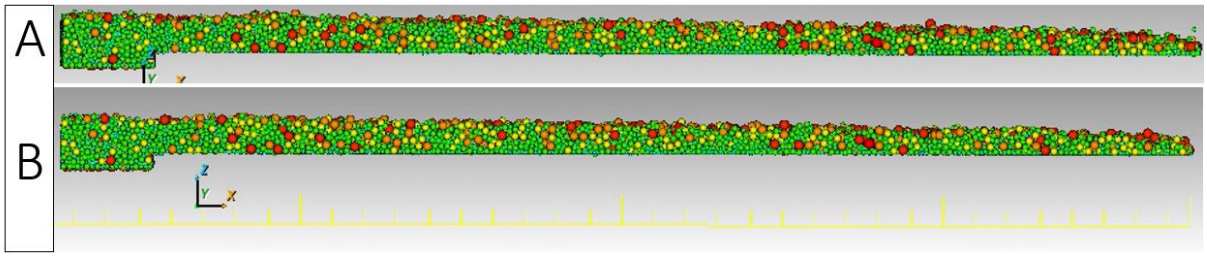

Figure 64 Comparison between initial and repeat simulation runs. A) initial B) repeat.